University of Alberta

Bimetallic catalysts for low-pressure ring opening

by

Jing Shen

A thesis submitted to the Faculty of Graduate Studies and Research
in partial fulfillment of the requirements for the degree of

Master of Science
in
Chemical Engineering

Department of Chemical and Material Engineering

©Jing Shen

Spring 2011
Edmonton, Alberta

Permission is hereby granted to the University of Alberta Libraries to reproduce single copies of this thesis and to lend or sell such copies for private, scholarly or scientific research purposes only. Where the thesis is converted to, or otherwise made available in digital form, the University of Alberta will advise potential users of the thesis of these terms.

The author reserves all other publication and other rights in association with the copyright in the thesis and, except as herein before provided, neither the thesis nor any substantial portion thereof may be printed or otherwise reproduced in any material form whatsoever without the author's prior written permission.

Abstract

Selective ring opening of naphthenic molecules is a preferred reaction to increase cetane number of fuels, and it should result in products with no loss in molecular weight and longer alkyl side chains. Benzocyclopentane (indan) ring opening was studied under hydrogen atmospheric pressure at 609 K with a variety of poly-(vinylpyrrolidone)-stabilized Pd, Ir, and Ru mono- and bimetallic nanocatalysts. The bimetallic catalysts were synthesized either via simultaneous reduction or via hydrogen-sacrificial technology, providing presumably alloy or core-shell structures, respectively. Pd catalysts displayed the lowest activity; Ru showed the highest formation of *o*-xylene. Monometallic Ir (sphere 1.6 nm) and bimetallic Pd-Ir catalyst (2.7 nm) with presumable core-shell structure showed superior activity and selectivity to desired *2*-ethyltoluene and *n*-propylbenzene, as well as lower cracking as compared to industrial Pt-Ir catalyst.

Acknowledgement

I would like to thank my supervisor Assistant Professor Natalia Semagina. I very much appreciate the support and guidance she has given me throughout my Master program.

Special thanks to:

- Dr. Xing Yin and Dr Kavithaa Loganathan for their advice and supervising on laboratory work. They were ready to give me a helping hand whenever I was faced a problem.
- Shiraz Merali for AAS training.

Financial support from the Imperial Oil-Alberta Ingenuity Centre of Oil Sands Innovation (COSI) at the University of Alberta is gratefully acknowledged.

Table of contents

1. Introduction…….... 1

2. Literature review…….……..... 4

2.1. Methods of nanoparticle stabilization..... 4

2.1.1. General methods of nanoparticle stabilization……..... 4

2.1.1.1. Electrostatic stabilization…… 4

2.1.1.2. Steric stabilization……... 5

2.1.1.3. Electrosteric stabilization…… 6

2.1.1.4. Ligand stabilization……. 7

2.1.1.5. Solvent stabilization……. 8

2.1.2. Size control in stabilization of metal nanoparticles with PVP……. 8

2.1.2.1. Effect of PVP concentration…… 9

2.1.2.2. Effect of average molecular weight of PVP……. 9

2.1.2.3. Effect of nature and concentration of alcohol …… 10

2.1.2.4. Other examples of metal nanoparticle stabilization with PVP…….. 10

2.1.3. Crystal growth and shape control of PVP-stabilized nanoparticles .....……..... 11

2.1.3.1. Nanospheres…….. 11

2.1.3.2. Nanocubes……. 14

2.1.3.3. Nanotetrahedrons……. 17

2.1.3.4. Nanobars and nanorods…… 18

2.1.4. Bimetallic catalysts.....……..... 20

2.1.4.1. Synergism…….. 20

2.1.4.2. Preparation……... 21

2.2. Catalytic ring opening reaction……..... 26

2.2.1. Introduction of oil refinery challenges: sulfur and aromatics contents……..... 26

2.2.2. Selective ring opening mechanisms…… 27
2.2.3. Ring opening catalysis…… 28
2.2.3.1. Acid catalysts…… 28
2.2.3.2. Bifunctional catalysts…… 30
2.2.4. Selective ring opening over supported noble metal catalysts…….. 32
2.2.4.1. Mechanism…… 32
2.2.4.2. Effect on type of metals (mono- and bi- metallic)……. 34
2.2.4.3. Effect on nanoparticle sizes…….. 36
2.2.4.4. Effect on acid-base supports……. 37
2.2.4.5. Selective ring opening of methylcyclopentane (MCP)…. 37
2.2.4.6. Ring opening of indan……... 38
2.3. Concluding remarks from the literature review…….. 40
3. Materials and Methods……..……..... 41
3.1. Materials…….…….…… 41
3.2. Preparation of catalysts…….……..... 41
3.2.1. Synthesis of PVP-stabilized Pd nanoparticles and Pd/γ-Al_2O_3 catalysts…….……..... 42
3.2.1.1. One-step synthesis method…… 42
3.2.1.2. Stepwise growth synthesis method…… 43
3.2.1.3. Nanoparticle deposition…… 44
3.2.2. Synthesis of PVP-stabilized Ru nanoparticles and Ru/γ-Al_2O_3 catalysts…….…… 44
3.2.2.1. $Ru(NO)(NO_3)_3$ precursor…….. 45
3.2.2.2. $RuCl_3$ precursor…… 47
3.2.2.3. Nanoparticle deposition…… 47
3.2.3. Synthesis of PVP-stabilized Ir nanoparticles and Ir/γ-Al_2O_3 catalysts……..…….……..... 48
3.2.3.1. Stepwise growth synthesis method…… 48
3.2.3.2. Nanoparticle deposition…… 49

3.2.4. Synthesis of PVP-stabilized core-shell structure bimetallic nanoparticles and corresponding supported catalysts…….. 49

3.2.4.1. Metal core preparation……. 50

3.2.4.2. Core-Shell structure preparation…….. 51

3.2.4.3. Nanoparticle deposition…… 51

3.2.5. Synthesis of PVP-stabilized alloy structure bimetallic nanoparticles and corresponding supported catalysts…….. 52

3.2.5.1. Pd-Ir colloids…… 52

3.2.5.2. Ir-Ru colloids…… 53

3.2.5.3. Pd-Ru colloids…….. 53

3.2.5.4. Nanoparticle deposition…… 54

3.3. Colloids and catalyst characterization techniques…….. 54

3.3.1. Transmission electron microscopy (TEM) …… 54

3.3.2. UV-visible spectroscopy……..... 55

3.3.3. Atomic absorption spectroscopy (AAS)…….. 55

3.3.4. Neutron activation analysis (NAA)……. 56

3.3.5. X-ray photoelectron spectroscopy (XPS) ……... 56

3.4. Low-pressure ring opening of indan…….. 56

3.4.1. Catalysts pre-treatment……..... 57

3.4.2. Experimental set up and conditions……... 57

3.4.3. Reaction product identification……..... 59

3.4.4. Calculation of indan conversion, catalytic activity, and selectivity……..... 61

4. Results and discussions……. 63

4.1. Catalyst synthesis and characterization ……... 63

4.1.1. Monometallic Pd/γ-Al_2O_3 catalysts……. 63

4.1.1.1. Pd nanoparticles via one-step growth…….. 63

4.1.1.2. Pd nanoparticles via stepwise growth…….. 66

4.1.1.3. Pd/γ-Al_2O_3 catalysts……. 69

4.1.2. Monometallic Ru/γ-Al_2O_3 catalysts……. 70

4.1.2.1. Ru nanoparticles via one-step growth…….. 70
4.1.2.2. Ru nanoparticles via stepwise growth…….. 73
4.1.2.3. Ru/γ-Al_2O_3 catalysts……. 74
4.1.3. Monometallic Ir/γ-Al_2O_3 catalysts……... 76
4.1.3.1. Ir nanoparticles via stepwise growth…… 76
4.1.3.2. Ir/γ-Al_2O_3 catalysts…….. 80
4.1.4. Bimetallic catalysts……..... 81
4.1.4.1. Alloy structures……. 81
4.1.4.2. Core-shell structures…….…….. 88
4.1.4.3. M1-M2/γ-Al_2O_3 catalysts…… 90
4.1.5. PVP removal……..... 91
4.2. Low-pressure ring opening of indan…….. 91
4.2.1. Mass transfer limitations…….. 91
4.2.1.1. External mass transfer limitation…….. 92
4.2.1.2. Internal mass transfer limitation…….. 92
4.2.4. Catalytic reaction results…….. 96
4.2.4.1. Ring opening of indan over industrial Pt-Ir catalyst 96
4.2.4.2. Ring opening of indan over monometallic catalysts 98
4.2.4.3. Ring opening of indan over Pd-Ir/γ-Al_2O_3 bimetallic catalysts…….. 104
4.2.4.4. Ring opening of indan over Ir-Ru/γ-Al_2O_3 bimetallic catalysts…….. 109
4.2.4.5. Ring opening of indan over Pd-Ru/γ-Al_2O_3 bimetallic catalysts…….. 112
5. Conclusions……. 116
6. References……... 117
Appendix A: TEM images and corresponding histograms for repeated nanoparticles…….. 122
Appendix B: Summary of low-pressure ring opening of indan…… 126
Appendix C: GC-MS analysis…….. 129

List of Tables

Table 2.1	Past diesel fuel specifications in the European Union.	27
Table 3.1	Synthesis conditions for Pd nanoparticles using one-step synthesis method.	43
Table 3.2	Synthesis conditions for Pd nanoparticles using stepwise growth method.	43
Table 3.3	Synthesis conditions for Ru nanoparticles.	46
Table 3.4	Synthesis conditions for Ir nanoparticles.	49
Table 3.5	Synthesis conditions for Pd-Ir nanoparticles (Pd/Ir molar ratio = 3/1).	54
Table 3.6	Experimental conditions and GC analytical procedure for catalytic low-pressure ring opening of indan.	59
Table 4.1	Pd loading on γ-Al_2O_3 determined by AAS.	69
Table 4.2	Ru loading on γ-Al_2O_3 determined by AAS.	75
Table 4.3	Ir loading on γ-Al_2O_3 determined by NAA.	81
Table 4.4	Bimetallic catalysts loading on γ-Al_2O_3 determined by NAA and corresponding M1 to M2 metal ratios.	90
Table 4.5	XPS composition results (in mass concentration).	91
Table 4.6	Parameters for effective diffusivity.	94
Table 4.7	Reaction conditions and experimental data of indan ring opening over 1.9 nm Ir3Ru1_1/γ-Al_2O_3 catalyst.	95
Table 4.8	Weisz-Prater criterion calculation.	95
Table 4.9	Comparison of selectivities to single cleavage, *n*-propylbenzene, *o*-xylene, and lights for indan ring opening over nanosized monometallic catalysts. Metal loading was 1.2 mg for Pd1, Ru1, Ir worm, and industrial Pt-Ir catalysts; and 0.6 mg for Ir sphere catalyst. Data in brackets are one standard deviation.	102

Table 4.10 Comparison of selectivities to single cleavage, *n*-propylbenzene, and lights for indan ring opening over nanosized Pd-Ir bimetallic catalysts. Metal loading was 1.2 mg for Pd1, Pd1Ir1, Pd1Ir3, Pd(c)Ir(s), and industrial Pt-Ir catalysts; and 0.6 mg for Ir sphere catalyst. Data in brackets are one standard deviation. 108

Table 4.11 Comparison of selectivities to single cleavage, *n*-propylbenzene, and lights for indan ring opening over nanosized Ir-Ru bimetallic nanocatalysts. Metal loading was 1.2 mg for Ru1, Ir3Ru1, Ir1Ru1, Ir1Ru3, and industrial Pt-Ir catalysts; and 0.6 mg for IrS21 sphere catalyst. Data in brackets are one standard deviation. 112

Table 4.12 Comparison of selectivities to single cleavage, *n*-propylbenzene, and lights for indan ring opening over nanosized Ir-Ru bimetallic nanocatalysts. Metal loading was 1.2 mg for Pd1, Ru1, Pd1Ru3, and industrial Pt-Ir catalysts. Data in brackets are one standard deviation. 115

Table B1 Summary of catalytic results for low-pressure ring opening of indan. Reaction temperature was 336 ^{o}C and reaction pressure was 1 atm pressure. 8 (or 6) data points were obtained at 150, 180, 210, (and 240 minutes) of time on stream with a duplicate experiment. Within the indicated times on stream the catalysts did not show noticeable deactivation. 126

Table C1 Reactant and major products confirmed by chemical standards and GC-MS. 129

Table C2 Possible by-products identified by GC-MS. 130

List of Figures

Figure 2.1	Two major polymer families, PVP and PPO, often used as nanoparticle stabilizers.	6
Figure 2.2	Electrosteric stabilization of metal nanoparticles by tetrabutylammonium halide.	7
Figure 2.3	(a) An f.c.c. cuboctahedron and (b) corresponding statistics of surface atoms.	13
Figure 2.4	Hydrogen-sacrificial technique to synthesize metal nanoparticles.	14
Figure 2.5	TEM images of PVP-stabilized Pd nanospheres synthesized by hydrogen-sacrificial technique: (a) 2nd reaction, 2.51 nm diameter, (b) 5th reaction, 3.84 nm diameter, and (c) 8th reaction, 6.15nm diameter.	14
Figure 2.6	(a) An f.c.c. cube and (b) corresponding statistics of surface atoms.	15
Figure 2.7	Mechanism of the formation of Pt nanocubes in presence of polymer.	16
Figure 2.8	Formation of silver nanocubes and nanotetrahedrons by polyol reduction method in the presence of PVP and a trace amount of sodium chloride.	16
Figure 2.9	(a) An f.c.c. tetrahedron, and (b) corresponding statistics of surface atoms.	17
Figure 2.10	High resolution image of a truncated tetrahedral (triangular) particle.	17
Figure 2.11	TEM image of PVP-stabilized Pt nanoparticles (55% regular tetrahedral, 22% distorted tetrahedral and 23% spherical nanoparticles).	18
Figure 2.12	Nucleation and growth: kinetic control. A, nanobars and B, nanorods.	19
Figure 2.13	TEM images of PVP-Pd: (a) nanobars, 9.1% EG in	19

solution and (b) nanorods, 72.2% EG in solution.
Figure 2.14 Various structures of bimetallic nanoparticles. 22
Figure 2.15 Simultaneous reduction of two metal ions in the presence of PVP leading to core-shell structures. 23
Figure 2.16 TEM image and histogram of PVP-stabilized Pd-Au bimetallic nanoparticles (molar ratio of Au/Pd = 3/1). 24
Figure 2.17 TEM images of PVP-stabilized Pd-core/Pt-shell bimetallic colloids synthesized by hydrogen-sacrificial technique: (c) molar ratio of Pd/Pt = 1/1 and (d) molar ratio of Pd/Pt =1/2. 25
Figure 2.18 TEM images of Pt(core)Ru(shell) nanoparticles obtained via successive reduction. 26
Figure 2.19 Mechanism for isomerization and ring opening of decalin over zeolites. 29
Figure 2.20 Mechanism for isomerization and ring opening of decalin over Pt-zeolites bifunctional catalysts. 31
Figure 2.21 Hydrogenolysis of methylcyclopentane via the multiplet mechanism. 33
Figure 2.22 Ring opening modes of 1,3-dimethylcyclohexane. 33
Figure 2.23 (a) Non-selective and (b) selective hydrogenolysis of methylcyclopentane from the viewpoint of octane number increase. 38
Figure 2.24 Ring opening of indan at α and β positions and further cracking products. 39
Figure 3.1 A schematic diagram of reactor setup. 58
Figure 3.2 A typical chromatogram of low-pressure ring opening of indan. Apart from indan and main products indicated on the chromatogram, other peaks ("lights" and "others") also were taken into consideration for analysis. 60
Figure 4.1 TEM photographs of Pd nanoparticles synthesized by one-step reaction (the scale bar is 20 nm) and 65

corresponding size distribution histograms: (a) Pd1: PVP/Pd = 10; [EtOH] = 40 %, (b) Pd2: PVP/Pd = 1; [EtOH] = 16 %, (c) Pd3: PVP/Pd = 40; [EtOH] = 70 %, and (d) Pd4: PVP/Pd = 10; [EtOH] = 70 %.

Figure 4.2 UV-vis spectroscopy of PVP-stabilized Pd nanoparticles and the precursor H_2PdCl_4. 66

Figure 4.3 TEM photographs of Pd nanoparticles synthesized by stepwise growth reaction (the scale bar is 20 nm) and corresponding size distribution histograms: (a) PdS1: PVP/Pd = 20, (b) PdS2: PVP/Pd = 10, (c) PdS3: PVP/Pd = 5, and (d) PdS4: PVP/Pd = 2.5. 68

Figure 4.4 (a) PdS1/γ-Al_2O_3, (b) PdS1/γ-Al_2O_3 after O_2-H_2 pretreatment (burning in air at 200 ^oC and reducing in H_2 at 375 ^oC, and (c) after reaction. 70

Figure 4.5 TEM photographs and the corresponding particle size distribution histograms of PVP-stabilized Ru nanoparticles synthesized by one-step reactions ($Ru(NO)(NO_3)_3$ precursor). (a), (b), (c) and (d) correspond to samples Ru1, Ru2, Ru3, and Ru4 respectively. The molar ratios of PVP/Ru were 10/1. 71

Figure 4.6 UV-vis spectroscopy of PVP-stabilized Ru nanoparticles and the precursor $Ru(NO)(NO_3)_3$. 72

Figure 4.7 TEM photographs of PVP-stabilized Ru nanoparticles synthesized by one-step reactions ($RuCl_3$ precursor). (a) Ru5: reduction temperature 200 ^oC and (b) Ru6: reduction temperature 160 ^oC. The molar ratios of PVP to $RuCl_3$ were 10/1. 73

Figure 4.8 (a) particle size distribution for RuS1 colloids (seed) and (b) TEM photographs of RuS2 colloids obtained via stepwise growth method ($Ru(NO)(NO_3)_3$ precursor). 73

Figure 4.9 TEM photographs of PVP-stabilized Ru nanoparticles synthesized by stepwise growth method ($Ru(NO)(NO_3)_3$ precursor). (a) seeds and (b) RuS3 (forth step growth). 74

Figure 4.10 (a) Ru1/γ-Al_2O_3 (b) Ru1/γ-Al_2O_3 after O_2-H_2 pretreatment (burning in air at 200 ^oC and reducing in H_2 at 375 ^oC), and (c) Ru1/γ-Al_2O_3 after reaction. 75

Figure 4.11 TEM photographs of Ir nanoparticles synthesized by stepwise reaction and corresponding size distribution histograms: (a) IrS12: second growth; PVP/Ir = 5, (b) IrS13: third growth; PVP/Ir = 2.5, (c) IrS14: fourth growth; PVP/Ir = 1.75, and (d) repeat of the seed preparation. Ir seed was prepared by n-propanol/water method. 77

Figure 4.12 TEM photographs of Ir nanoparticles synthesized by stepwise reaction (the scale bar is 20 nm) and corresponding size distribution histograms: (a) IrS21: seed; PVP/Ir = 20, (b) IrS22: second growth; PVP/Ir = 10, and (c) IrS24: fourth growth; PVP/Ir = 2.5. Ir seed was prepared by ethanol/water method. 79

Figure 4.13 UV-vis spectroscopy of PVP-stabilized Ir nanoparticles and the precursor H_2IrCl_6. 80

Figure 4.14 (a) IrS21/γ-Al_2O_3 and (b) IrS21/γ-Al_2O_3 after reaction. 81

Figure 4.15 TEM photographs of bimetallic Pd-Ir colloids (the scale bar is 20 nm) and corresponding size distribution histograms: (a) Pd3Ir1_1, (b) Pd3Ir1_2, (c) Pd1Ir1_1, (d) Pd1Ir1_2, (e) Pd1Ir3_1, and (f) Pd1Ir3_2. 84

Figure 4.16 TEM photographs of bimetallic Ir-Ru colloids (the scale bar is 20 nm) and corresponding size distribution histograms: (a) Ir3Ru1_1, (b) Ir1Ru1_1, and (c) Ir1Ru_1. 86

Figure 4.17 TEM photographs of bimetallic Pd-Ru colloids (the scale bar is 20 nm) and corresponding size distribution 87

histograms: (a) Pd3Ru1_1, (b) Pd3Ru1_2, (c) Pd1Ru1_1, and (d) Pd1Ru3_2.

Figure 4.18 TEM photographs of bimetallic core-shell colloids prepared via hydrogen-sacrificial technique (the scale bar is 20 nm) and corresponding size distribution histograms: (a) Pd(c)Ir(s) and (b) Pd(c)Ru(s). 89

Figure 4.19 TEM image of spent Pd(c)Ir(s)/γ-Al_2O_3. 90

Figure 4.20 Low-pressure ring opening of indan over industrial Pt-Ir catalyst (0.208g): (a) indan conversion, (b) selectivity to single cleavage, and (c) selectivities to ring opening products. Reaction conditions: indan flow rate was 2.4 $\times 10^{-5}$ g/min, H_2/Indan molar ratio was 10136, reaction temperature was 336 ^{o}C, and reaction pressure was 1 atm pressure.

Reaction products: Benzene (□), toluene (■), ethylbenzene (△), o-xylene (▲), n-propylbenzene (◇), 2-ethyltoluene (◆), lights (○), others (●). 97

Figure 4.21 Comparison of catalytic activity among synthesized monometallic catalysts and industrial polydispersed Pt-Ir catalysts. Reaction conditions: indan flow rate was ranging from 2.2 to 3.3 $\times 10^{-5}$ g/min, H_2/Indan molar ratio was ranging from 7377 to 11066, reaction temperature was 336 ^{o}C, reaction pressure was 1 atm pressure, and metal loading was 1.2 mg for all catalysts. 99

Figure 4.22 Low-pressure ring opening of indan over synthesized Pd(c)Ir(s) nanocatalyst (metal loading 1.2 mg): (a) indan conversion, (b) selectivity to single cleavage, and (c) selectivities to ring opening products. Reaction conditions: indan flow rate was 2.1 $\times 10^{-5}$ g/min, H_2/indan 106

molar ratio was 11584, reaction temperature was 336 ^{o}C, and reaction pressure is 1 atm pressure.

Reaction products: Benzene (□), toluene (■), ethylbenzene (△), o-xylene (▲), n-propylbenzene (◇), 2-ethyltoluene (◆), lights (○), others (●).

Figure 4.23 Comparison of catalytic activity among synthesized Pd-Ir bimetallic catalysts and industrial polydispersed Pt-Ir catalysts. Reaction conditions: indan flow rate was ranging from 2.2 to 3.6 $\times 10^{-5}$ g/min, H_2/Indan molar ratio was ranging from 6758 to 11058, reaction temperature was 336 ^{o}C, reaction pressure was 1 atm pressure, and metal loading was 1.2 mg for all catalysts. 107

Figure 4.24 Comparison of catalytic activity among synthesized Ir-Ru bimetallic nanocatalysts and industrial polydispersed Pt-Ir catalysts. Reaction conditions: indan flow rate was ranging from 2.5 to 3.0 $\times 10^{-5}$ g/min, H_2/Indan molar ratio was ranging from 8109 to 9731, reaction temperature was 336 ^{o}C, reaction pressure was 1 atm pressure, and metal loading was 1.2 mg for all catalysts. 110

Figure 4.25 Comparison of catalytic activity among synthesized Pd-Ru bimetallic nanocatalysts and industrial polydispersed Pt-Ir catalysts. Reaction conditions: indan flow rate was ranging from 2.2 to 4.6 $\times 10^{-5}$ g/min, H_2/Indan molar ratio was ranging from 5289 to 11058, reaction temperature was 336 ^{o}C, reaction pressure was 1 atm pressure, and metal loading was 1.2 mg for all catalysts. 113

Figure A1 TEM photographs of repeated (a) PdS1, (b) PdS2, (c) PdS3, and (d) PdS4 and corresponding size distribution histograms. 122

Figure A2 TEM photographs of repeated (a) Pd3 and (b) Pd4 and corresponding size distribution histograms. 123
Figure A3 TEM photographs of repeated (a) Ru1, (b) Ru4, and (c) RuS3 and corresponding size distribution histogram for Ru4. 124
Figure A4 TEM photographs of repeated (a) Pd1Ir3_2, (b) Ir1Ru1_1, and (c) Pd(c)Ir(s) and corresponding size distribution histograms. 125
Figure C1 Product evaluation for ring opening of indan by GC-MS analysis. (Mixture of indan and RO products). 132

Nomenclature

A_T	Total GC area
A_i	GC area of ring opening product *i*
A_{indan}	GC area of indan
C_{As}	Concentration of indan at catalyst surface
C_{WP}	Weisz-Prater parameter
D	Diffusion coefficient
d	Mean diameter of nanoparticles
d_{at}	Atomic diameter
d_i	Diameter of nanoparticle *i*
D_e	Effective diffusivity
d_{rel}	Relative nanoparticle diameter
d_{sph}	Diameter of a sphere
d_0	Particle diameter in the starting solution
ε	Porosity
m	Number of atoms lying on an equivalent edge (corner atoms included)
ϕ_i^2	Reaction rate evaluated at C_{As} divided by rate of diffusion
η	Observed reaction rate divided by rate evaluated at C_{As}
n	Total number of nanoparticles
n_i	Quantity of metal ions
n_m	Quantity of the metal particles
N_S	Number of surface atoms
N_T	Number of total atoms
n_u	Number of atoms in the unit cell
$N(C_j^{p,q,r,\cdots})$	Number of atoms with a specified number and arrangement of nearest neighbors.
r	Radius of catalyst particle

$-r_A^{'}$	Reaction rate of A
ρ_c	Catalyst density
S_i	Selectivity for product *i*
δ	Constrictivity
T	Temperature
τ	Tortuosity
V_u	Volume of the unit cell
X	Indan conversion

Abbreviations

AAS	Atomic absorption spectroscopy
BDE	Bond dissociation energies
c	Core
CN	Cetane number
EDX	Energy-dispersive X-ray
EDTA	Disodium ethylenediamine tetraacetate
EG	Ethylene glycol
EtOH	Ethanol
EXAFS	Extended X-ray absorption fine structure spectroscopy
FCC	Fluid Catalytic Cracking
fcc	Face-centered cubic
GC	Gas chromatography
hcp	Hexagonal close-packed
HR	High resolution
IR	Infrared
LCO	Light cycle oil
M	Metal
MCP	Methylcyclopentane
MP	Methylpentane
MW	Molecular weight
NAA	Neutron activation analysis
PVP	Poly-(vinylpyrrolidone)
PPO	Poly-(phenylene oxide)
n-PrOH	*n*-Propanol
RO	Ring opening
s	Shell
SRO	Selective ring opening

TEM	Transmission electron microscopy
THF	Tetrahydrofuran
TO	Truncated octahedron
TOF	Turnover frequency
ToF-SIMS	Time-of-flight secondary ion mass spectrometry
TOS	Time on stream
UV	Ultra-Violet

1. Introduction

Environmental, health, and global climate change concerns have prompted worldwide regulatory actions on gasoline and diesel specifications to limit emissions of hydrocarbons, carbon monoxides, nitrogen oxides and particulate matter, especially for heavy crude oil, which have higher aromatics and sulfur contents as compared to conventional crude oil. Sulfur and aromatics in fuel contribute to exhaust gas emissions. Nowadays, refining industry faces the significant challenges for the simultaneous decrease in the quality of crude oils and increase in demand for the best fuel possible. A catalytic ring opening (RO) of naphthenes, serving as one of the upgrading steps during hydroprocessing of heavy crude oils, is a preferred reaction for improving the cetane number (CN). During the selective ring opening (SRO) reaction, naphthenic ring is only cleaved once, maintaining the same number of carbon atoms, as contrary to hydrogenolysis and cracking. However, not all selective ring opening leads to higher CN; only ring opening at the substituted carbon - carbon bonds improves CN, whereas ring opening at unsubstituted C-C bonds improves octane number (ON).

Platinum group metals are known to selectively catalyze the ring opening of naphthenes. However, the most significant drawback of the Pt catalysts for fuel hydrotreating applications is their very low sulfur tolerance [1]. Previous studies indicated increasing sulfur tolerance by alloying Pt with another metal, for example Pd. The synergetic effect of Pt-Pd system decreases Pt electron-deficiency as compared to monometallic Pt, which in turn lowers the strength of the sulfur metal bond, thus, leading to improved sulfur tolerance and better activity [2]. Since 1970s, Exxon introduced Pt-Ir catalysts in reforming units,

which were several-fold more active and stable (lower rate of deactivation) than Pt. Ir ensures high RO activity and low coke formation; the addition of Pt tempers the undesirable excessive cracking by Ir, increases its sulfur tolerance and resistance to agglomeration [3]. Conventional Pt-Ir catalysts are prepared by traditional impregnation/calcination technique, which does not allow precise control of bimetallic nanoparticle structure and size.

Theoretically, bimetallic particles may form random alloy, cluster-in-cluster, core-shell, and inverted core-shell structures with hetero- and homo-bonds. The structure and size of bimetallic nanoparticles could be strongly affected by the synergism between the two metals in terms of electronic and geometric effects, as well as the occurrence of mixed sites [4]. Thus, by precisely changing the atom position and its surroundings, the catalytic properties can be controlled on an atomic level. Recent tremendous success in colloid chemistry techniques allows easy preparation of a desirable bimetallic particle of a desirable size [5, 6]. This opens unprecedented opportunities for catalytic technologies, since catalytic properties may change dramatically with only a 1 nm difference in particle size.

This project is focused on the development of Pt-free bimetallic nanoparticles of controlled size and structure and evaluation of their catalytic performance in low-pressure ring opening of benzocyclopentane (indan) to improve the cetane number of fuels. The hypothesis is that the nanoparticle preparation method could lead to improved activity and selectivity as compared to traditional Pt-containing catalysts.

The project objectives are the followings:

- To synthesize series of bimetallic Pd, Ir, and Ru nanoparticles with various precisely controlled composition and sizes, and to study their catalytic performance in RO of benzocyclopentane (indan);

- To find correlations between the nanoparticle composition and size and its catalytic activity and selectivity, and to propose the optimal catalytic system to increase CN of fuels.

2. Literature review

2.1. Methods of nanoparticle stabilization

2.1.1. General methods of nanoparticle stabilization

The most common metal nanoparticle structures studied are nanospheres, nanocubes, nanotetrahedrons, nanorods, and nanowires. They are isolable particles of size between 1 and 50 nm. Among them, the most studied metal particle structure is nanosphere, since thermodynamics imposes that nanoparticles grow perfectly into a spherical shape [5, 7]. Cuboctahedrones are nearly sphere structures containing {100} and {111} crystal faces with minimum surface energy as compared to other crystal shapes. Metal nanoparticles are thermodynamically unstable, because their surface free energy is excess to their lattice energy, which is due to nanoclusters' enormous surface areas relative to their masses. To prevent agglomeration, protective agents are therefore essential in order to outweigh the attractive van der Waals forces by the repulsive electrostatic and steric forces between adsorbed ions and associated counterions [5]. Based on the type of protecting shells, the stabilization of metal nanoparticles during their synthesis can be by classified as electrostatic, steric, electrosteric, ligand, and solvent stabilizations [5, 8]. However, some stabilizers (such as polymers or surfactants) can block the active sites of nanoparticles, so they must be removed prior to the catalytic reactions.

The basic theory and examples of each stabilization method are described in the following sub-sections.

2.1.1.1. Electrostatic stabilization

Electrostatic stabilization is achieved by electrical double layers around the metal particles' surfaces, which results from interaction of anions and cations with the surfaces of metal nanoparticles. For example, ionic liquids are favorable media for the electrostatic stabilization of preformed metal nanoparticles at room temperature [5, 8], although ionic liquids have some drawbacks like difficulty of purification, etc. If the double layer has sufficiently high potential energy, metal nanoparticles are prevented from agglomeration by electrostatic repulsion. However, the electrostatically stabilized metal clusters can coagulate easily if the ionic strength of the dispersing medium is increased sufficiently for the double layer to become compressed. Both the total charge on the surface of the metal clusters and the polarity of the solvent have effects on the stabilization of metal nanoparticles [5, 9].

2.1.1.2. Steric stabilization

Steric stabilization of metal nanoparticles is achieved through the steric bulk of large organic polymers' framework. When using a linear polymer (poly-(vinylpyrrolidone), PVP) as a stabilizer, the carbonyl groups of PVP (Fig. 2.1) coordinate to the metal atoms; part of the main chain of PVP are adsorbed on the surface of the nanoparticles. Instead of forming strong bonds on specific sites of the particles, polymers create many weak bonds with the metal nanoparticles' surfaces [5, 7, 8]. Somorjai et al. studied the vibrational spectra of PVP-stabilized Pt and Rh nanoparticles by deep UV-Raman and Fourier transform infrared spectroscopy. Raman spectra showed selective enhancement of C=O, C-N, and CH_2 vibrational modes of the pyrrolidone ring as a result of donor-acceptor interactions between PVP functional groups and surface metal atoms [10].

Figure 2.1 shows two major polymer families, poly-(vinylpyrrolidone) (PVP) and poly-(phenylene oxide) (PPO) [8]. PVP is the most commonly used polymer for metal nanoparticle stabilization and catalysis, because it fulfills both steric and ligand requirements. According to Toshima's alcohol reduction method, PVP protected metal (for example, Pd, Pt, Rh, and Au) nanoparticles were synthesized by the reduction of the corresponding metal halide in refluxing alcohol (such as ethanol) in the presence of PVP [5, 8, 12]. For example, a mean diameter of monodispersed palladium nanoparticles could be controlled from 17 to 30 Å in a one-step reduction reaction by changing the amount of protective polymer, PVP, and the kind and/or the concentration of alcohol in the solvent [11].

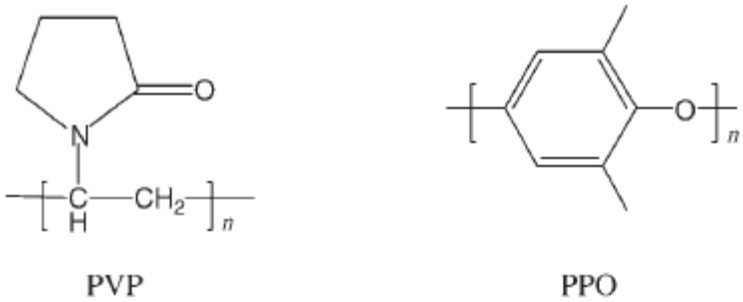

(a) poly-(vinylpyrrolidone) (b) poly-(phenylene oxide)

Figure 2.1. Two major polymer families, PVP and PPO, often used as nanoparticle stabilizers. Reprinted with permission from [8].

2.1.1.3. Electrosteric stabilization

Electrosteric stabilization is a combination of electrostatic and steric stabilizations, which prevents the metal nanoparticles from agglomeration. Polymers or surfactants are adsorbed on the surfaces of metal nanoparticles during electrosteric stabilization. The sterically demanding shields, which coordinate strongly to the surfaces of the metal nanoparticles, are very well solvated in the

respective medium (organic or aqueous phase) [5]. An example of electrosteric stabilizers is tetrabutylammonium halide, which is shown in Figure 2.2. Metal nanoparticles were obtained by reduction of a metal chloride salts in the presence of tetra-N-alkylammonium cations. The halide anions provided electrostatic stabilization; and the tetrabutylammonium cations provided steric stabilization. Furthermore, the stabilization of metal nanoparticles by anions, such as chloride or others, also have an important steric stabilization effect [8].

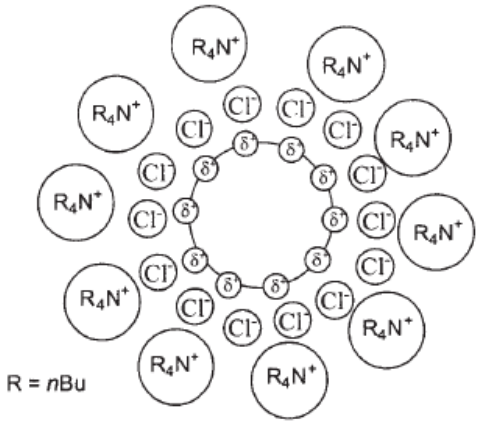

Figure 2.2. Electrosteric stabilization of metal nanoparticles by tetrabutylammonium halide. Reprinted with permission from [8].

2.1.1.4. Ligand stabilization

Ligands are ions or molecules, whose functional group binds to a central metal atom to form a coordination complex; for example, thioethers as stabilizers to control the size of metal nanoparticles. As such, monodispersed palladium nanoparticles with sizes ranging from 1.7 to 3.5 nm were accomplished in a one-step procedure. Nanoparticle size and size distribution were controlled by modulation of the reaction temperature, reaction time, solvent, and carbon chain length of the thioether [13]. The mean diameters of palladium, platinum, rhodium

and Pd-Pt nanoclusters stabilized by various ligands ranging from 1.3 to 3.2 nm were prepared by a one-step reaction, and 2.2 to 4.0 nm were prepared by stepwise growth method [14]. Schmid first described the ligand-stabilized Au_{13} clusters with icosahedral structure in 1981; whereas the ligand-protected $Au_{55}(PPh_3)_{12}Cl_6$ cluster was found to take up the cubic closed packed structure of bulk gold. The reduction of $(PPh_3)AuCl$ with B_2H_6 in benzene yielded $Au_{9,2}(PPh_3)_2Cl$, which was characterized by means of molecular weight determinations as $Au_{55}(PPh_3)_{12}Cl_6$ [5, 15].

2.1.1.5. Solvent stabilization

Electrostatic stabilization by solvents arises from donor properties of the respective liquids. Tetrahydrofuran (THF) and propylenecarbonate are often used for nanoparticle stabilization [5]. As an example, the hydrogen-free organosol $Ti^0 \cdot 0.5THF$ was prepared by the reduction of $TiBr_4 \cdot 2THF$ using $K[BEt_3H]$. According to geometric structure analysis, this metal nanoparticle colloid consists of small Ti particles in the zero-valent state, stabilized by intact THF molecules [16].

2.1.2. Size control in stabilization of metal nanoparticles with PVP

Among the mentioned stabilizations in previous section, steric stabilization is the most effective method and PVP is the most often used stabilizer in catalysis. PVP as a stabilizer can provide different sizes and shapes of metal nanoparticles, which leads to different catalytic properties of the latter. Parameters such as PVP concentration, reducing agent nature, solvent composition, temperature, and others, have to be varied to control the size of the metal nanoparticles. Sometimes, a stabilizer can also act as a reducing agent; for example, both PVP and ethylene

glycol in the synthesis of palladium nanorods were reducing agents. PVP was also reported as a reducing agent in gold and silver hydrosols preparation [5, 7, 13].

2.1.2.1. Effect of PVP concentration

Among all the parameters, PVP has been successfully used to control the size of the metal nanoparticles through varying its concentration, i.e., the higher the PVP concentration in solution, the smaller the metal nanoparticle sizes. It is reported that, for polymer concentration higher than 50 mg/L, fully developed steric layers are formed around the particles; these layers act as an effective diffusion barrier that blocks further growth of the metal nanoparticles. During PVP stabilization, the carbonyl groups of PVP are considered to adsorb on the surfaces of metal nanoparticles [7]. Thus, concentration of PVP can significantly affect the growth process for the nanoparticles. Palladium nanoparticles with mean diameters of >30 Å, <30 Å, 23 Å, and 19 Å were obtained at 20 - 40% of alcohol (ethanol) [11].

2.1.2.2. Effect of average molecular weight of PVP

Molecular weight (MW) of PVP could also be a factor to control metal nanoparticles size. The higher the PVP molecular weight, the bigger the metal nanoparticles; this is due to a weaker PVP interaction with nanoparticles. A representative example is colloidal dispersions of PVP-stabilized palladium nanoparticles with various PVP average molecular weights (MW = 6,000; 25,000; 175,000; 574,000). The average diameter of palladium nanoparticles increased from 2.0 to 2.5 nm with the increasing MW of PVP. The thickness of adsorbed layer of PVP on palladium nanoparticles increased from 1.9 to 7.8 nm with the increasing MW of PVP, which has a great influence on the dispersion stability and

behavior of nanoparticles [17].

2.1.2.3. Effect of nature and concentration of alcohol

Although the concentration and molecular weight of PVP play an important role for metal nanoparticle size control, the lower limit of the particle size does not depend on the stabilizer characteristics, but the kind and concentration of reducing alcohol [11]. Alcohol reduction method in the presence of PVP was developed by N. Toshima. During the metal salts reduction, alcohols having α-hydrogen atoms are oxidized to the corresponding carbonyl compounds, for example, ethanol to acetaldehyde [5]. Both the type and concentration of alcohol can affect the size of the metal nanoparticles, because the reduction rate of metal salt is greatly affected by these two factors [11].

Among the most commonly used alcohols in the synthesis of PVP-stabilized nanoparticles, 1-propanol is a stronger reductant than ethanol, which is stronger than methanol. Since a stronger reducing agent results in a faster reduction of the metal precursors, smaller particles sizes are obtained. For example, monodispersed Pd nanoparticles of smaller diameter were obtained in the order of methanol > ethanol > 1-propanol. This indicates that a higher reduction rate of $[PdCl_4]^{2-}$ ions is an important factor in the synthesis of smaller particles [11].

In general, an increase in the concentration of the reducing agent (alcohol) increases the reduction rate of the metal ions as well, therefore, smaller metal nanoparticles [11].

2.1.2.4. Other examples of metal nanoparticle stabilization with PVP

Previous section shows only PVP-stabilized Pd nanoparticles as examples. In fact, PVP stabilizer controls not only the nanoparticle size of palladium, but also

sizes of other transition metals, such as Pt, Rh, Ru, and Ni. It has been reported that the nanocluster sizes were 5 nm, 5.1 nm, 5 nm, 4.8 nm, and 9.4 nm for Pd, Pt, Rh, Ru, and Ni, respectively, with a reaction temperature of 323 K, H_2 pressure of 2.4 MPa, and PVP/Pd molar ratio of 40. Moreover, monodispersed platinum nanoparticles with mean diameters of 1.7 - 7.1 nm were prepared by Toshima's alcohol reduction method with the presence of PVP [13, 18].

2.1.3. Crystal growth and shape control of PVP-stabilized nanoparticles

During the synthesis reaction, metal ions are reduced to metal atoms, but how do the nanoparticles form? Turkevich established a procedure for the preparation of metal colloids, and also proposed a mechanism for stepwise formation of nanoclusters based on nucleation, growth, and coagulation. Metal salts are first reduced to give zero-valent metal atoms. These colloids in solution with other metal atoms or with "sub-clusters", that have already been formed, together result in a stable "seed" nucleus of 13 metal atoms [5, 16]. This is the nucleation stage of nanoparticle formation. The formation of the full-shell cluster family is irreversible. According to La Mer's study, nucleation occurs when the concentration of metal precursor is supersaturated and above the nucleation threshold. Since the growth of any one nanocrystal is similar to all others, the initial size distribution is largely determined by the time over which the nuclei are formed and begin to grow [20].

2.1.3.1. Nanospheres

The next stage followed by nucleation is growth stage. Since the nucleation time is very short, no more cluster nuclei are created in growth stage. The remaining metal atoms are taken up by the nuclei already in existence [5].

According to thermodynamic arguments, metal atoms should nucleate and grow in a solution phase to form cuboctahedrons of spherical shape with their surfaces bounded by a mix of {111} and {100} facets [21]. Figure 2.3 (a) shows a model of face-centered cubic (f.c.c.) cuboctahedron. The symbol, C_j, denotes a surface atom with j nearest neighbors. To differentiate between atoms whose nearest neighbors are equal in number but different in arrangement, upper indices p, q, r, s, etc. are added to the symbol C_j [22]. These upper indices denote the serial numbers of the z - j missing atoms, where for p, q, r, s, in that order, always the lowest possible number is chosen. z denotes the number of nearest neighbor atoms. In an f.c.c. structure, an atom is surrounded by 12 neighboring atoms (z = 12) [7, 22]. For symmetry reasons, p corresponds to atom no. 1 for f.c.c.. The set of indices thus obtained will be abbreviated by omitting p, if corresponding to 1; q, if corresponding to 2 etc. Should all indices be left out in this way, the last one (= z - j) will be retained. For example, $C_6^{1,2,3,4,5,6} \rightarrow C_6^{6}$ and $C_8^{1,2,4,5} \rightarrow C_8^{4,5}$.

Figure 2.3 (b) shows the statistics of surface atoms for f.c.c. cuboctahedron. Relative occurrence, $N(C_j^{p,\ q,\ r})/N_S$, of the various types of surface atoms is determined as a function of crystallite size. To obtain the statistics of surface atoms, the crystallite size parameter, d_{rel} (a dimensionless quantity), is defined as the ratio of the diameter of a sphere with a volume equal to N_T times the volume occupied by an atom in the unit cell, to the atom diameter, d_{at}.

$$d_{rel} = \frac{d_{sph}}{d_{at}} = d_{at}^{-1}\left(\frac{6}{\pi} N_T \frac{V_u}{n_u}\right)^{\frac{1}{3}} \tag{2.1}$$

where V_u is volume of the unit cell, and n_u is number of atoms in the unit cell.
For an f.c.c. crystal structure, d_{rel} is determined as,

$$d_{rel} = 1.105 \times N_T^{\frac{1}{3}} \tag{2.2}$$

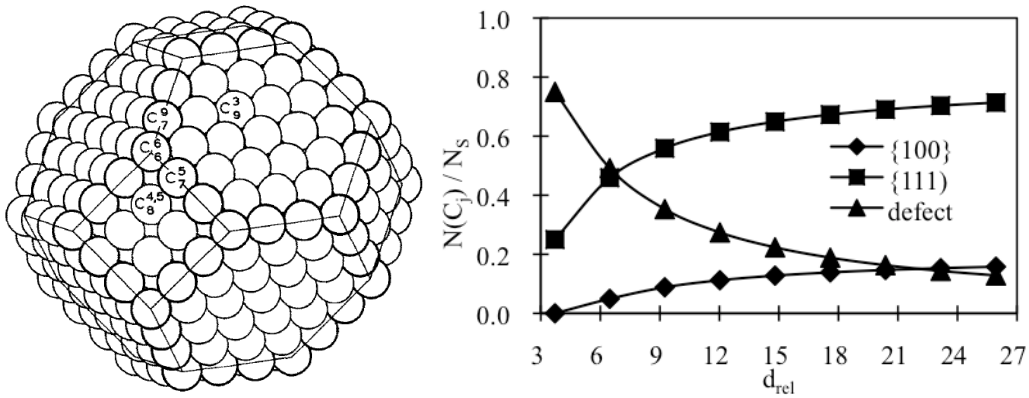

(a) (b)

Figure 2.3. (a) An f.c.c. cuboctahedron (reprinted with permission from [22]) and (b) corresponding statistics of surface atoms [22].

As Figure 2.3 (b) shows, larger particles expose mainly {100} and {111} facets, contrary to smaller clusters exhibiting mainly defect atoms on edges and vertices.

El-Sayed et al. have reported a series of PVP-stabilized Pd nanoparticles with varying sizes, which were prepared using the stepwise growth reaction [21]. The monodispersed PVP-Pd nanoperticles synthesized in a one-step reaction were used as the starting particles for stepwise growth to obtain larger particles. The obtained mean diameters of the PVP-Pd nanoparticles were 3.0 nm, 3.9 nm, 5.2 nm, and 6.6 nm for the first, second, third, and fourth stepwise reaction, respectively [21].

Another approach to prepare different sizes of PVP-stabilized palladium nanospheres is hydrogen-sacrificial technique, when hydrogen atoms chemisorbed on the seeds surfaces serving as a reductant to form a next layer of palladium atoms on the seed nanoparticles (Figure 2.4). This method leads to a wide size range of Pd nanoparticles from 1.5 nm (1st reaction) to 23 nm (15th reaction) [23]. Figure 2.5 shows TEM images of Pd nanoparticles obtained at 2nd, 5th, and 8th stepwise reactions.

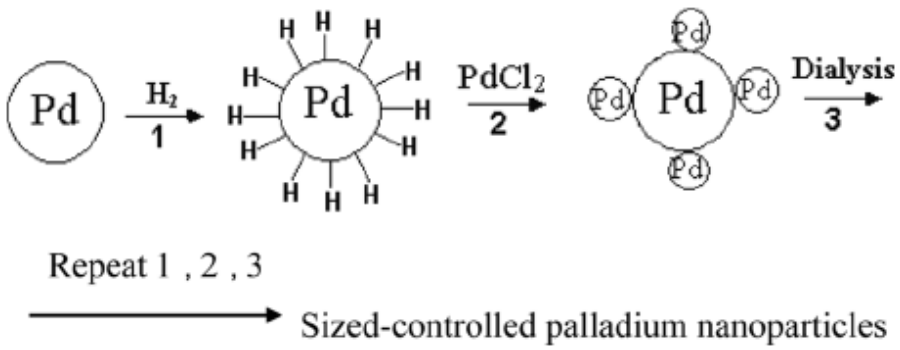

Figure 2.4. Hydrogen-sacrificial technique to synthesize metal nanoparticles. Reprinted from with permission [23].

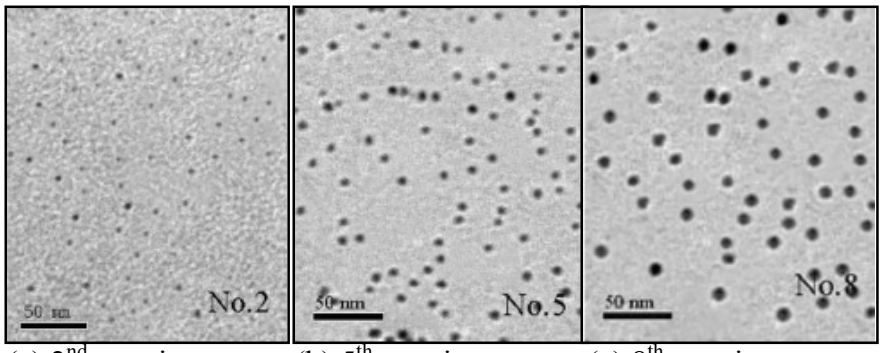

(a) 2nd reaction (b) 5th reaction (c) 8th reaction

Figure 2.5. TEM images of PVP-stabilized Pd nanospheres synthesized by hydrogen-sacrificial technique: (a) 2nd reaction, 2.51 nm diameter, (b) 5th reaction, 3.84 nm diameter, and (c) 8th reaction, 6.15 nm diameter. Reprinted from with permission [23].

2.1.3.2. Nanocubes

Other than the size control of the metal nanoparticles, stabilizer (PVP) and reducing agent (alcohol) can also affect the shape of the metal nanoparticles. Thermodynamics imposes that metal atoms grow perfectly into a spherical shape; however, anisotropic nanostructures, such as nanocubes, nanotetrahedrons, nanobars, nanorodes, and nanowires, can be also synthesized under kinetic and

thermodynamic controls [21]. Among the transition metals, the morphology of Pt nanoparticles has been most extensively studied [24].

Nanocube is a crystal bounded by {100} facets [21]. Figures 2.6 (a) and (b) show a model of f.c.c. cube and corresponding statistics of surface atoms.

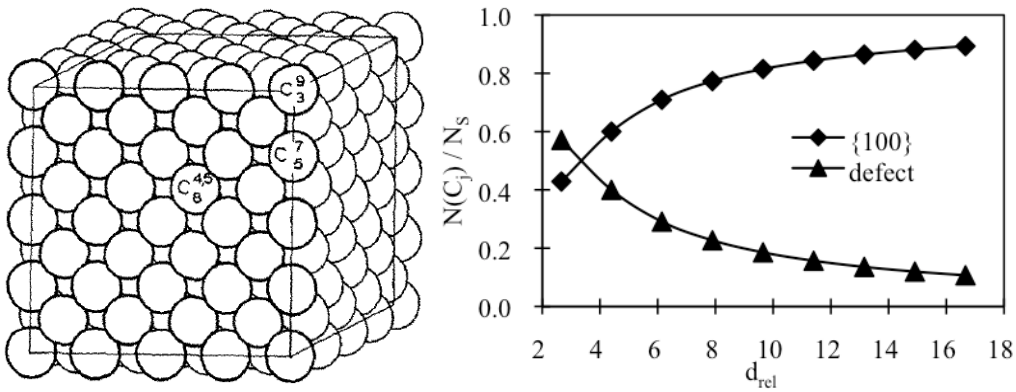

(a) (b)

Figure 2.6. (a) An f.c.c. cube (reprinted from with permission [22]) and (b) corresponding statistics of surface atoms [22].

Small nanoparticles, formed during the early stages of growth or at high concentration of capping polymer, displayed distribution with a dominance of shapes having the stable {111} faces. Initially or at high polymer-to-Pt molar ratio, capping of the tetrahedral nanoparticles took place. As growth continued or at low polymer-to-Pt concentration, the tetrahedral nanoparticles were then transformed into truncated octahedrons and eventually into cubic shapes [25]. Mechanism for the formation of polymer-stabilized Pt nanocubes is shown in Figure 2.7 (a) and (b).

Silver nanocubes and nanotetrahedrons with truncated corners or edges have been synthesized by polyol reduction method. Silver nitrate was reduced by

ethylene glycol in the presence of PVP and a trace amount of sodium chloride. Previous studies proposed that the defects inherent in twinned nuclei of silver led to their selective etching and dissolution by chloride and oxygen, leaving only the single crystalline ones to grow into nanoscale cubes and tetrahedrons [26] (Figure 2.8).

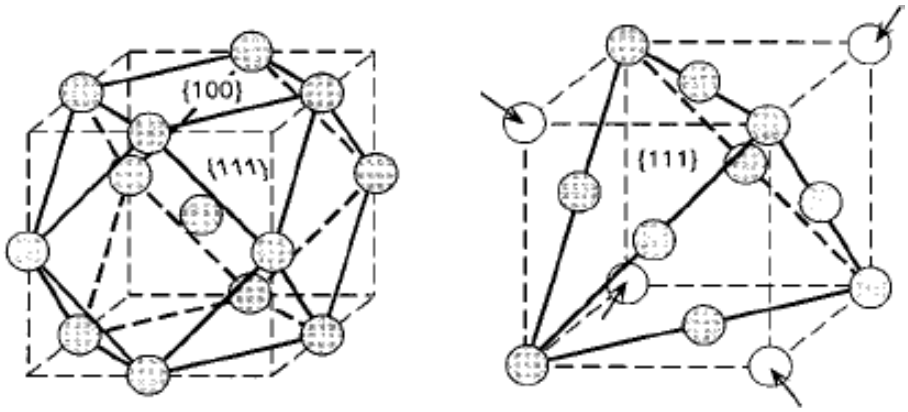

(a) Truncated octahedron (TO) (b) Tetrahedron to TO and to cube

Figure 2.7. Mechanism of the formation of Pt nanocubes in presence of polymer. Reprinted with permission from [25].

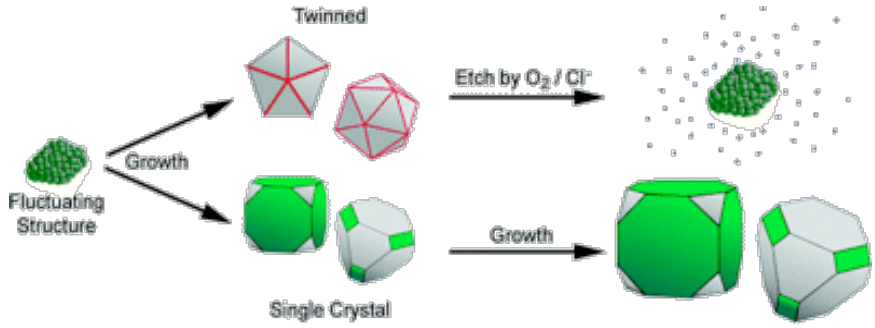

Figure 2.8. Formation of silver nanocubes and nanotetrahedrons by polyol reduction method in the presence of PVP and a trace amount of sodium chloride. Reprinted with permission from [26].

2.1.3.3. Nanotetrahedrons

Nanotetrahedrons have sharp edges and corners; and atoms are chemically and dynamically active [6]. Figures 2.9 (a) and (b) show a model of f.c.c. tetrahedron and corresponding statistics of surface atoms. Figure 2.10 is a high resolution image of a truncated tetrahedral nanoparticle.

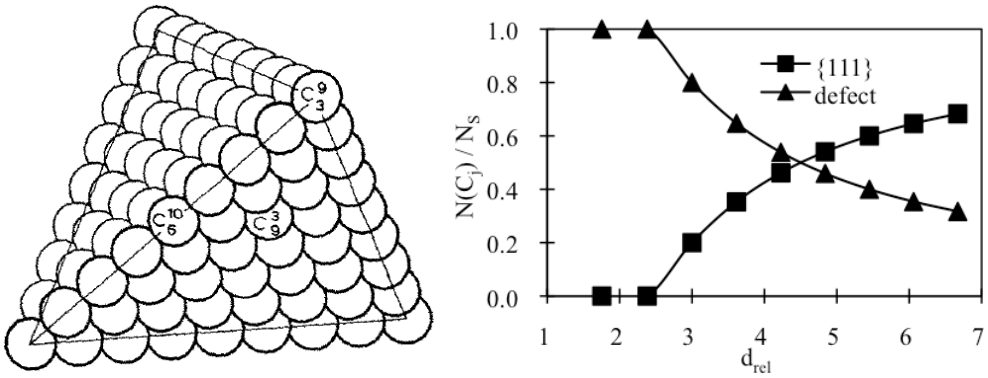

(a) (b)

Figure 2.9. (a) An f.c.c. tetrahedron (reprinted with permission from [22]) and (b) corresponding statistics of surface atoms.

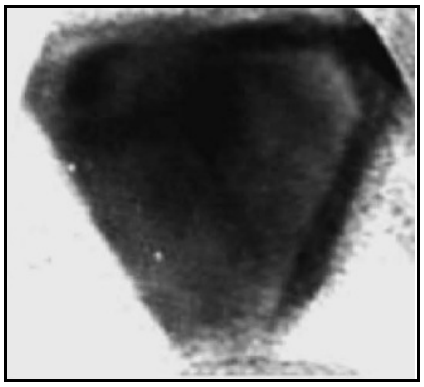

Figure 2.10. High resolution image of a truncated tetrahedral (triangular) particle. Reprinted with permission from [24].

Tetrahedral nanoparticles were predominant products during the hydrogen

reduction of H_2PtCl_6 or K_2PtCl_6 in the presence of PVP; whereas, the reduction with methanol generated mainly truncated octahedral particles. Slow H_2 reduction of Pt^{4+} ions favorably led to the formation of tetrahedral Pt nuclei enclosed with four {111} planes [6, 27]. For example, PVP-stabilized Pt nanoparticles synthesized by hydrogen reduction method showed 55% regular tetrahedral, 22% distorted tetrahedral, and 23% spherical nanoparticles (Figure 2.11) [6].

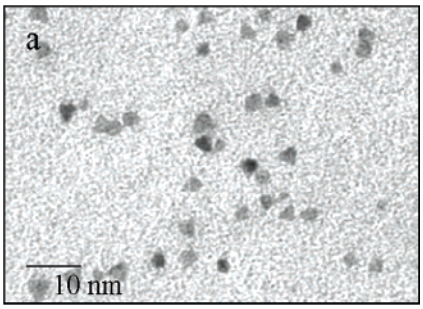

Figure 2.11. TEM image of PVP-stabilized Pt nanoparticles (55% regular tetrahedral, 22% distorted tetrahedral, and 23% spherical nanoparticles). Reprinted with permission from [6].

2.1.3.4. Nanobars and nanorods

If synthesis reactions are under kinetic control, other shapes of nanoparticles such as nanobars and nanorods could be also obtained. PVP-stabilized Pd nanostructures were synthesized by ethylene glycol reduction of sodium palladium (II) chloride in the presence of KBr. When the reduction rate was in the medium region, the seeds took a cubic shape with slight truncation at the corner, and the product contained were mainly nanobars (Figure 2.12 A). As the reduction rate became much faster, more seeds were formed in the nucleation step with smaller sizes and more significant truncations at corners, and the final product contained mostly nanorods (Figure 2.12 B) [21]. Single crystal nanobars are

bound by {100} facets; and single crystal nanorods are characterized by {100} and {110} facets.

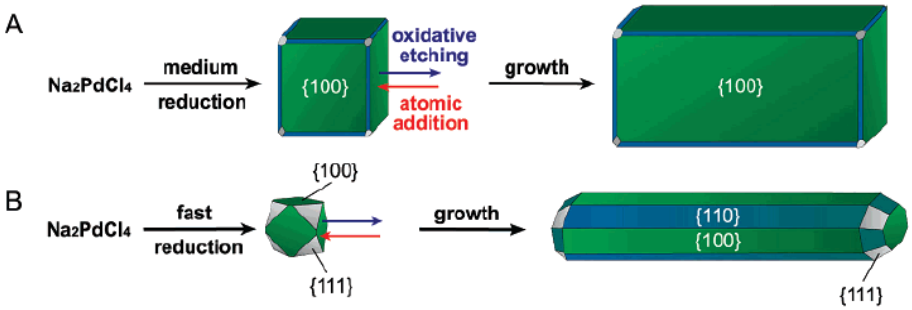

Figure 2.12. Nucleation and growth: kinetic control. A, nanobars and B, nanorods. Reprinted with permission from [21].

Previous results show that a faster reduction at a higher EG concentration induced anisotropic growth for the nanocrystals. Slow and medium reduction rates favored the formation of Pd nanobars of 8 nm width and 6 nm width, respectively; while fast reduction rate favored the formation of Pd nanorods of 2 nm diameter. The yields of Pd nanobars and nanorods were typically > 95% [21]. Figure 2.13 (a) and (b) are examples of PVP-stabilized Pd nanobars and nanorods, respectively.

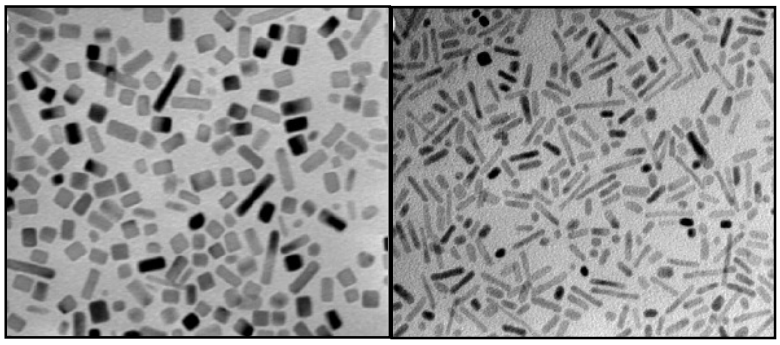

(a) nanobars (b) nanorods

Figure 2.13. TEM images of PVP-Pd: (a) nanobars, 9.1% EG in solution and (b) nanorods, 72.2% EG in solution. Reprinted with permission from [21].

2.1.4. Bimetallic catalysts

2.1.4.1. Synergism

As industrial Pt containing catalysts show deactivation by sulfur poisoning, many studies have been focused on increasing S-tolerance by alloying the active component with another metal, and promote the catalytic activity via synergism. It is important that the addition of the second metal does not simply "add" its catalytic activity but often leads to synergism. Coq and Figueras's review on bimetallic Pd catalysts concluded that the promotion of one metal by addition of a second metal is described in terms of electronic effects, geometric effects, and the occurrence of mixed site [4].

Electronic effect. The key point of electronic effect is the interaction between the *d*-band orbitals of the surface sites with molecular orbitals of reactants and products. The heat of adsorption of reactants and products, governed by the electronic factors, should be neither too strong nor too weak to give the optimum coverage for species competing at the surface, or for the products to desorb [4]. The degree of electronic interaction between valence electrons of the two metals in alloys depends on the enthalpy: interaction is low if enthalpy is positive and strong if enthalpy is negative [4, 28]. Fuggle et al. have concluded that in alloys with electropositive elements the Pd *d*-band is filled and moved away from the Fermi level with narrowing the width of *d*-band; as the electronegativity difference between the two metals increases, there is a greater overlap in the band energies of Pd and second metal; the filling of bands is largely due to changes in the hybridization of the Pd *d*-band, and the actual charge transfer of Pd *d* electrons is probably small [4, 29].

Geometric effect. The key point of geometric effect is that the reaction rate is a function of the probability to find an ensemble of *n* free and neighbor atoms on which the adsorption of the reactant and the further transformation can occur. When an active metal and an inactive metal are alloyed, the ensembles of active surface are diluted by the inactive metal. These smaller ensembles of active metal being less prone to activate the reactant thus lower the catalytic turnover frequency (TOF) [4]. This is true only if the active metal and the inactive metal are randomly distributed on an infinite surface, which requires a slightly negative enthalpy; whereas a positive enthalpy leads to form clusters [4].

Mixed sites. Mixed site is an active site where both metals of the alloys participate in the catalytic transformation. Sometimes, the mixed site could result in a higher activity than any of the metal component, which can be achieved by alloying two transition metals, for example, mixed Pd-Ni sites show a better catalytic activity in the hydrogenolysis of C_2H_6 [4, 30].

2.1.4.2. Preparation

The preparation of bimetallic nanoparticles has been widely studied. Among them, Toshima et al. have made great contribution to the synthesis of bimetallic nanoparticles with precisely controlled composition and size. Two methods used to synthesize bimetallic catalysts are: chemical and physical methods. The former method is superior to the latter, with respect to the easy preparation, stability, small size, and narrow size distribution of the clusters [31]. Two commonly used reduction techniques in chemical method are simultaneous reduction (or co-reduction) and successive (or two-stepped) reduction of two kinds of metal ions. Theoretically, bimetallic particles may form a random alloy, core-shell, and inverted core-shell structures (Figure 2.14) [5].

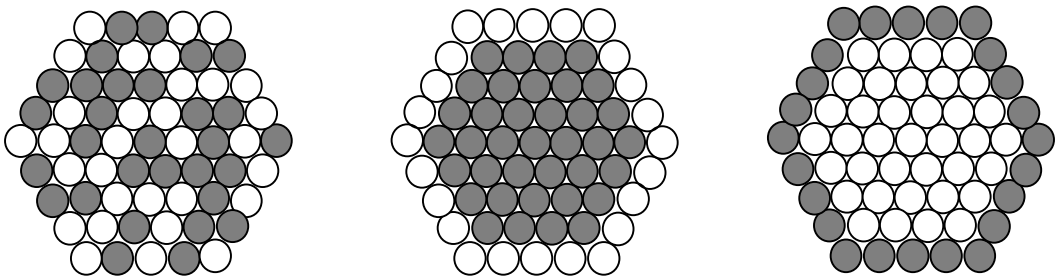

(a) Random Alloy (b) Core-Shell (c) Inverted core-shell

Figure 2.14. Various structures of bimetallic nanoparticles.

In ***successive reduction***, core metal precursors are reduced first, followed by the reduction of shell metal precursors. The core-shell structures are obtained by the formation of strong metallic bonds between the core and shell metal atoms. This method was initially developed for inverted core-shell structures (Figure 2.14 (c)), when the core should be formed from the metal with lower redox potential.

The ***simultaneous reduction*** of two metal ions with different redox potentials often leads to normal core-shell (Figure 2.15); alloys (Fig. 2.14 (a)) could also be formed is metal ratios are changed. However, it is not possible to obtain inverted core-shell structures (Figure 2.14 (c)) (due to redox potentials) [5]. The mechanism shown in Figure 2.15 includes: (1) coordination of metal ions, (2) reduction of coordinated ions to metal atoms or microclusters, (3) coagulation of one kind of atoms or microclusters to produce core clusters, and (4) deposition of another kind of metal atoms or microclusters on the surfaces of the core clusters to form the shell. The core-shell structure can be controlled by the following two factors: the reduction potential of metal ions and the coordination ability of metal atoms or microclusters to PVP.

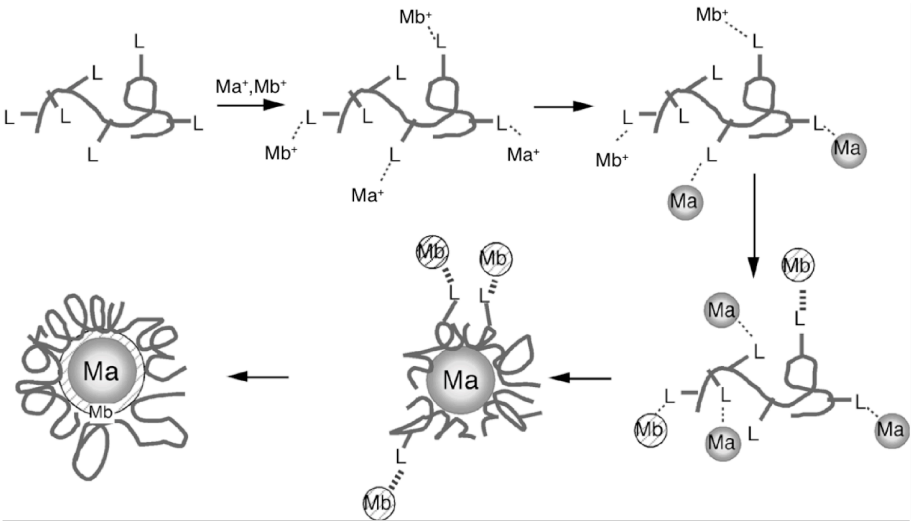

Figure 2.15. Simultaneous reduction of two metal ions in the presence of PVP leading to core-shell structures. Reprinted with permission from [32].

The synthesis of bimetallic nanoparticles with core-shell structures has been widely studied. For example, Ag(core)Pt(shell) bimetallic nanoparticles with core-shell structures were prepared by successive reduction method using Ag nanoparticles as the seeds [33]. Au(core)Pd(shell) bimetallic nanoparticles were prepared by reducing $Pd(NO_3)_2$ first, and then followed by the reduction of $HAuCl_4$ [34]. PVP-stabilized Pd(core)Ru(shell) nanoparticles with mean diameter of 2 nm were successfully synthesized by simultaneous reduction [35, 36]. Core-shell structures of bimetallic nanoparticles can be synthesized by both successive reduction and co-reduction. However, previous study on the preparation of Pd(core)Au(shell) showed that the successive method was more effective than the simultaneous one in term of the formation of the core-shell structure [5, 34].

Alloys are often formed via simultaneous reduction when metal ratios are changed. For example, Pt-Ru alloys reveal a face-centered cubic (f.c.c.) structure at Pt/Ru = 3/1, a hexagonal close-packed (h.c.p.) structure at Pt/Ru = 1/9, and a new phase comprised of twinned f.c.c. octahedrons at Pt/Ru = 1/3 [37].

Typically, the PVP-protected nanoparticles are highly stable for years [5]. Thousands of papers have been published on the preparation of noble metal nanoparticles of different controlled sizes using PVP; many of these papers are about PVP-stabilized bimetallic colloids. Toshima et al. have studied PVP-stabilized Pd-Pt bimetallic clusters synthesized by refluxing mixed solutions of $PdCl_2$ and H_2PtCl_6 in ethanol/water [31]. Figure 2.16 is an example of PVP-stabilized Pd-Au bimetallic nanoparticles prepared by simultaneously reducing Pd and Au precursors in methanol [38].

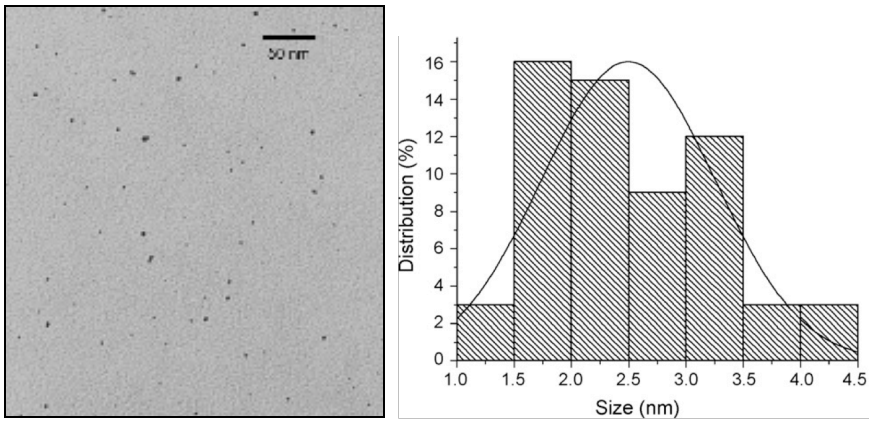

Figure 2.16. TEM image and histogram of PVP-stabilized Pd-Au bimetallic nanoparticles (molar ratio of Au/Pd = 3/1). Reprinted with permission from [38].

In order to prepare bimetallic nanoparticles with different sizes and controllable core-shell structures, successive reduction via hydrogen-sacrificial protective strategy has been developed by Toshima's group [5, 39]. The synthesized monometallic particles (core element) of different sizes are treated by hydrogen, and form metal hydrides on the metal surface. The hydrogen atoms have a very strong reducing ability due to the low redox potential. Consequently, the second metal ions are easily reduced to metal atoms by the hydrogen atoms on the surface, and form a shell. Polymer-stabilized Pt(core)Pd(shell) nanoparticles

with particle sizes of 1.5 - 5.5 nm were prepared by successive reduction via H_2 [39]. Figure 2.17 is an example of PVP-stabilized Pd-Pt bimetallic nanoparticles with core-shell structures synthesized by hydrogen-sacrificial protective method [39].

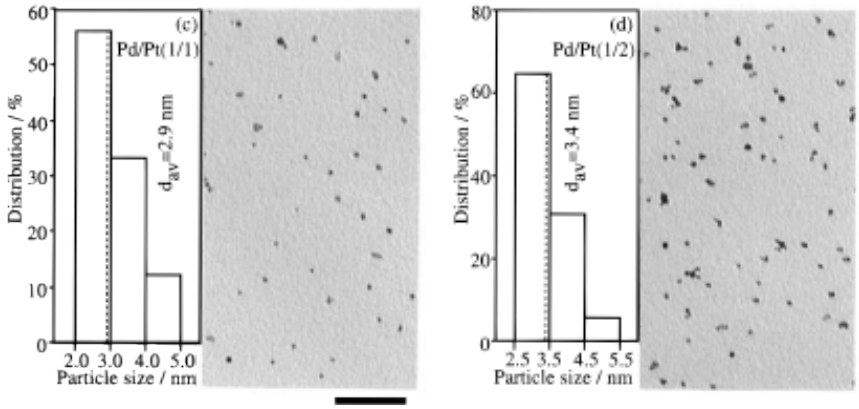

Figure 2.17. TEM images of PVP-stabilized Pd(core)Pt(shell) bimetallic colloids synthesized by hydrogen-sacrificial technique: (c) molar ratio of Pd/Pt = 1/1 and (d) molar ratio of Pd/Pt =1/2. Reprinted with permission from [39].

The formation of core-shell structures could be confirmed by different characterization techniques like UV (ultra-violet)-Visible Spectroscopy, Transmission Electron Microscopy (TEM), High Resolution TEM (HR-TEM), Extended X-ray Absorption Fine Structure Spectroscopy (EXAFS), or CO Adsorption Infrared Spectroscopy (CO-IR). Figure 2.18 shows TEM and HRTEM images of Pt(core)Ru(shell) nanoparticles, in which Pt core and Ru shell can be clearly observed.

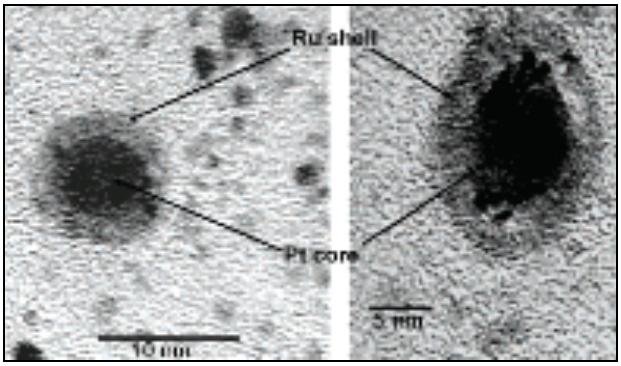

Figure 2.18. TEM images of Pt(core)Ru(shell) nanoparticles obtained via successive reduction. Reprinted with permission from [40].

2.2. Catalytic ring opening reaction

2.2.1. Introduction to oil refinery challenges: sulfur and aromatics contents

In Canada, the sulfur content of diesel fuel produced or imported was required to reduce to 15 ppm since May 2006. In the European Union, a final target in 2009 for the final sulfur content in diesel fuel was 10 ppm, which was confirmed by the European Commission.

For diesel fuel, refiners need to increase industrial capacity for the growing market demand and to meet regulations for clean fuels, such at cetane number (CN), sulfur and aromatics contents. CN measures the combustion properties of diesel fuels during compression ignition, and is one of the factors to determine the quality of diesel fuels. Cetane is an unbranched open chain alkane molecule and has a CN of 100, so the desired RO product should contain less branching. One of the options to achieve the goal of producing high demand and high quality diesel fuel is to upgrade Light Cycle Oil (LCO) into a high quality diesel-blending component. LCO is one of the recovered product groups from the Fluid Catalytic Cracking (FCC) units. It is a poor diesel fuel blending component, due to its low

CN (15 - 25) and high aromatics (80 wt.%) and sulfur (0.2 - 2.5 wt.%) contents [41]. Therefore, selective ring opening of naphthenic rings is a preferred reaction.

Table 2.1. Past diesel fuel specifications in the European Union [42].

Diesel fuel	1996	2000	2005	2009
Sulfur, maximum	500 ppm	350 ppm	50 ppm	10 ppm
Cetane number, minimum	49	51	51	51
Polyaromatics	-	11%	11%	11%

2.2.2. Selective ring opening mechanisms

The current hydrotreating technique is not enough to reduce the sulfur content to less than 10 ppm, so selective ring opening (SRO) is a preferred reaction to increase CN or ON of fuels as mentioned in previous section. SRO is defined as opening of naphthenic rings without loss of reactant molecular weight, i.e., the product molecule having the same number of carbon atoms but one less ring than the reactant [43]. There are three pathways to achieve ring opening: free radical route, acid-catalyzed carbocation route, and metal catalyzed hydrogenolysis.

Free radical route is normally initiated by pyrolysis. With this mechanism, it is very difficult to get high ring opening yields, because the reaction is limited by competitive secondary cracking and dealkylation, which is 5- to 50-fold faster than those of naphthenes of equivalent carbon number [43].

In ***acid-catalyzed carbocation route***, naphthenic molecules are activated by either direct formation of cationic species by hydride abstraction by a Lewis acid or by protonation of an olefin intermediate formed by naphthene dehydrogenation over a metal function. The system is dominated by acid function; this results in excessive cracking of side chains and products alkane cracking. Therefore, the

yields of SRO products are unacceptable low [43, 44].

In metal catalyzed hydrogenolysis, ring opening can be achieved by breaking either endocyclic or exocyclic C-C bonds of naphthenic molecules. Breaking an endocyclic C-C bond in an alkyl-substituted one-ring naphthene results in selective ring opening. For example, selective ring opening of pentylcyclopentane produces alkanes. On the other hand, breaking an exocyclic C-C bond results in non-selective ring opening. Taking the same example, pentylcyclopentane, by cracking of the alkyl substituent, ethylcyclopentane and propane could be produced, which are two lower molecular weight products. Moreover, non-selective ring opening can also be resulted if both endocyclic and exocyclic C-C bonds are broken [43]. Two groups of metals have been studied previously in ring opening of methylcyclopentane (MCP): noble VIIIB metals (Rh, Pd, Ir, Pt) and Co, Ni, Ru, Re, Os, Cu, Ag metals. The former group promoted isomerization and produced high amounts of C_6 alkanes from MCP [45].

Both free radical and acid-catalyzed carbocation routes give low SRO products yields; therefore, metal catalyzed SRO is more favorable for improvement of cetane number in heavy oil upgrading. Selective ring opening with minimum side chain cracking is difficult and presents a challenge to catalysis societies.

2.2.3. Ring opening catalysts

2.2.3.1. Acid catalysts

As discussed in the previous section, one of the pathways of ring opening is by acid catalysts, e.g., zeolites. Ring opening reaction on acid catalysts is carried out in three steps. In the first step, reaction is initiated by protolytic

dehydrogenation and protolytic cracking; and then followed by the propagation steps, in which skeletal isomerization, hydride transfer, and β-scission (ring opening) occur; at last, alkylation [46]. An example of ring opening of decalin over zeolites is shown in Figure 2.19.

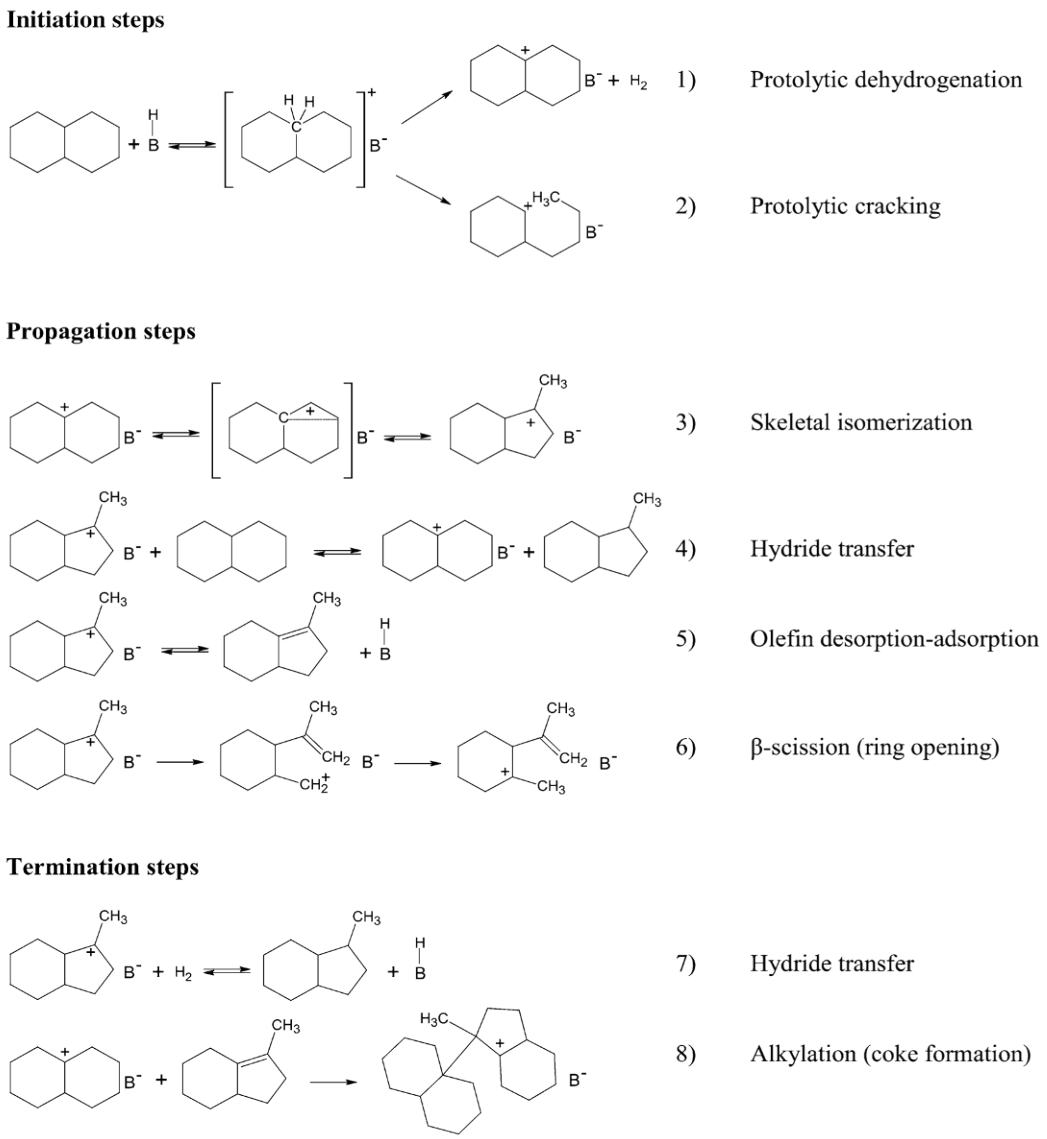

Figure 2.19. Mechanism for isomerization and ring opening of decalin over zeolites. Reprinted with permission from [46].

2.2.3.2. Bifunctional catalysts

Either acid or metal catalysts can achieve the ring opening of five-membered rings; while for the six-membered rings, acid function is required to isomerize the six-membered structures to five-membered rings (ring shrinkage). Without the acid sites (only metal function), the ring opening rate of six-membered rings will be very low, since a six-membered ring is the ideal structure for ring molecules, and therefore, the C-C bonds are more stable than those in a five-membered ring. In order to achieve optimal performance, this needs catalysts with a balanced metal and acid functionalities; or in another word, bifunctional catalysts [44]. Bifunctional catalysts contain both metal and acid functions, e.g., metals supported on zeolites. Hydrogenation and dehydrogenation occur on the metallic sites; and isomerization and cracking are carried on acidic sites [44, 46, 47]. Equations 2.3, 2.4, and 2.5 show the mechanism of bifunctional catalysts: (2.3) hydrogenation or dehydrogenation converts the reactants to olefins on metal sites; (2.4) carbenium ions are formed by protonation of olefins on the acid sites, the formed carbenium ions undergo skeletal isomerization, cracking, or alkylation; and (2.5) the olefins are then desorbed from the acid sites, and undergo hydrogenation on the metal sites [44, 48, 49].

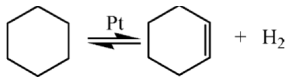

(2.3)

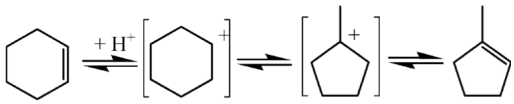

(2.4)

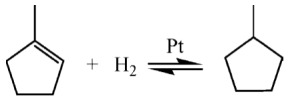

(2.5)

The most widely used bifunctional catalysts are Pt-based zeolites. An example of ring opening of decalin over Pt-zeolites bifunctional catalysts is shown in Figure 2.20.

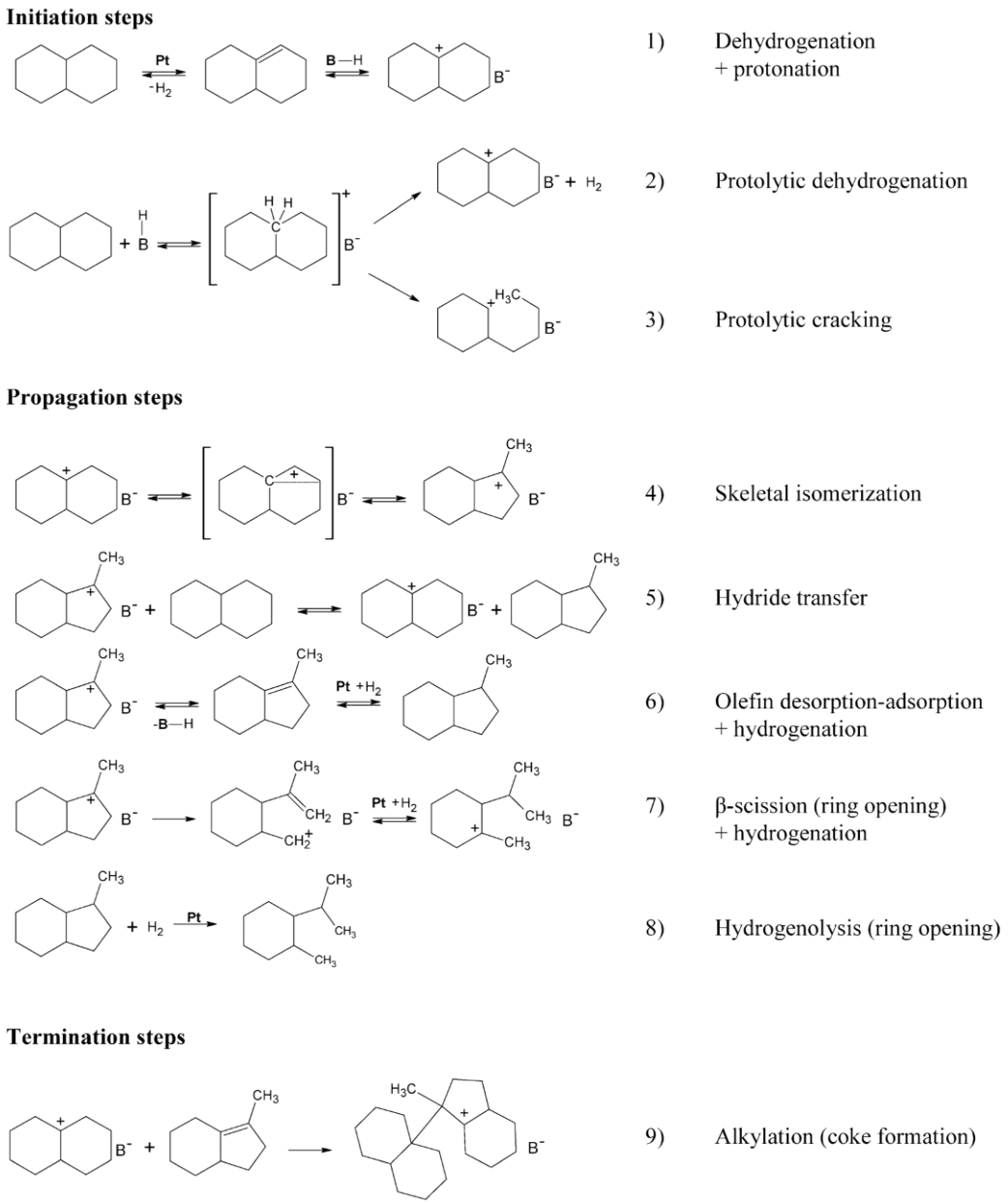

Figure 2.20. Mechanism for isomerization and ring opening of decalin over Pt-zeolites bifunctional catalysts. Reprinted with permission from [50].

2.2.4. Selective ring opening over supported noble metal catalysts

It has been reported that noble metals supported on acidic oxides are the most active catalysts for selective ring opening, but these catalysts are very sensitive to poisoning by sulfur compounds in petroleum feedstock [44].

2.2.4.1. Mechanism

All catalytic reactions are preceeded by chemisorption of reactant molecules on the active sites of catalyst. Multiplet and dicarbene are two well-known mechanisms for ring opening on metal surfaces. The main difference between these two mechanisms is the reaction intermediate formed on the metal surfaces during ring chemisorption.

In ***multiplet mechanism***, two competitive mechanisms are doublet and sextet-doublet. Doublet mechanism usually occurs on the surface of small metal particles, in which cyclic hydrocarbons physically adsorb on the edges of two metal atoms via a bisecondary C-C bond. The bisecondary C-C bond then reacts with chemisorbed hydrogen in a push-pull manner to achieve ring opening. Due to the steric hindrance, the edge-wise adsorption of the tertiary-secondary or tertiary-tertiary C-C bond is limited. In sextet-doublet mechanism, cyclic hydrocarbon is physically adsorbed flat-lying on the metal surfaces, with the carbon atoms of ring located over the interstices of the metal plane, e.g., Pt (111). For the five-membered ring cyclopentanes, one C-C bond has to be stretched (Figure 2.21), and this bond is readily attached by neighboring, adsorbed hydrogen atom, leading to hydrogenolysis of the ring [44, 48].

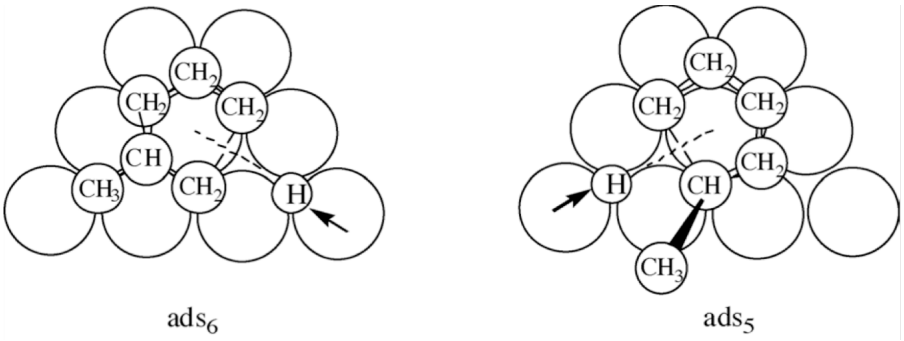

Figure 2.21. Hydrogenolysis of methylcyclopentane via the multiplet mechanism. Reprinted with permission from [48].

In the ***dicarbene mechanism***, cyclic hydrocarbon is chemisorbed on the metal surface after the rupture of several C-H bonds, and form carbon-metal bonds (Figure 2.22) [44].

In the study of 1,3-dimethylcyclohexane, Gault et al. have summarized three different RO mechanisms (Fig. 2.22); they are dicarbene, π-adsorbed olefin, and metallacyclobutane reaction paths.

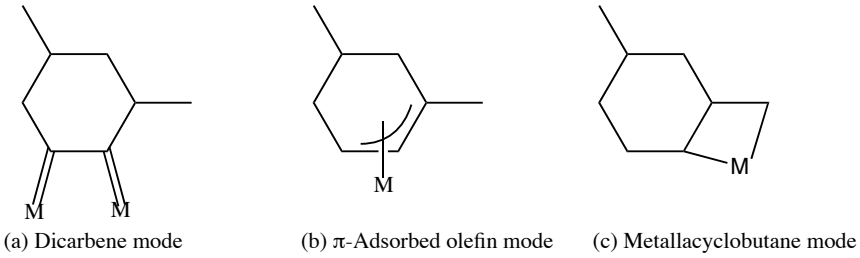

Figure 2.22. Ring opening modes of 1,3-dimethylcyclohexane. Reprinted with permission from [51].

Dicarbene reaction path results in the cleavage of unsubstituted secondary-secondary C-C bonds, thus producing highly branched isoparaffins with low CNs;

whereas, both ***π-adsorbed olefin*** and ***metallacyclobutane reaction paths*** result in C-C cleavage at substituted position. Therefore, the latter two paths are desirable for enhancing CN, because the main consequence of cleaving a substituted C-C bond is the elimination of molecular branching [48, 51].

There are many factors, such as type of metals, nanoparticle sizes, and nature of supports could affect the choice of the ring opening paths. For example, highly dispersed Pt catalysts favored C-C bond cleavage via a π-adsorbed olefin mode, whereas low dispersed Pt catalysts followed the dicarbene reaction path. π-adsorbed olefin mode requires flat adsorption of three neighboring metal atoms (lower density of active sites resulted from bigger particle size), whereas the dicarbene mode requires metal-carbon bonding of two contiguous metal atoms, with the molecule adsorbed perpendicular to the surface (higher density of active sites on the catalysts surface). In the previous study, Ir catalyst did not show the same size effect as Pt catalyst, but strong support effect. It has been reported that, with Ir/SiO_2 catalyst, ring opening of 1,3-dimethylcyclohexane preferred dicarbene mode, whereas with Ir/Al_2O_3 catalyst, metallacyclobutane was favored [51].

2.2.4.2. Effect on type of metals (mono- and bi- metallic)

Nature of metals is one of the important factors to affect the product yields during catalytic ring opening. Previous study used eleven different metals to test the ring opening of methylcyclopentane [45]. Among the monometallic catalysts tested, Ir was the most active and selective catalyst. Results showed that Ir, Rh, and Ru catalysts were very active in the following order: $Ir/Al_2O_3 > Rh/Al_2O_3 > Ru/Al_2O_3 > Re/Al_2O_3 >> Pt/Al_2O_3$. The RO selectivity was in the order of: Ir > Pt ~ Rh > Ru > Re [52].

There are numerous recent reports on improved catalytic activity of bimetallic catalysts. In 1970s Exxon introduced Pt-Ir catalysts in reforming units, which were several-fold more active and stable than Pt catalyst. Ir ensures high RO activity and low coke formation; the addition of Pt tempers the undesirable excessive cracking by Ir, thus increases its sulfur tolerance and resistance to agglomeration [3]. In bimetallic catalysts, one metal is promoted by the addition of a second metal; this leads to synergism between the two metals in terms of electronic and geometric effects, as well as the occurrence of mixed sites [4]. For example, increasing the size of particles results in an increase of electron bandwidth and a decrease of binding energies of core electron [4]. A better activity has been reported for hydrogenolysis of C_2H_6 over mixed Pd-Ni sites composed of six Ni atoms diluted in the Pd matrix [53].

In order to obtain bimetallic catalysts leading to selective RO, Marecot et al. studied the RO of MCP over several Pt-based bimetallic catalysts, such as, Pt-Ge, Pt-Cu, Pt-Ru, and Pt-Rh. Although Pt was the least active catalyst for RO of MCP as compared to other monometallic catalysts, Pt-Rh bimetallic catalyst allowed increasing RO activity and selectivity, which are similar to those of Ir catalysts [52].

Catalytic activity for hydrogenation also depends on metal composition of the bimetallic nanoparticles. It has been found that Pt(core)Pd(shell) bimetallic catalyst with a Pt/Pd molar ratio of 1/4 was the most active catalyst for the hydrogenation of 1,3-cyclooctadiene to cyclooctene [31]. From the sulfur resistance point of view, greater resistance of Pt-Pd bimetallic catalyst (as compared to their monometallic counterparts) to poisoning by sulfur compounds was confirmed by study involving the hydrogenation of toluene and naphthalene in the presence of 1200 ppm dibenzothiophene [2].

2.2.4.3. Effect on nanoparticle sizes

Another factor that could affect the catalytic performance in RO reaction is the size of metal nanoparticles. There are two main reasons for the difference of catalysts property between small and large metal nanoparticles. Firstly, as metal nanoparticle size decreases, the electronic bands of the metal particle becomes distinct, therefore, the electron energies increase. Secondly, for a smaller particles size, the number of atoms of low coordination at the edges or corners of the crystallites increases, i.e., less fraction of face atoms [44]. Such atoms possess different electronic and geometric properties, affecting the chemisorption strength and mode of reaction substrates, as catalytic reaction requires chemisorption on the metal particle surfaces.

The activity and selectivity of Pt catalysts in RO of MCP are very sensitive to nanoparticle sizes. Previous study shows that Pt/Al_2O_3 catalysts with extremely high (1.5 nm mean diameter) and low (18 nm mean diameter) dispersions behaved in very different ways in selectivity. A study on the MCP ring opening shows that highly dispersed 0.2% Pt/Al_2O_3 led to non-selective hydrogenolysis; while on the other hand, low dispersed 10% Pt/Al_2O_3 selectively ruptured the C-C bonds. Similar results were observed on Rh/Al_2O_3 catalyst [44, 54]. However, not all the metal catalysts performance is as sensitive as Pt catalysts. The hydrogenolysis of cyclopentane was slightly promoted by decreasing Pd nanoparticle size, but insensitive to Ir particles sizes [44].

Moreover, Vasudevan et al. have reported that an increase of Pd nanoparticle size from 1.7 to 4.2 nm led to 15-fold increase of the turnover frequency in 1-butyne hydrogenation [55]. Somorjai et al. have found that the ring opening of pyrrole over 2.0 nm Pt nanoparticles resulted in 90% selectivity to the RO product (n-butylamine), but lower selectivity (75%) over the 1.5 nm Pt nanoparticles [56]. A study on the methylcyclohexane ring opening shows that RO selectivity

increased from 5% over 1 nm Ir to 40% over larger Ir particle sizes [57].

2.2.4.4. Effect on acid-base supports

Catalysts selectivity and RO mechanisms also depend on the acid-base properties of the catalyst supports. Acid catalysts (e.g., gamma-alumina modified with chlorine) lead to low selectivity; while basic catalysts (e.g., gamma alumina modified with potassium) allow very high selectivity (up to 98%) [58].

2.2.4.5. Selective ring opening of methylcyclopentane (MCP)

Nowadays, catalytic SRO of heavy oil upgrading has been studied using both single-ring compound models like methylcyclopentane (MCP) and methylcyclohexane, and multiple-ring compound models, such as indan, decalin, tetralin, naphthalene, and phenanthrene, etc. The RO mechanism has been widely studied over mono- and bimetallic catalysts.

The ring opening of MCP over supported metal catalysts has been extensively studied for the octane number increase. SRO of MCP results mainly in 2-methylpentane (2MP) (β-ring opening) and 3-methylpentane (3MP) (γ-ring opening); while non-selective ring opening of MCP (in terms of octane number increase) results in the mixture of n-hexane (α-ring opening), 2MP, and 3MP (Fig. 2.23) [58]. Generally, activity and selectivity depend on the type of metals, metal particle sizes, and nature of supports [44, 58]. Studying the properties of metal catalysts helps to understand the mechanism of ring opening reaction. Here shown below is the RO of MCP as an example (Fig. 2.23).

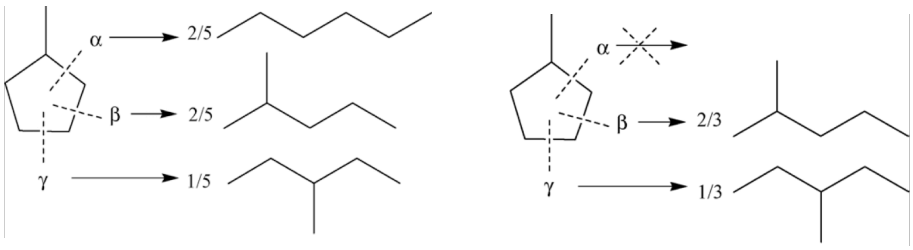

(a) (b)

Figure 2.23. (a) Non-selective and (b) selective hydrogenolysis of methylcyclopentane from the viewpoint of octane number increase. Reprinted with permission from [44].

2.2.4.6. Ring opening of indan

Although many researchers studied catalytic ring opening using MCP as the model compound, its structure is not close enough to the real feed molecules. A multi-ring compound model, indan (benzocyclopentane), has structure and properties that are closer to the petroleum real feed than the commonly used MCP. Indan consists of a C_5 ring fused to a benzene ring, and is a probable reaction intermediate of heavy oil on ring opening catalysis [44, 59]. Boutonnet et al. have studied the RO of indan over Pt-Ir bimetallic catalysts supported on seven different materials, and found that 2 wt.% Pt_5Ir_{95}/CeO_2 is the best catalyst for selective RO of indan [3]. However, no size or structure control was achieved, as the catalysts were prepared via traditional impregnation of the supports with metal precursors followed by reduction.

RO mechanism of indan over Pt-Ir catalysts at 325 ^{o}C and atmospheric pressure is presented in Figure 2.24. The desired ring opening products are *2*-ethyltoluene and *n*-propylbenzene, where the naphthenic ring has been cleaved only once, leaving the molecular weight unchanged. However, due to the consecutive dealkylation, further stripping of hydrocarbon fragments occurs irrevocably and products such as *o*-xylene, ethylbenzene, toluene, benzene, and

lights are formed [3]. Only the α-ring opening results in cetane number improvement (eliminating branches as described previously). α-ring opening produces *n*-propylbenzene, which may crack to ethylbenzene, benzene, and toluene with light products. β-ring opening produces *2*-ethyltoluene or *o*-xylene with lights. β-ring opening results in octane number (ON) improvement for gasoline. Octane number measures the resistance from petro to engine knocking. Iso-octane is a highly branched isoparaffin molecule, which has an ON of 100, so the desired product for ON improvement should have more branches (*2*-ethyltoluene). The bond dissociation energies (BDE) explain why β-ring opening is preferred over α-ring opening (BDE of C_6H_5-C_2H_5 is 99 kcal/mol, while BDE of $C_6H_5CH_2$-CH_2 is only 73 kcal/mol), therefore, thermodynamics works against our purpose to improve the cetane numbers with less branching products [9].

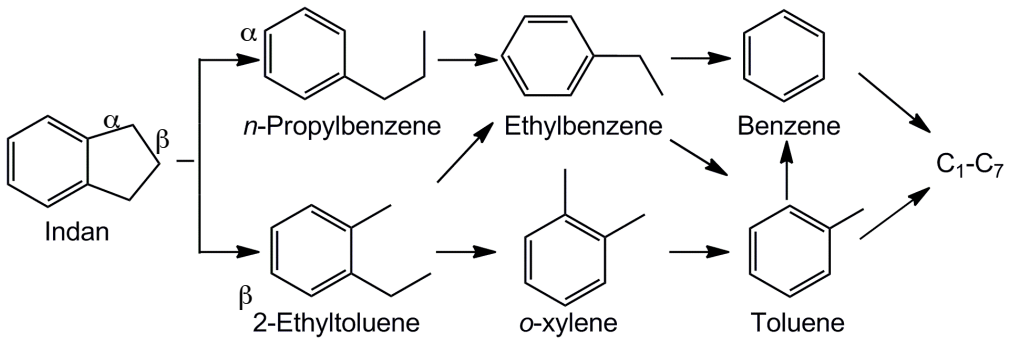

Figure 2.24. Ring opening of indan at α and β positions and further cracking products. Reprinted with permission from [3].

Boutonnet et al. have reported the activity and selectivity of the ring opening of indan at both atmospheric pressure and high pressure (40 bar) over a 2 wt.% $Pt_{25}Ir_{75}$/boehmite catalyst [59]. At atmospheric pressure, Ir and Pt-Ir catalysts showed superior activities, while the activity of Pt was very low (1% conversion after 4.5 hrs). As time on stream (TOS) increased, RO of indan generated mainly

2-ethyltoluene (61-76%). *n*-propylbenzene was formed in smaller quantities (7-10%). At high pressure, hydrogenation of indan into hexahydroindan was favored. At higher temperature, undesired cracking products increased significantly.

2.3. Concluding remarks from the literature review

The cetane number of fuels can be increased using bimetallic catalysts; however, up to now, there is no data on the use of bimetallic nanoparticles with controlled structure and size for ring opening. As has been shown in the past decade, the nanoparticle precise control can bring about tremendous improvements in catalytic activity and selectivity. Nanoparticles with different sizes have different surface atom distribution. If the catalytic activity is enhanced over some specific atoms (e.g., surface or defect atoms), then a monodispersed catalyst will lead to the overall improved activity as compared to a polydispersed catalyst. Recent advances in nanoparticle synthesis motivated us to prepare bimetallic nanoparticles with different structures and compositions and study their catalytic performance in the selective ring opening of indan. The study will allow verifying the hypothesis of the approach success and find the most optimal catalytic system to improve cetane number of fuels.

3. Materials and Methods

3.1. Materials

For the catalyst preparation: palladium(II) chloride solution ($PdCl_2$, 5% w/v, Acros), ruthenium(III) nitrosylnitrate ($Ru(NO)(NO_3)_3$, Alfa Aesar), ruthenium(III) chloride hydrate ($RuCl_3$, Sigma-Aldrich), hydrogen hexachloroiridate(IV) hydrate (H_2IrCl_6, 99.98%, Sigma-Aldrich), poly-(vinylpyrrolidone) (PVP, MW: 10K, 29K, and 40K, Sigma-Aldrich), ethylene glycol (EG, 99.8%, Sigma-Aldrich), gamma aluminum oxide (γ-Al_2O_3, 150 mesh 58Å, Sigma-Aldrich, reagent alcohol (ethanol, 95 vol.%, Fisher Scientific), acetone (99.7%, Fisher Scientific), and *1*-propanol (min 99.5%, Caledon) were used as received. Nitrogen and hydrogen of ultra high purity 5.0 (99.999%) were purchased from Praxair. MilliQ water was used throughout the experiments.

For the ring opening reaction: indan was purchased from Aldrich and distilled once for purification; indan assay was estimated as 96.8% by gas chromatography (GC). Hydrogen and Argon of ultra high purity 5.0 were purchased from Praxair.

3.2. Preparation of catalysts

The first objective of this study is catalyst preparation. PVP-stabilized monometallic nanoparticles were synthesized in ethanol, *1*-propanol, or polyols that serve both as solvent and reducing agent. Based on the synthesis methods of monometallic nanocatalysts, bimetallic nanoparticles with controlled sizes, compositions, and structures were then synthesized.

3.2.1. Synthesis of PVP-stabilized Pd nanoparticles and Pd/γ-Al_2O_3 catalysts

PVP-stabilized Pd nanoparticles were synthesized by Miyake's one-step ethanol reducing method and stepwise growth method [11, 60]. Palladium precursors were reduced to Pd^0 according to Equation (3.1):

$$M^{n+} + CH_3CH_2OH \rightarrow M^0 + CH_3CHO \tag{3.1}$$

3.2.1.1. One-step synthesis method

Pd nanoparticle size control in a one-step was achieved by changing PVP-to-metal molar ratio or reducing agent concentration. 50 mL of 2.0 mM $PdCl_2$ aqueous solution was prepared by diluting $PdCl_2$ solution (5% w/v) with milliQ water (resistivity 18.2 MΩ·cm). A mixture of 50 mL 2.0 mM $PdCl_2$ solution, 167 mL ethanol/water solution, and designated amount of poly-(vinylpyrrolidone) PVP (MW 40,000) was stirred and refluxed in a 250 mL 3-neck round bottom flask for 3 hours under air, to synthesize PVP-stabilized Pd nanoparticles (see Table 3.1 for experimental details). Transparent dark-brown colloidal dispersions of Pd metal nanoparticles were obtained without any precipitate. In order to control the sizes of PVP-stabilized Pd nanoparticles, the concentrations of ethanol used as reducing agent were 16 vol.%, 40 vol.%, and 70 vol.%; and the molar ratios of PVP/Pd were 1/1, 10/1, and 40/1 (Table 3.1) [11]. The solvent and unreduced Pd salts were removed by either acetone wash (Pd1 and Pd2) or dialysis (Pd3 and Pd4). During dialysis, Pd colloidal solutions in 28 μm thickness dialysis tubing (3,500 MW cut-off, regenerated cellulose tubular membrane) were dialyzed against 3,000 mL milliQ water for 24 hours to remove solvent and unreduced Pd salts. Syntheses of Pd3 and Pd4 nanoparticles were reproduced twice.

Table 3.1. Synthesis conditions for Pd nanoparticles using one-step synthesis method (as described in [11]).

Sample designation	Expected sizes [11] nm	[EtOH] vol.%	PVP/Pd mol./mol.
Pd1	2.2	40	10/1
Pd2	3.4	16	1/1
Pd3	4.0	70	40/1
Pd4	4.9	70	10/1

3.2.1.2. Stepwise growth synthesis method

In general, it is considered that it is difficult to prepare Pd nanoparticles larger than 3 nm in a one-step growth in the presence of PVP [11]. Therefore, Miyake's stepwise growth method was used to synthesize Pd nanoparticles with sizes greater than 3 nm [11, 60]. In the first step (PdS1, Table 3.2), Pd nanoparticles were prepared by one-step synthesis method. 50 mL 2.0 mM $PdCl_2$ aqueous solution, 167 mL ethanol/water solution ([EtOH] = 40 vol.%), and 0.222 g PVP (MW = 40,000; PVP/Pd = 20/1) were mixed, stirred, and refluxed for 3 hours under air. In the second step (PdS2), the growth of Pd atoms on the seed nanoparticles was carried out by mixing 50 mL of 0.6 mM PVP-Pd dispersion from step one with 50 mL of 0.6 mM $PdCl_2$ in ethanol/water ([EtOH] = 40 vol.%). The mixture was then stirred and refluxed for 3 hours under air. The third and fourth steps (PdS3 and PdS4) were performed similar to the second step with nanoparticles from previous steps as seeds (see Table 3.2 for experiment details) [11, 60]. Transparent dark-brown colloidal solutions of Pd metal nanoparticles were obtained without any precipitates. Syntheses of PdS1-PdS4 were reproduced twice.

Table 3.2. Synthesis conditions for Pd nanoparticles using stepwise growth method [60].

Sample designation	Expected sizes [60] nm	PVP/Pd mol./mol.
PdS1	3.0 ± 0.6	20/1
PdS2	3.9 ± 0.7	10/1
PdS3	5.2 ± 0.8	5/1
PdS4	6.6 ± 0.9	2.5/1

3.2.1.3. Nanoparticle deposition

Synthesized Pd nanoparticles were deposited on support for the future use in catalytic reactions. Nanocatalyst support, γ-Al_2O_3 (target loading is 0.3 wt.%), was dried in oven at 120 ^oC for 12 hours. The support characteristics are: activated, weakly acidic γ-Al_2O_3, 150 mesh, 5.8 nm pore size, surface area of 155 m^2/g. PVP-stabilized Pd1, Pd2, and PdS1-PdS4 colloids were precipitated with acetone, and deposited on γ-Al_2O_3 by wet impregnation. PVP-stabilized Pd3 and Pd4 colloids were deposited by incipient wetness impregnation. Finally, all PVP-stabilized Pd/γ-Al_2O_3 catalysts were dried in a fumehood.

3.2.2. Synthesis of PVP-stabilized Ru nanoparticles and Ru/γ-Al_2O_3 catalysts

PVP-stabilized Ru nanoparticles were synthesized by Li's one-step and seeding growth methods in ethylene glycol [60], as well as Miyake's stepwise growth method [11] for the synthesis of Pd nanoparticles.

3.2.2.1. $Ru(NO)(NO_3)_3$ precursor

Size control of Ru nanoparticles in a one-step reaction was achieved by varying the mode of reactants addition or reduction temperature. However, based on the size control of Pd nanoparticles, stepwise growth method is more effective than one-step method to get bigger nanoparticles (> 3 nm) [11].

One-step synthesis method. Li's one-step synthesis methods were used to synthesize PVP-stabilized Ru nanoparticles [62]. The size of PVP-stabilized Ru nanoparticles was controlled by varying the mode of addition of reactants, reaction temperature, and reduction time (see Table 3.3 for experiment details). In mode A, $Ru(NO)(NO_3)_3$ and PVP(MW 10,000) were dissolved in 100 mL ethylene glycol (EG) in a 250 mL 3-neck flask under stirring and refluxing. In mode B, 100 mL PVP-Ru^{3+}-EG solution was prepared at room temperature. For both modes, the concentration of Ru^{3+} was 1.12 mM, and molar ratio of PVP/Ru was 10/1. For Ru4, 100 mL PVP-Ru^{3+}-EG solution was then added into 10 mL EG dropwise (1 mL/min) under stirring and refluxing. After the reaction, transparent dark-brown colloidal dispersions of Ru metal nanoparticles were obtained without any precipitates. After synthesis reactions, PVP-stabilized Ru1-Ru4 colloidal solutions were dialyzed against 3,000 mL milliQ water in 28 μm dialysis tube (3,500 MW cut-off) 2 times (48 hours each time) to remove EG and unreduced Ru salts. Syntheses of Ru1 and Ru4 were reproduced at least twice.

Table 3.3. Synthesis conditions for Ru nanoparticles [62].

Sample designation	Expected size, nm	Mode of reactants addition	Reaction temperature, ^{o}C	Reduction time, h
Ru1	2.6 ± 0.3	B	25 – 200	3.6
Ru2	3.7 ± 0.7	A	160	3
Ru3	4.2 ± 0.6	B	25 – 160	3.6
Ru4	N/A	B	140	>12

Li's seeding growth synthesis method. In order to obtain large size of Ru nanoparticles, RuS1 and RuS2 catalysts were prepared using Li's seeding growth method [62]. During the seeds preparation (RuS1, expected size of 2.6 ± 0.3 nm), PVP-stabilized Ru nanoparticles were prepared as seeds using the one-step synthesis method for Ru1. In the growth step (RuS2, expected size of 5.4 ± 0.7 nm), a mixture of 2.5 mL of 2.6 nm PVP-Ru seeds, 25 mL 1.12 mM Ru^{3+}-EG solution (prepared at room temperature), and excess amount of L-ascorbic acid (0.1 M, 3 mL) was stirred and refluxed at 160 ^{o}C under air for 3 hours. Transparent dark-brown colloidal solutions of Ru metal nanoparticles were obtained without any precipitates.

Miyake's stepwise growth synthesis method. Since stepwise growth method is more effective to synthesize large size Pd nanoparticles, RuS3 (expected size of 6.6 ± 0.9 nm) was then synthesized by Miyake's stepwise growth method for Pd [11, 60]. In the first step, Ru nanoparticles were prepared by one-step synthesis method of PdS1 with some changes. A mixture of 50 mL 2.0 mM $Ru(NO)(NO_3)_3$ solution, 117 mL EG, and 0.222 g PVP (MW 40,000) (PVP/Ru = 20/1) was stirred and refluxed for 3 hours under air. The second, third, and forth (RuS3) growths of PVP-Ru nanoparticles were carried out by the same growth methods as those for PdS2, PdS3, and PdS4, respectively, but using $Ru(NO)(NO_3)_3$

precursors instead. Transparent dark-brown colloidal solutions of Ru metal nanoparticles were obtained without any precipitates. The synthesis of RuS3 was reproduced twice.

3.2.2.2. $RuCl_3$ precursor

Different metal precursors could also affect the size or structure of nanoparticles, as PVP may have different degrees of interactions with metal ions; so Ru nanoparticles were also synthesized from the reduction of ruthenium(III) chloride hydrate. $RuCl_3$ and PVP (MW 40,000) were mixed with 100 mL EG in a 250 mL 3-neck flask. The concentration of $RuCl_3$ was 1.12 mM; and the molar ratio of PVP/Ru was 10/1. The mixture was then stirred and refluxed under air for 3 hours to synthesize PVP-Ru nanoparticles. Transparent dark-brown homogeneous colloidal solutions of Ru metal nanoparticles were obtained without any precipitates. In order to control the sizes of PVP-Ru nanoparticles, synthesis reactions were carried out at two different temperatures, 160 ^{o}C (Ru5, expected size of 7.4 ± 2.2 nm) and 200 ^{o}C (Ru6, expected size of 5.4 ± 1.2 nm) [63]. After reaction, PVP-stabilized Ru colloidal solutions were dialyzed against 3,000 mL milliQ water in 28 μm dialysis tubing (3,500 MW cut-off) twice (48 hours each time) to remove EG and unreduced $RuCl_3$ precursor.

3.2.2.3. Nanoparticle deposition

Synthesized Ru nanoparticles were deposited on support for the future use in catalytic reactions. Nanocatalyst support, γ-Al_2O_3 (target Ru loading is 0.3 wt.%), was dried in oven at 120 ^{o}C for more than 12 hours. PVP-stabilized Ru1 - Ru4 nanoparticles were deposited on γ-Al_2O_3 by incipient impregnation. PVP-stabilized RuS1 - RuS3 colloids were precipitated with acetone, and deposited on

γ-Al_2O_3 by wet impregnation. Finally, all PVP-Ru/γ-Al_2O_3 catalysts were dried in a fumehood.

3.2.3. Synthesis of PVP-stabilized Ir nanoparticles and Ir/γ-Al_2O_3 catalysts

3.2.3.1. Stepwise growth synthesis method

There is no previous study on the size control of monometallic Ir nanoparticles, so Miyake's stepwise growth method for the synthesis of PVP-stabilized Pd nanoparticles was applied to synthesize PVP-stabilized Ir nanoparticles [11, 60]. During the synthesis of Ir seeds, Ir precursors were reduced by ethanol (Equation 3.1) or *1*-propanol (similarly to the reduction by ethanol).

In the first step, PVP-stabilized Ir seeds were prepared by a one-step alcohol/water reduction method [17, 64]. During the ***1-propanol/water reduction***, 50 mL aqueous solution containing 0.1 mmol H_2IrCl_6 and 0.116 g PVP (MW 40,000) (PVP/Pd = 10/1) were mixed with 150 mL *1*-propanol/water solution ([1-PrOH] = 90 vol.%) in a 250 mL 3-neck round bottom flask. In the ***ethanol/water reduction***, 50 mL 2.0 mM H_2IrCl_6 solution, 167 mL ethanol/water solution ([EtOH] = 40 vol.%), and 0.222 g PVP (MW 40,000) were mixed in a 250 mL 3-neck round bottom flask. For both cases, the mixtures were stirred and refluxed under air for 3 hours. All further growth steps were carried out in ethanol/water.

In the second step, the growth of PVP-stabilized Ir nanoparticles was carried out by mixing 50 mL of 0.6 mM PVP-Ir dispersions from step one and 50 mL of 0.6 mM H_2IrCl_6 in ethanol/water ([EtOH] = 40 vol.%). The mixture was then stirred and refluxed for 3 hours under air. The third and fourth steps were performed the same way as second step with nanoparticles from previous steps as

seeds (see Table 3.4 for experiment details) [11, 60]. Transparent dark-brown colloidal solutions of Ir metal nanoparticles were obtained without any precipitates. Synthesis of IrS11 using *1*-propanol reduction method was repeated.

Table 3.4. Synthesis conditions for Ir nanoparticles [60].

Sample [a] designation	PVP/Ir [a] mol./mol.	Sample [b] designation	PVP/Ir [b] mol./mol.
IrS11	10/1	IrS21	20/1
IrS12	5/1	IrS22	10/1
IrS13	2.5/1	IrS23	5/1
IrS14	1.75/1	IrS24	2.5/1

[a] in the first step, Ir precursors were reduced by *1*-propanol/water.
[b] in the first step, Ir precursors were reduced by ethanol/water.

3.2.3.2. Nanoparticle deposition

Synthesized Ir nanoparticles were deposited on support for the future use in catalytic reactions. Nanocatalyst support, γ-Al_2O_3 (target loading is 0.3 wt.%), was dried in oven at 120 ^oC for more than 12 hours. PVP-stabilized Ir colloids were precipitated with acetone, and deposited on γ-Al_2O_3 by wet impregnation. Finally, all Ir/γ-Al_2O_3 catalysts were dried in a fumehood.

3.2.4. Synthesis of PVP-stabilized core-shell structure bimetallic nanoparticles and corresponding supported catalysts

Ir is known as the most active and selective catalyst in RO reactions; Ru containing catalyst may lead to higher sulfur tolerance, since RuS_2 is the most active catalyst in hydrodesulfurization [65]. Therefore, the core-shell

nanoparticles with Pd core and Ir (or Ru) shell structure were synthesized. There is a great hope that Ir will provide high activity, and Ru will improve S-tolerance in the RO of indan to be studied later. Pd atoms in the core were expected to have strong electronic effects on the shell Ir (or Ru) atoms, and so to affect the chemisorption strength and mode during the catalytic reactions.

As previously described in literature review section, the most effective method to obtain core-shell structure is successive reduction, so Toshima's hydrogen-sacrificial method for Pd-Pt bimetallic colloids preparation was used to synthesize Pd(c)Ir(s) and Pd(c)Ru(s) bimetallic nanoparticles [39]. Hydrogen atoms adsorbed on the pre-synthesized metal nanoparticle surfaces have a strong reducing ability, implying a low redox potential; thus, if a metal nanoparticle, which is able to dissociate hydrogen, is treated with hydrogen and then with a precursor of a second metal, the latter forms a shell around the former nanoparticle [39, 66]. The molar ratio of the core/shell was 1/1 in this study.

In the presented study, the core-shell structure was assumed due to the synthesis method and needs to be confirmed.

3.2.4.1. Metal core preparation

The first step in the successive reduction is metal core preparation, which is a one-step reduction reaction based on the synthesis of monometallic metal nanoparticles, i.e., 0.1 mmol of Pd core was prepared as for Pd1 nanoparticles (see section 3.2.1).

3.2.4.2. Core-Shell structure preparation

The next step is reduction of the second metal ions on the pre-synthesized core nanoparticles and formation of shell. The 250 mL three-neck flask containing core nanoparticles (Pd(c)) was equipped with a dropping funnel containing 50 mL 0.1 mmol shell metal precursor (M(s)) aqueous solution. Molar ratio of shell metal-to-core metal was 1/1. Pd core nanoparticle colloidal solution in the reaction flask was treated with hydrogen for 2 hours. Shell precursors in the dropping funnel were bubbled by nitrogen for 5 minutes to replace air. The aqueous solution of shell metal precursor was then added into the reaction system drop by drop for about 1 hour, and the reaction was continued for at least 5 hours under hydrogen environment. Transparent dark-brown homogeneous colloidal solutions of bimetallic nanoparticles were obtained without any precipitates. Solvent and unreduced metal salts were removed by acetone wash. Synthesis of Pd(c)Ir(s) was reproduced at least twice.

3.2.4.3. Nanoparticle deposition

Synthesized M(c)M(s) nanoparticles were deposited on support for the future use in catalytic reactions. Nanocatalyst support, γ-Al_2O_3 (target loading is 0.3 wt.%), was dried in oven at 120 ^{o}C for more than 12 hours. PVP-stabilized M(c)M(s) colloids were precipitated with acetone, and deposited on γ-Al_2O_3 by wet impregnation. Finally, PVP-stabilized M(c)M(s)/γ-Al_2O_3 catalysts were dried in a fumehood.

3.2.5. Synthesis of PVP-stabilized alloy structure bimetallic nanoparticles and corresponding supported catalysts

One of the objectives of this study is to find the correlations between nanoparticle compositions and its catalytic activity and selectivity, so bimetallic nanoparticles with varying metal ratios were synthesized. Based on the literature reviews, Ru containing catalyst system can improve S-resistance; and Ir containing catalyst should result in higher activities. Although previous studies in RO reactions did not report Pd as the most active or stable catalyst, it has similar hydrogenation properties as Pt [67], and RO of indan requires dissociative hydrogen adsorption as well. However, the optimal combination of two metals is not know from the literature and needs to be found.

Therefore, Pd-Ir, Ir-Ru, and Pd-Ru were synthesized using the synthesis methods for monometallic Pd and Ru nanoparticles. For each alloy structure, three different metal molar ratios were synthesized: 3/1, 1/1, and 1/3; for each molar ratio, two different sizes were synthesized.

In the presented study, the mixed alloy structure was assumed due to the synthesis method and needs to be confirmed.

3.2.5.1. Pd-Ir colloids

Since there is no previous study reported on the size control of Ir nanoparticles, and both Pd and Ir precursors could be reduced by ethanol based on the previous synthesis of monometallic nanoparticles, Toshima's ethanol reduction method to synthesize Pd nanoparticles was used to synthesize Pd-Ir bimetallic nanoparticles [11]. Table 3.5 shows synthesis conditions for two different sizes of Pd3Ir1 (Pd/Ir molar ratio = 3/1). Same synthesis conditions were

applied for Pd1Ir1 (Pd/Ir molar ratio = 1/1) and Pd1Ir3 (Pd/Ir molar ratio = 1/3). After reaction, transparent dark-brown homogeneous colloidal solutions of Pd-Ir bimetallic nanoparticles were obtained without any precipitates. Solvent and unreduced metal salts were removed by dialysis (24 hours). Synthesis of Pd1Ir3_2 was reproduced twice.

3.2.5.2. Ir-Ru colloids

Li's one-step ethylene glycol reduction method for Ru nanoparticles was used to synthesize Ir-Ru bimetallic nanoparticles [62]. For example, synthesis methods for Ru1 and Ru3 (section 3.2.2) were used to synthesize Ir3Ru1_1 and Ir3Ru1_2, respectively. The same approach was applied for Ir1Ru1 (Ir/Ru molar ratio = 1/1) and Ir1Ru3 (Ir/Ru molar ratio = 1/3). After reaction, transparent dark-brown homogeneous colloidal solutions of Pd-Ru nanoparticles were obtained without any precipitate. Solvent and unreduced metal salts were removed by dialysis twice (48 hours). Synthesis of Ir1Ru1_1 was reproduced twice.

3.2.5.3. Pd-Ru colloids

Pd ions are more easily reduced to metal atoms than Ru ions (due to redox potential), so Li's ethylene glycol reduction method for Ru nanoparticles was used to synthesize Pd-Ru bimetallic nanoparticles [62]. For example, preparation methods for Ru1 and Ru3 (section 3.2.2) were used to synthesize Pd3Ru1_1 and Pd3Ru1_2, respectively. The same approach was applied for Pd1Ru1 (Pd/Ru molar ratio = 1/1) and Pd1Ru3 (Pd/Ru molar ratio = 1/3). After reaction, transparent dark-brown homogeneous colloidal solutions of Pd-Ru nanoparticles were obtained without any precipitates. Solvent and unreduced metal salts were removed by dialysis twice (48 hours).

Table 3.5. Synthesis conditions for Pd-Ir nanoparticles (Pd/Ir molar ratio = 3/1) [11].

Sample designation	Expected sizes nm	[EtOH] vol.%	PVP/Pd mol./mol.
Pd3Ir1_1	1.7	40	40/1
Pd3Ir1_2	2.2	40	10/1

3.2.5.4. Nanoparticle deposition

Synthesized nanoparticles with presumably alloy structures were deposited on support for the future use in catalytic reactions. Nanocatalyst support, γ-Al_2O_3 (target loading is 0.3 wt.%), was dried in oven at 120 ^{o}C for more than 12 hours. PVP-stabilized colloids were deposited by incipient impregnation. Finally, catalysts were dried in a fumehood.

3.3. Colloids and catalyst characterization techniques

3.3.1. Transmission electron microscopy (TEM)

Transmission electron microscopy allows analysis of the size and shape of nanoparticles. As-prepared metal nanoparticles were characterized by TEM using a JEOL 2100 transmission electron microscope operating at 200 kV. Samples for TEM were prepared by placing a drop of the colloidal dispersion of metal nanoparticles onto a carbon-coated copper grid, followed by evaporating the solvent at room temperature. Most of the samples were prepared immediately after nanoparticle synthesis, unless indicated otherwise. Diameters of over 200 particles were determined using ImageJ software. The mean diameter (d) and standard deviation (σ) were determined by Equations (3.2), where i represents

each nanoparticle being analyzed, and n is the total number of nanoparticles that are analyzed:

$$d = \frac{\sum d_i}{n}, \sigma = \sqrt{\frac{1}{n}\sum_{i=1}^{n}\left(d_i - d\right)^2} \tag{3.2}$$

3.3.2. UV-visible spectroscopy

Formation of metal nanoparticles in their colloidal dispersions was confirmed with a Varian Cary 50 Scan UV-vis spectrometer using a quartz cell (1 cm). Teranishi and Miyake have confirmed the formation of Pd nanoparticles via UV-vis spectrometer. The absorption from the ultraviolet to visible region increases, suggesting that the band structure of the Pd nanoparticles is formed [11].

3.3.3. Atomic absorption spectroscopy (AAS)

Atomic absorption spectroscopy is a quantitative elemental analysis, and determines the metal loading of the supported nanocatalysts. The actual loadings of Pd and Ru nanoparticles on γ-Al_2O_3 were determined using a SpectrAA 220FS Atomic Absorption Spectrometer (Varian). Samples for AAS were prepared by dissolving certain amount of catalysts in hot concentrated nitric acid (or aqua regia when necessary) followed by filtration through a Whatman filter paper and then quantitative dilution. AAS requires samples in solution and only Pd and Ru catalysts are soluble in nitric acid (or aqua regia), so only these two metals are analyzed by AAS.

3.3.4. Neutron activation analysis (NAA)

Since it is not possible to dissolve Ir, even in aqua regia, monometallic Ir and all the bimetallic catalysts were analyzed by NAA. The advantage of NAA is that supported nanoparticles do not need to be dissolved, and the method does not suffer from matrix problems. The actual loadings of Ir, Pd-Ir, Ir-Ru, and Pd-Ru nanoparticles on γ-Al_2O_3 were determined by NAA at either the Slowpoke facilities at University of Alberta or the Becquerel Laboratories Inc. in Mississauga, Ontario. Samples were irradiated for 110 s in the Cd shielded, epi-thermal site of the reactor core (McMaster University). They were counted for 30 min each on an Aptec CS11-A31C gamma detector, approximately 12 h after irradiation.

3.3.5. X-ray photoelectron spectroscopy (XPS)

X-ray photoelectron spectroscopy (XPS) is a surface-sensitive analysis (up to 10 nm) that gives both quantitative and qualitative results on the analysed element. XPS was performed using a Kratos Axis 165 X-ray photoelectron spectrometer with a Mono Al Kα source (operated at 15 mA and 14 kV). The survey spectrum and the high resolution spectrum were scanned with a pass energy of 160 eV, and of 20 eV, respectively. During the acquisition of a spectrum, charge neutralization was applied to compensate the insulating problem of the sample.

3.4. Low-pressure ring opening of indan

After the catalysts preparation and characterization, the second part of this study is catalytic ring opening of indan. In the laboratory investigation, the

reaction system was kept simple to allow fast catalyst screening. Selective ring opening was studied at low pressure, as low pressure promotes the RO route vs. the hydrogenation route at high pressures (40 bars); and indan was chosen as the model compound, because it is closer to the real industrial feed as compared to commonly used methylcyclopentane [3].

3.4.1. Catalysts pre-treatment

Prior to the catalytic reactions, polymers must be removed, as PVP could block the active sites of catalyst. In order to remove PVP, PVP-stabilized mono- and bimetallic Pd, Ru, and Ir catalysts were calcined at 200 ^{o}C in an oven under air for 1 hour. Catalysts were then reduced at 359 ^{o}C for 1 hr under hydrogen flow (80 mL/min) by increasing reactor internal temperature from room temperature to 359 ^{o}C at a rate of 5 ^{o}C/min, and then holding for 1 hour. This oxidation-hydrogenation cycle is known to remove PVP from metal nanoparticles at lower temperature than free PVP decomposition according to Somorjai's study. In their study, catalysts were calcined in 20% O_2/He for 1 hr at 200 ^{o}C, purged with He for 0.5 hr at 200 ^{o}C, and then followed by reduction in H_2 for 1 hr at 200 ^{o}C. Somorjai et al. also confirmed that ethylene hydrogenation activity was maximized with in-situ oxidation-reduction cycle at 200 ^{o}C [68].

3.4.2. Experimental set up and conditions

Ring opening of indan was carried out in a packed bed reactor instead of a constant-volume batch reactor in a liquid phase, as three-phase reactions are more susceptible to mass transfer limitations (thus, intrinsic catalytic behavior can not be estimated) and forming lights will lead to a pressure increase. A continuous

fixed bed catalytic reactor, which is a 16" long stainless steel tube with an inner diameter of 1/2', was packed with the catalyst corresponding to 1.2 mg active metal(s) (diluted with 2 g 150 mesh SiC) and encircled by a furnace. A reactor setup schematic is shown in Figure 3.1. The reactant, indan, was fed into the catalytic system by bubbling 50 mL/min H_2 through indan at a constant temperature bath at 10 ^oC. Indan flow rate for each reaction was determined from GC areas; the GC was calibrated using a HPLC pump with known indan flow rate. A high H_2-to-indan molar ratio was used to avoid coke formation. 99.999% pure Ar and H_2 flows were controlled by calibrated mass flow controllers (Sierra Instruments). The catalytic reactions were carried out at an internal temperature of 336 ^oC and atmospheric pressure. The reactor up- and down- streamlines were heated to 220 ^oC to preheat reactants and avoid product condensation. The outgoing stream was analyzed on-line with a Varian 430-GC-FID every 30 minutes since reaction was started. Reaction parameter settings and GC analytical procedure are summarized in Table 3.6.

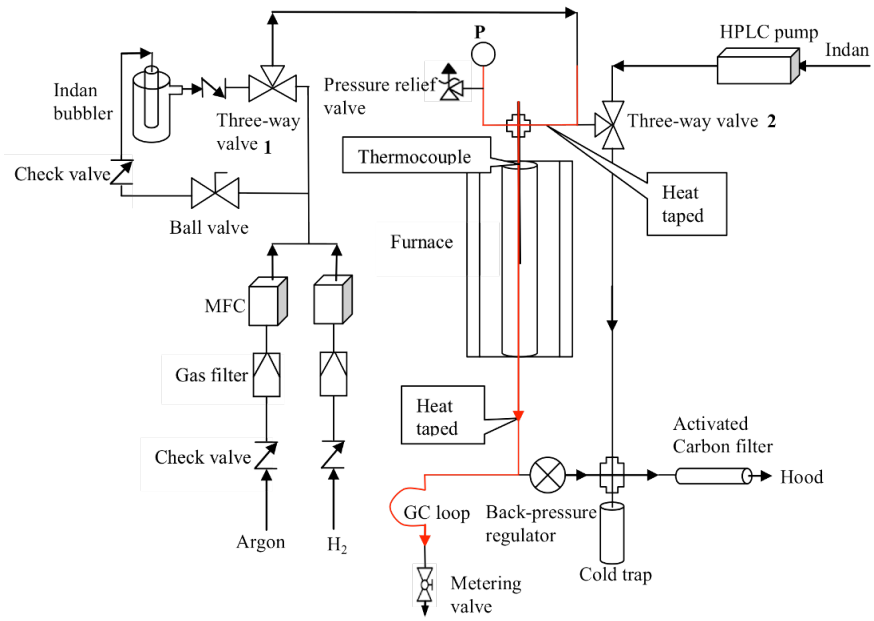

Figure 3.1. A schematic diagram of reactor setup.

Table 3.6. Experimental conditions and GC analytical procedure for catalytic low-pressure ring opening of indan.

Reaction conditions	**On-line product analysis by Varian 430-GC-FID**
Temperature: 336 ^{o}C Pressure: atmospheric H_2 flow rate (STP): 50 mL/min Indan flow rate (calibrated): (2.1– 5.1) $\times 10^{-5}$ g/min H_2/indan molar ratio: 4800 – 11600	He flow rate: 25 mL/min Split ratio: 1 Capillary column: WCOT FUSED SILICA 50 m × 0.32 mm × 1.2 μm COATING CP-SIL 5CB Oven temperature description: Stabilizing 2.5 min at 40 ^{o}C, then 30 ^{o}C/min ramp to 110 ^{o}C and hold for 20 min. FID and injector temperature: 280 ^{o}C

3.4.3. Reaction product identification

In the previous study on ring opening of indan over Pt-Ir catalysts, Boutonnet et al. have reported that the major ring opening products are *2*-ethyltoluene, *n*-propylbenzene, *o*-xylene, ethylbenzene, toluene and benzene [3], which was confirmed in our study. A typical chromatogram of low-pressure ring opening of indan over industrial Pt-Ir catalyst is shown in Figure 3.2. In order to identify the peaks, retention times of major ring opening products (C_6-C_9) were compared with those of the pure reference compounds. Compounds with the GC retention times less than 4.85 minutes were named as “lights”; and products other than the main products (shown in Figure 2.24) and lights were called “others”. The desired products of ring opening of indan are *2*-ethyltoluene and *n*-propylbenzene, where the naphthenic ring has been cleaved only once. From cetane number point of view, *n*-propylbenzene (eliminating branch) is more favorable of these two products. Further dealkylation, which results in toluene, benzene and lights, is

highly undesired [3, 59].

Reaction products and indan impurities were confirmed by GC-MS. GC-MS was performed with an Agilent Technologies 7890 GC coupled with 5975C MSD (single quadrupole mass spectrometry). The GC column used is a ZB-50 (Phenomenex) column, 30 m length × 25 mm i.d. × 25 μm thickness. Oven temperature was stabilized at 40 ^{o}C for 0.5 min, then increased to 110 ^{o}C at 30 ^{o}C/min to, and then increased to 280 ^{o}C at 50 ^{o}C/min.

The reactant (indan) and major products (benzene, toluene, ethylbenzene, *o*-xylene, *n*-propylbenzene, and *2*-ethyltoluene) were confirmed by chemical standards and GC-MS (Table C1, Appendix C). A list of by-products and indan impurities found by GC-MS is given in Table C2, Appendix C.

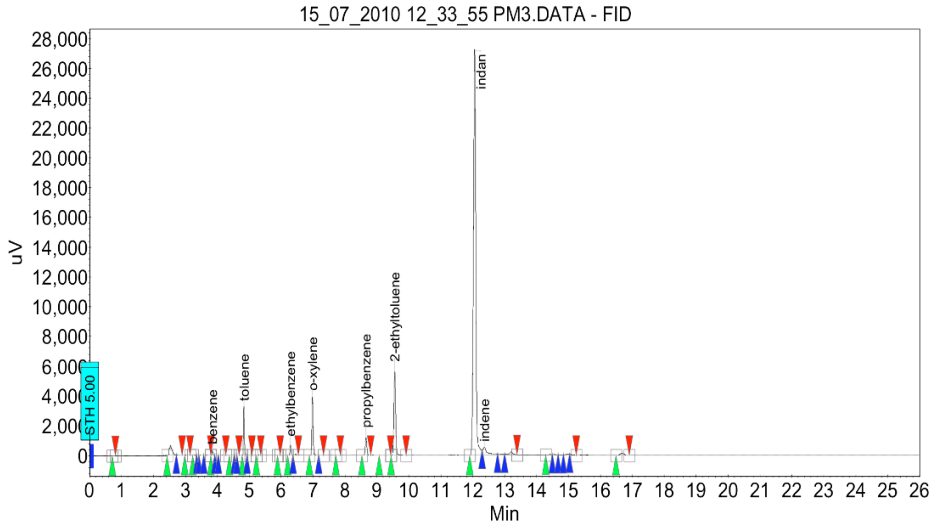

Figure 3.2. A typical chromatogram of low-pressure ring opening of indan. Apart from indan and main products indicated on the chromatogram, other peaks ("lights" and "others") also were taken into consideration for analysis.

3.4.4. Calculation of indan conversion, catalytic activity, and selectivity

In order to propose the optimal catalyst system for RO of indan, indan conversion, catalytic activity and selectivity should be calculated and compared with the industrial Pt-Ir catalyst. Indan conversion and selectivities are reported on mass basis, as FID detector is a mass-sensitive analyzer that responds to the number of carbon atoms entering per unit of time. After the steady state was achieved (at 150 min TOS), no more than 5% deviation in the mass balance was observed (typically, within 2%) as compared to the mass flow of incoming indan. Raw GC results were corrected for indan impurities and used for data analysis. Indan purified by distillation contains 0.09% of benzene, 0.15% of *n*-propylbenzene, 0.02% of *2*-ethyltoluene, 0.02% of lights, and 2.91% of others. Raw GC results from catalytic reactions were corrected for impurities, and all calculations for indan conversion and product selectivities were based on the corrected GC results. The use of internal standard (undecane was tested) was not possible due to its decomposition during ring opening reaction (undecane was cracked into shorter chains).

The indan conversion, *X*, was found as

$$X = \frac{A_T - A_{indan}}{A_T} \times 100\% \tag{4.2}$$

A_T stands for the total GC area and includes indan, indene, main reaction products (Figure 2.24), lights, others, and by-products.

The catalytic activities were found based on indan inlet flow rate, conversion, and catalyst loading in the reactor (typically, 1.2 mg of active metal(s), unless indicated otherwise).

Selectivity to product i, S_i, can be determined as,

$$S_i = \frac{A_i}{A_T - A_{indan}} \times 100\% \tag{4.3}$$

For most of the catalysts, 8 (or 6) data points were obtained at 150, 180, 210 (and 240) minutes of time on stream with a duplicate experiment (unless stated otherwise). The data are presented as average with a standard deviation (in the brackets). Within the indicated times on stream the catalysts did not show noticeable deactivation.

4. Results and discussions

4.1. Catalyst synthesis and characterization

Monometallic Pd, Ir, and Ru nanoparticles were synthesized by alcohol reduction method. The formation of synthesized nanoparticles was confirmed by UV-visible spectroscopy; synthesized mono- and bimetallic nanoparticles sizes and size distributions were determined by TEM; and metal loadings of the supported catalysts were determined by either AAS or NAA. Based on the synthesis of monometallic nanoparticles, bimetallic nanoparticles with presumably core-shell and alloy structures were synthesized by hydrogen-sacrificial technique and simultaneous reduction method, respectively. These bimetallic structures should be confirmed by EDX and EXAFS in the future.

4.1.1. Monometallic Pd/γ-Al_2O_3 catalysts

4.1.1.1. Pd nanoparticles via one-step growth

Different sizes of Pd nanoparticles were expected with one-step reaction by changing the amount of PVP or concentration of ethanol. Figure 4.1 shows TEM images and size distributions of PVP-stabilized Pd nanoparticles Pd1 - Pd4, synthesized at various molar ratios of PVP/Pd in ethanol/water under reflux for 3 hours and subjected to dialysis (or acetone wash). Teranishi and Miyake [11] concluded that both the amount of PVP added to the solution and the concentration of alcohol could affect the size of Pd nanoparticles. As PVP stabilizes the Pd nanoparticles by preventing them from aggregation, higher amount of PVP is expected to result in lower nanoparticle size [11]. The concentration of alcohol used as a reducing agent is also very important for size

control, because faster reduction of $[PdCl_4]^{2-}$ is needed to generate smaller Pd nanoparticles (as Pd nuclei formation competes with nanoparticle growth) [11]. Our results did not show much nanoparticle size change with ethanol concentration variation, e.g., the nanoparticle size increased from 2.3 to 2.8 nm, when the ethanol concentration was increased from 40 to 70%. Among the ratios studies, PVP/Pd molar ratio of 10 was large enough to effectively stabilize the nanoparticles: when the ratio was increased to 40 (Fig. 4.1 (c)), the average diameter was barely affected (2.6 nm). When the PVP amount was decreased (Pd2, Fig. 4.1 (b)), larger nanoparticles were formed (up to 10 nm), and some of them were even anisotropic (tetrahedral and multiply twinned). Similar anisotropic Pt nanoparticle formation in the presence of PVP was described recently by Somorjai [69], when the nanoparticle size exceeds 7 nm. This was ascribed to the change in the deposition selectivity of the Pd-precursors from (100) towards (111) crystals faces and breaking up of lager particles into small entities [39]. In general, it is considered that it is difficult to prepare Pd nanoparticles larger than 3 nm through one-step growth with PVP [11].

Repeated synthesis showed reproducible Pd nanoparicle size in the range of 2 - 3 nm and narrow size distribution (Fig. A2, Appendix A). Samples Pd3 and Pd4 show narrow size distribution (0.5 - 0.6 nm), which is a characteristic feature of the applied stabilization method.

The formation of Pd nanoparticles was also confirmed by UV-vis spectroscopy. During the formation of Pd nanoparticles the yellow solution containing $[PdCl_4]^{2-}$ ions turned into dark-brown and the absorption from the ultraviolet to the visible region increases (Fig. 4.2), which was ascribed to the formation of the band structure of Pd nanoparticles [11]. Thus, nearly monodispersed Pd nanoparticles with defined size distribution were successfully synthesized.

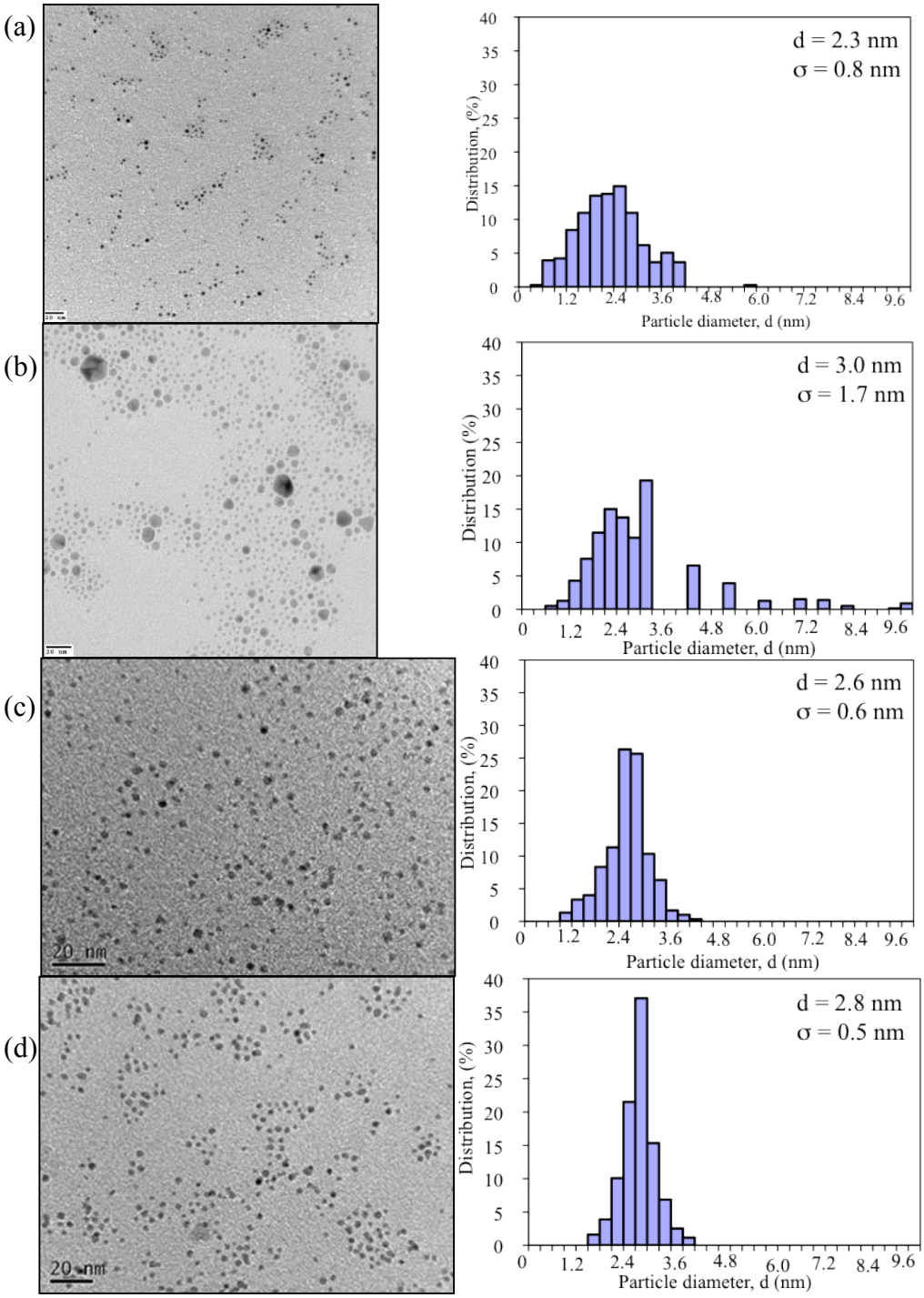

Figure 4.1. TEM photographs of Pd nanoparticles synthesized by one-step reaction (the scale bar is 20 nm) and corresponding size distribution histograms: (a) Pd1: PVP/Pd = 10; [EtOH] = 40%, (b) Pd2: PVP/Pd = 1; [EtOH] = 16%, (c) Pd3: PVP/Pd = 40; [EtOH] = 70%, and (d) Pd4: PVP/Pd = 10; [EtOH] = 70%.

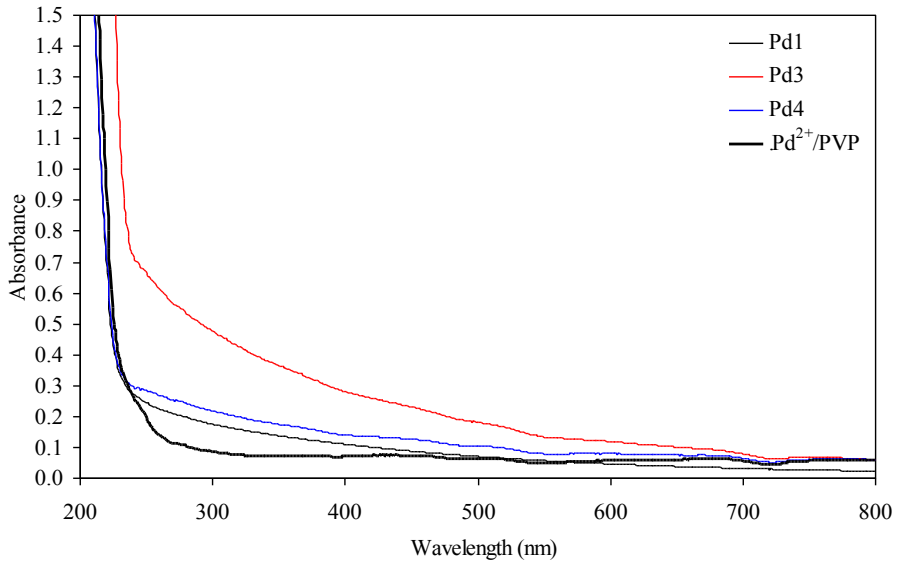

Figure 4.2. UV-vis spectroscopy of PVP-stabilized Pd nanoparticles and the precursor H_2PdCl_4.

4.1.1.2. Pd nanoparticles via stepwise growth

Since it is difficult to obtain Pd nanoparticles with average diameter greater than 3 nm, stepwise growth method was applied to synthesize bigger nanoparticles. Figure 4.3 shows TEM images and size distributions of PVP-stabilized Pd nanoparticles, PdS1 - PdS4, synthesized via stepwise growth method at varied molar ratios of PVP/Pd in ethanol/water under reflux for 3 hours. Pd nanoparticles synthesized in a one-step reaction, 2.3±0.4 nm in mean diameter, were used as seeds for stepwise growth to obtain nanoparticles larger than 3 nm.

The mean diameters of PVP-Pd nanoparticles determined from TEM images and their standard deviations are 2.3±0.4, 3.0±0.6, 3.8±1.4, and 4.4±1.6 nm for the first, second, third, and fourth stepwise growth reactions, respectively. Our results show clearly particle size increase with increasing growth steps, indicating that the nanoparticles from previous step served as nuclei for larger particles.

Similar TEM results for Pd nanoparticles synthesized by stepwise reactions were reported by Teranishi and Miyake [11]. The diameter of nanoparticles, *d*, synthesized by stepwise growth method can be calculated by Equation 4.1 [11, 60]:

$$d = d_0 \sqrt[3]{\frac{n_i + n_m}{n_m}} \tag{4.1}$$

Where d_0 is particle diameter in the starting solution; n_i and n_m are quantity of the ionic and metallic Pd, respectively. If complete reduction of Pd precursors is assumed, the mean diameters of PVP-Pd nanoparticles calculated from Equation 4.1 are 2.3, 2.9, 3.7, and 4.7 nm for the first, second, third, and fourth stepwise growth reactions, respectively. The calculated results are in good agreement with the experimental ones, with only slightly mean diameter difference.

Samples PdS1 and PdS2 show narrow size distributions (0.4 - 0.6 nm) with monodispersed Pd nanoparticles, which is a characteristic feature of the applied stabilization method. Samples PdS3 and PdS4 show relatively wide nanoparticle size distributions. As during growth only fresh Pd precursors were added, but not additional PVP, the polymer/Pd molar ratio decreased, thus larger nanoparticles were formed (up to 10 nm) and some of them were even anisotropic (PdS3 and PdS4, Fig. 4.3 (c) and (d)). The particle size distribution increased with increasing size growth, indicating that the size distribution of Pd nanoparticles prepared in the one-step reaction greatly influenced that prepared in the stepwise growth reaction [60].

Thus Pd nanoparticles of 2.3 - 4.4 nm mean diameters with well defined size distributions were successfully synthesized. Repeated synthesis showed reproducible Pd nanoparticle sizes in the range 2.3 - 4.2 nm and narrow size distributions (Figure A1, Appendix A)

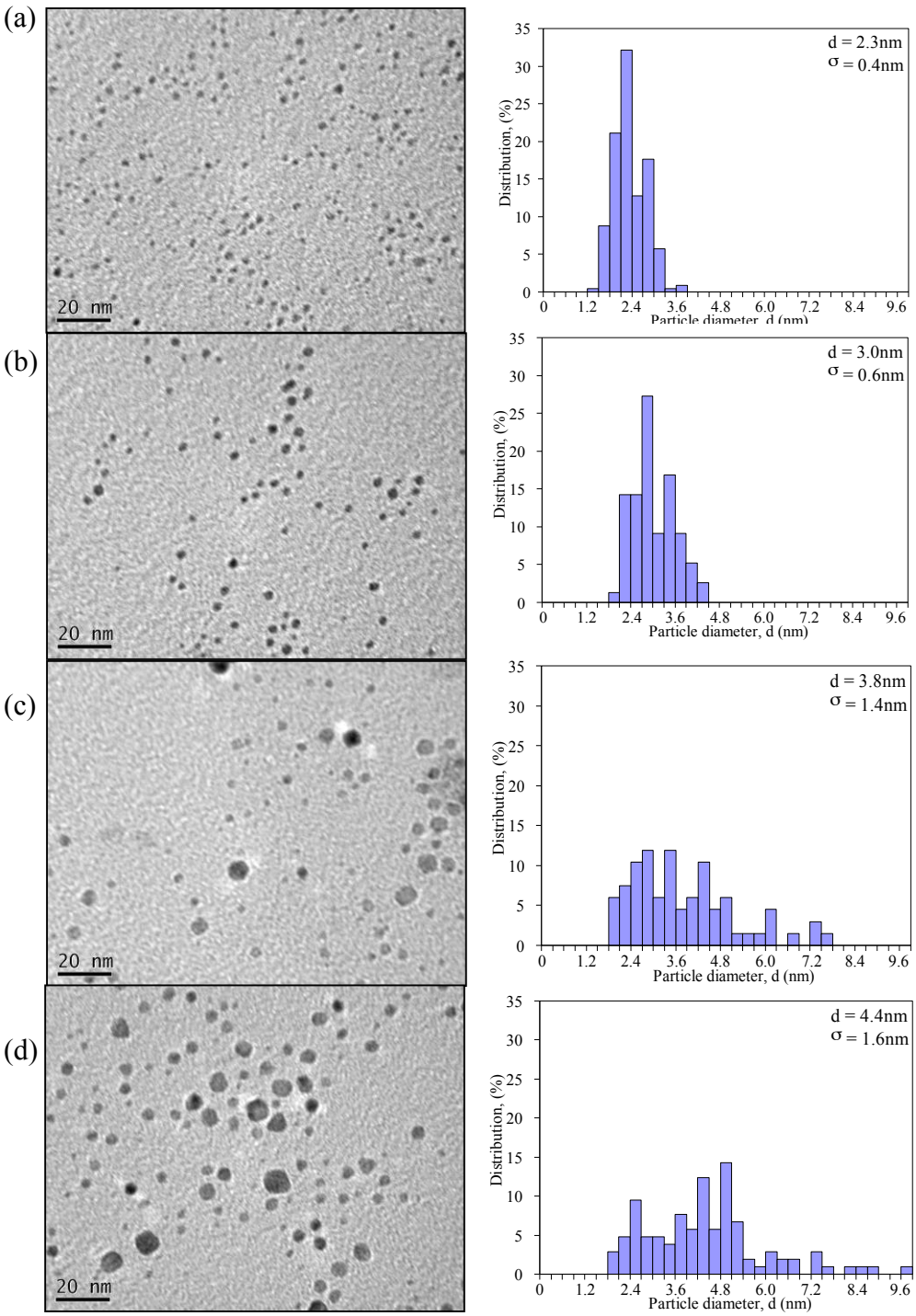

Figure 4.3. TEM photographs of Pd nanoparticles synthesized by stepwise growth reaction (the scale bar is 20 nm) and corresponding size distribution histograms: (a) PdS1: PVP/Pd = 20, (b) PdS2: PVP/Pd = 10, (c) PdS3: PVP/Pd = 5, and (d) PdS4: PVP/Pd = 2.5.

4.1.1.3. Pd/γ-Al_2O_3 catalysts

The synthesized nanoparticles were deposited on γ-Al_2O_3 (the target loading is 0.3 wt.%) and the exact loadings determined via AAS are shown in Table 4.1. AAS analysis for one sample was repeated with 0.01 M disodium ethylenediamine tetraacetate (EDTA) in the solution. The error was 3.5%. Thus, EDTA was not used for further analysis.

Table 4.1. Pd loading on γ-Al_2O_3 determined by AAS.

One-step synthesis		Stepwise growth	
Sample designation	Loading wt.%	Sample designation	Loading wt.%
Pd1	0.08	PdS1	0.16
Pd2	0.17	PdS2	0.17
Pd3	0.19	PdS3	0.22
Pd4	0.20	PdS4	0.14

Nanoparticle sintering at high temperature could be a reason of deactivation in catalytic reactions. TEM results show that Pd nanoparticles were dispersed pretty evenly on γ-alumina (Fig. 4.4 (a)). The O_2-H_2 pretreatment step showed no significant sintering happening upon pretreatment (Fig. 4.4 (b)), but sintering could be observed on portions of the spent Pd catalysts (Fig. 4.4 (c)). Nanoparticles have several fold lower melting point than bulk metal; and the smaller the nanoparticle size, the lower the melting point. Usually sintering starts at 50% of the melting point in degrees Kelvin. Pd is the only catalyst exhibiting sintering, because it has lower melting point than Ir and Ru.

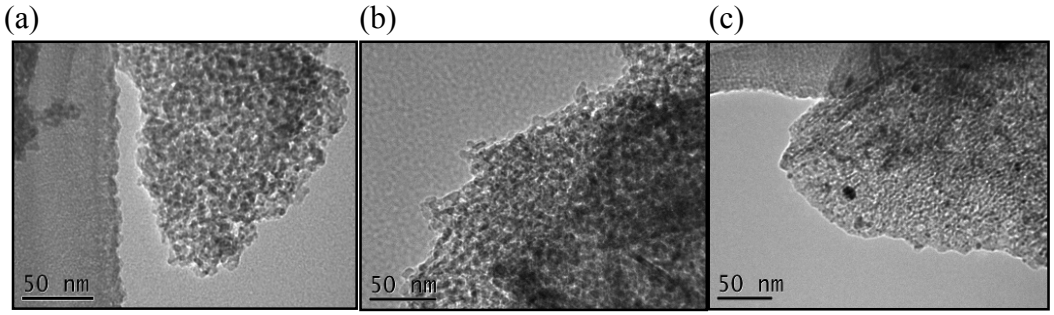

Figure 4.4. (a) PdS1/γ-Al_2O_3, (b) PdS1/γ-Al_2O_3 after O_2-H_2 pretreatment (burning in air at 200 °C and reducing in H_2 at 375 °C), and (c) after reaction.

4.1.2. Monometallic Ru/γ-Al_2O_3 catalysts

4.1.2.1. Ru nanoparticles via one-step growth

Size control of Ru nanoparticles in a one-step reaction was expected to be achieved by changing reduction temperature, mode of reactants addition, or type of metal precursors. Figure 4.5 shows TEM images and size distributions of PVP-stabilized Ru nanoparticles, Ru1 - Ru4, synthesized using $Ru(NO)(NO_3)_3$ precursors at various synthesis conditions (Table 3.3) and subjected to dialysis. Our results do not show dramatic particle size change with different reaction temperatures, e.g., Ru1, Ru2, and Ru3 catalysts have similar mean diameters of 2.3 nm, 2.2 nm and 2.0 nm, respectively. At a lower reduction temperature and using different modes of reactants addition, Ru4 shows relatively bigger particle size than Ru1, Ru2, and Ru3. For Ru4, slow addition of metal precursors to a boiling colloidal solution containing metal nanoparticles is known to produce larger nanoparticles [62].

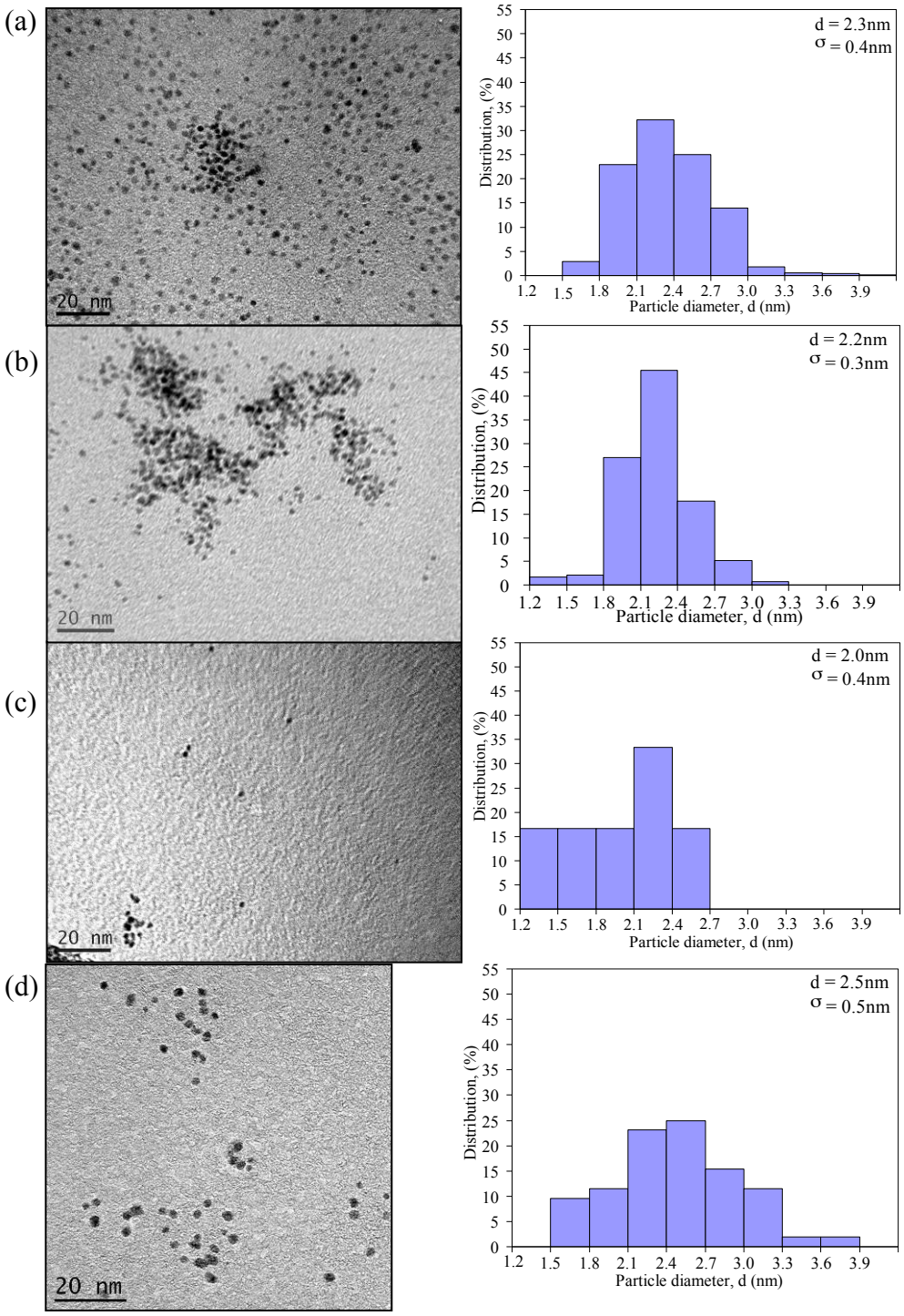

Figure 4.5. TEM photographs and the corresponding particle size distribution histograms of PVP-stabilized Ru nanoparticles synthesized by one-step reactions ($Ru(NO)(NO_3)_3$ precursor). (a), (b), (c) and (d) correspond to samples Ru1, Ru2, Ru3, and Ru4 respectively. The molar ratios of PVP/Ru were 10/1.

Repeated synthesis shows reproducible Ru nanoparticle size in the range of 2.0 - 2.5 nm (Fig. A3, Appendix A). It also shows that decreasing the molar ratio of PVP/Ru from 10/1 to 5/1 did not affect the particle size. Samples Ru1 - Ru4 show narrow size distributions (0.2 - 0.5 nm), which is a characteristic feature of the applied stabilization method. UV-vis spectra (Fig. 4.6) revealed a broad absorption band between 400 and 250 nm assigned to nanoparticle formation [70].

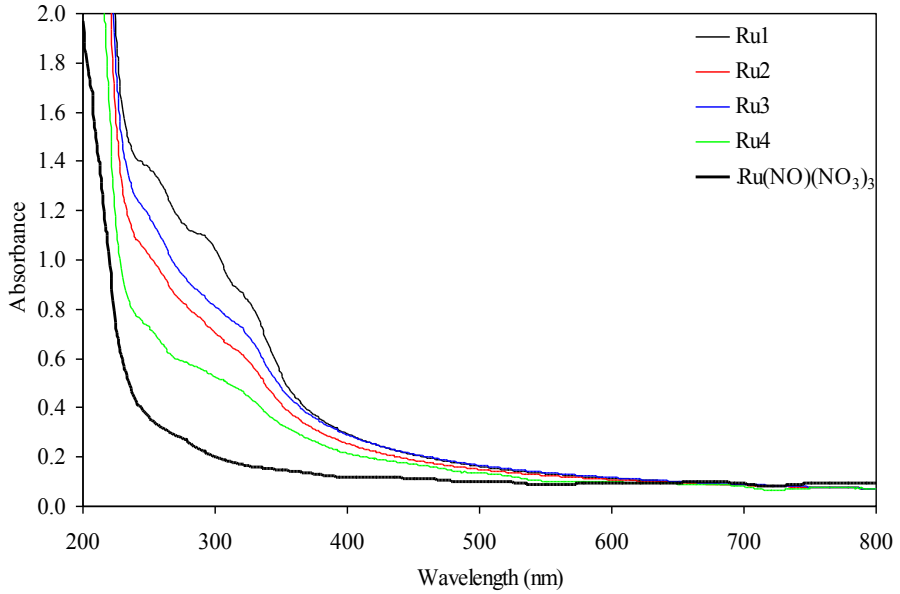

Figure 4.6. UV-vis spectroscopy of PVP-stabilized Ru nanoparticles and the precursor $Ru(NO)(NO_3)_3$.

Figure 4.7 shows TEM images of PVP-stabilized Ru nanoparticles, Ru5 and Ru6, synthesized using $RuCl_3$ precursors at various reduction temperatures and subjected to dialysis. Ru5 and Ru6 show filaments structures of Ru nanoparticles with diameters (individual particle size) of about 2 nm. Similar filaments structure of Pd-Ru bimetallic nanoparticles was reported by Tsang's group [71]. In their study, ruthenium chloride was used as precursors as well. Different reduction temperatures did not affect the size of Ru nanoparticles.

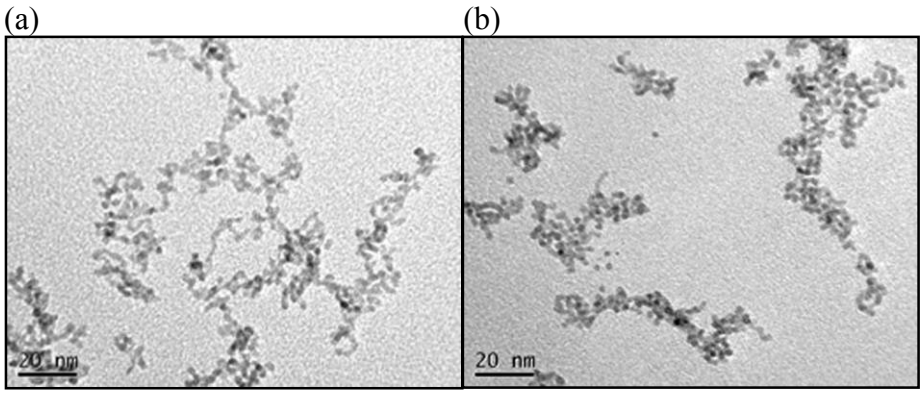

Figure 4.7. TEM photographs of PVP-stabilized Ru nanoparticles synthesized by one-step reactions ($RuCl_3$ precursor). (a) Ru5: reduction temperature 200 ^oC and (b) Ru6: reduction temperature 160 ^oC. The molar ratios of PVP/Ru were 10/1.

4.1.2.2. Ru nanoparticles via stepwise growth

Results from previous section show that with one-step reduction reaction, Ru nanoparticles size was barely affected, so seed growth method was applied for bigger Ru nanoparticles. However, seed-mediated growth using RuS1 seeds synthesized by one-step reaction did not result in nanoparticles with size growth, i.e., RuS1 and RuS2 have the same mean diameter of about 2 nm (Fig. 4.8).

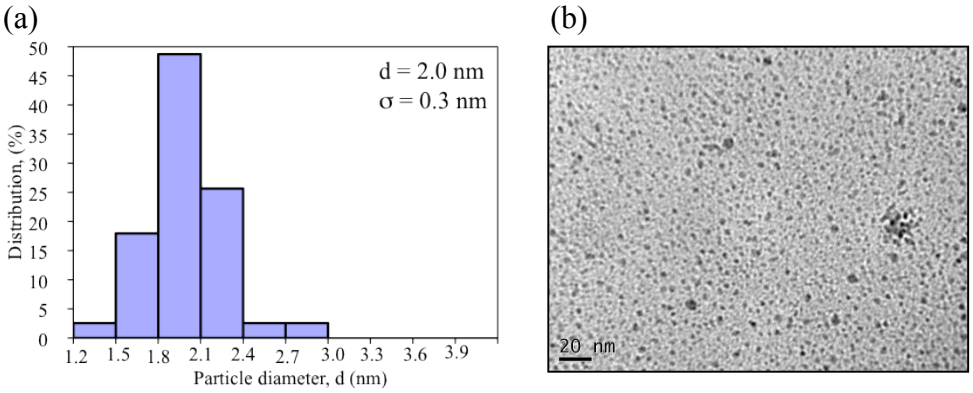

Figure 4.8. (a) particle size distribution for RuS1 colloids (seed) and (b) TEM photographs of RuS2 colloids obtained via stepwise growth method ($Ru(NO)(NO_3)_3$ precursor).

Therefore, Miyake's stepwise growth method for Pd was applied for the synthesis of bigger Ru nanoparticles and with some modifications. Figure 4.9 shows TEM images of PVP-stabilized Ru nanoparticles synthesized via stepwise growth method in ethanol/water under reflux for 3 hours. Ru nanoparticles synthesized in a one-step reaction (EG reduction), approximately 2 nm in mean diameter, were used as seeds for stepwise growth to obtain larger nanoparticles (Fig. 4.9 (a)). The mean diameter of Ru nanoparticles after the fourth growth reaction is approximately 3.0 nm (Fig. 4.9 (b)). Repeated synthesis showed RuS3 nanoparticle size of 2.5 nm (Fig. A3, Appendix A).

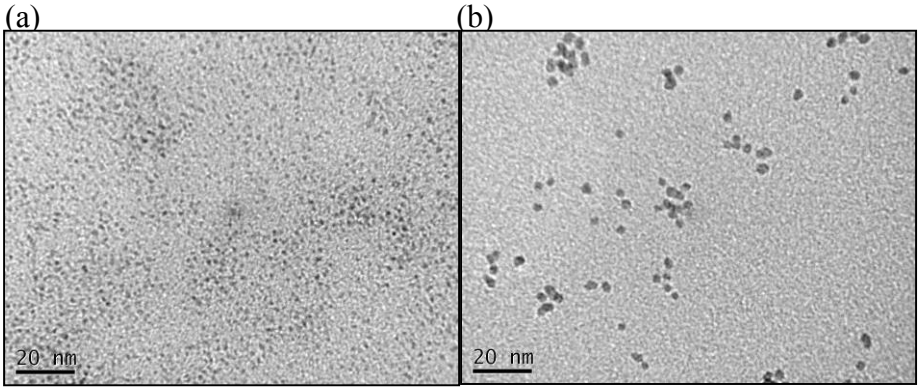

Figure 4.9. TEM photographs of PVP-stabilized Ru nanoparticles synthesized by stepwise growth method ($Ru(NO)(NO_3)_3$ precursor). (a) seeds and (b) RuS3 (fourth step growth).

4.1.2.3. Ru/γ-Al_2O_3 catalysts

The synthesized Ru nanoparticles were deposited on γ-Al_2O_3 (the target loading is 0.3 wt.%) and the exact loadings determined via AAS are shown in Table 4.2.

Table 4.2. Ru loading on γ-Al_2O_3 determined by AAS.

Sample designation	Loading wt.%
Ru1	0.16
Ru2	0.15
Ru3	0.14
Ru4	0.18
Ru5	0.23
Ru6	0.16
RuS1	0.25
RuS2	0.22
RuS3	0.26

Ru nanoparticles were dispersed evenly on γ-Al_2O_3. No significant sintering was observed on the pretreated and spent Ru1 catalysts (Fig 4.10).

(a) (b) (c)

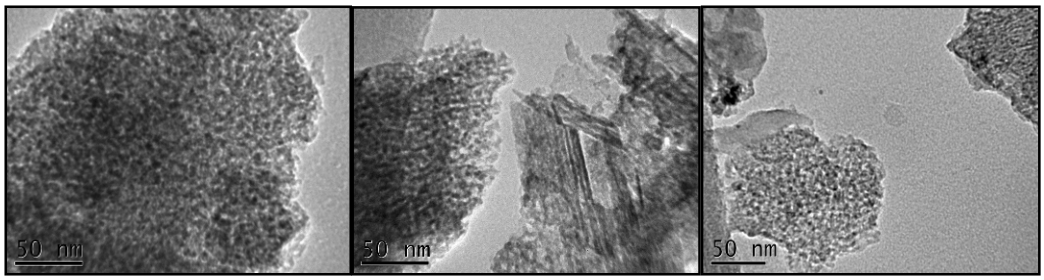

Figure 4.10. (a) Ru1/γ-Al_2O_3, (b) Ru1/γ-Al_2O_3 after O_2-H_2 pretreatment (burning in air at 200 °C and reducing in H_2 at 375 °C), and (c) Ru1/γ-Al_2O_3 after reaction.

4.1.3. Monometallic Ir/γ-Al_2O_3 catalysts

4.1.3.1. Ir nanoparticles via stepwise growth

Numerous studies have focused on the size control of nanoparticles, but none of them on Ir nanoparticles. Thus, stepwise growth method (the most effective method to control nanoparticle size) for Pd nanoparticles was applied for Ir size control. Also, in the seed preparation, Ir precursors were reduced by two different alcohols. Since *1*-propanol is a stronger reductant than ethanol, *1*-propanol will result a faster reduction rate of Ir ions, and therefore smaller nanoparticles.

Ir seeds synthesized in 1-propanol/water: Figure 4.11 shows TEM images and size distributions of PVP-stabilized Ir nanoparticles, IrS12 – IrS14 and seeds (repeated synthesis), synthesized by stepwise growth method in ethanol/water under reflux for 3 hours. Here *1*-propanol/water was used as a reducing agent to prepare only Ir seeds (IrS11). Further growth steps were carried out in ethanol/water. Unlike palladium, iridium does not show particle size growth, but worm-like filaments structure. Ir nanoparticles from all samples show the same average diameter of 1.9 nm, but different degrees of assembling. These filaments might be formed during growth in the colloidal solution due to self-assembly [72], since the Ir colloids (IrS12 - IrS14) were not deposited on TEM grids immediately after preparation, but one month later.

Repeated synthesis of Ir nanoparticles by *1*-propanol/water shows sphere Ir nanoparticles with mean diameter of 2.6 nm (Fig. 4.11 (d)). TEM sample was prepared immediately after synthesis reaction. This demonstrates that Ir nanoparticles were not stable in colloidal solutions, thus worm-like filaments were formed by self-assembly.

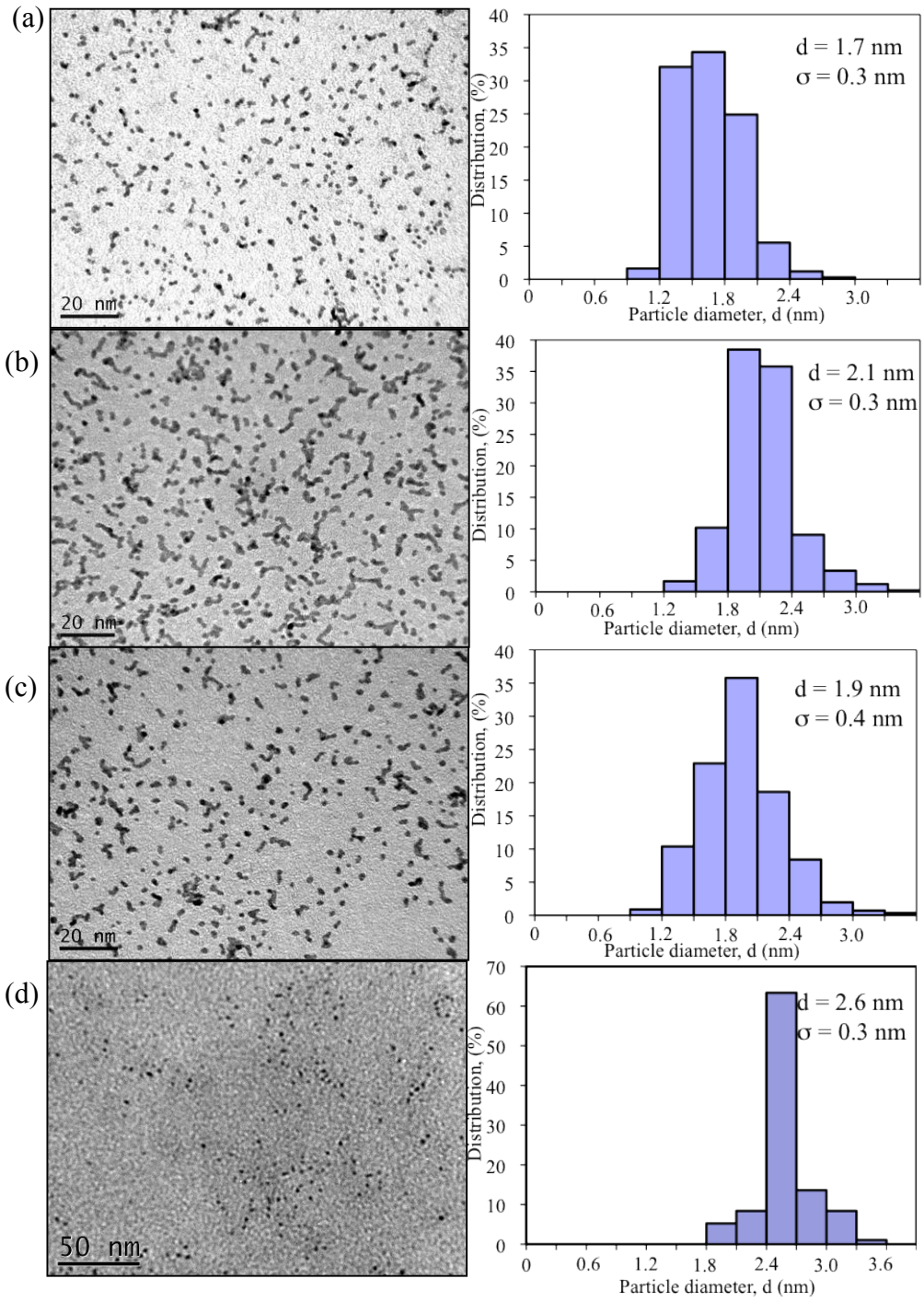

Figure 4.11. TEM photographs of Ir nanoparticles synthesized by stepwise reaction and corresponding size distribution histograms: (a) IrS12: second growth; PVP/Ir = 5, (b) IrS13: third growth; PVP/Ir = 2.5, (c) IrS14: fourth growth; PVP/Ir = 1.75, and (d) repeat of the seed preparation. Ir seed was prepared by *1*-propanol/water method.

Ir seeds synthesized in ethanol/water: Figure 4.12 shows TEM images and size distributions of PVP-stabilized Ir nanoparticles. IrS21, IrS22, and IrS24, synthesized by stepwise growth method in ethanol/water under reflux for 3 hours. Ir nanoparticle seeds for further stepwise growth were synthesized by ethanol/water as well. Again, Ir does not show particle size growth, but small nanoparticle sizes for all steps, i.e., average diameter of all samples is 1.7 nm. In this case, IrS21 and IrS22 show spherical Ir nanoparticles. However, when the PVP/Ir molar ratio decreased to 2.5, worm-like filaments could be observed in IrS24. These worm-like filaments were formed during synthesis due to low PVP concentration, as TEM samples for IrS24 was prepared immediately after synthesis reaction.

Size control: The mean diameter of Ir seeds prepared by ethanol/water ([EtOH] = 40 vol.%) shows 1 nm smaller (Fig. 4.12 (a)) than that of Ir seeds prepared by *1*-propanol/water ([*1*-PrOH] = 90 vol.%) (Fig. 4.11 (d)). This is consistent with the previous study on alcohol reduction method by Toshima. In their study, monodispersed Pd nanoparticles of smaller diameter (2 nm) were obtained at 40 vol.% EtOH, whereas bigger Pd nanoparticles (3.5 nm) were obtained at high *1*-propanol concentration (> 70 vol.%) [11]. Duding the synthesis, the concentration of *1*-PrOH is much higher than that of EtOH. In general, an increase in the concentration of the reducing agent increases the reduction rate of metal ions, leading to smaller metal nanoparticles, but this is not always true. At very high alcohol concentration (> 40 vol.%), metal salts will not homogeneously disperse in solution, resulting in a large size and wider distribution of nanoparticles [11].

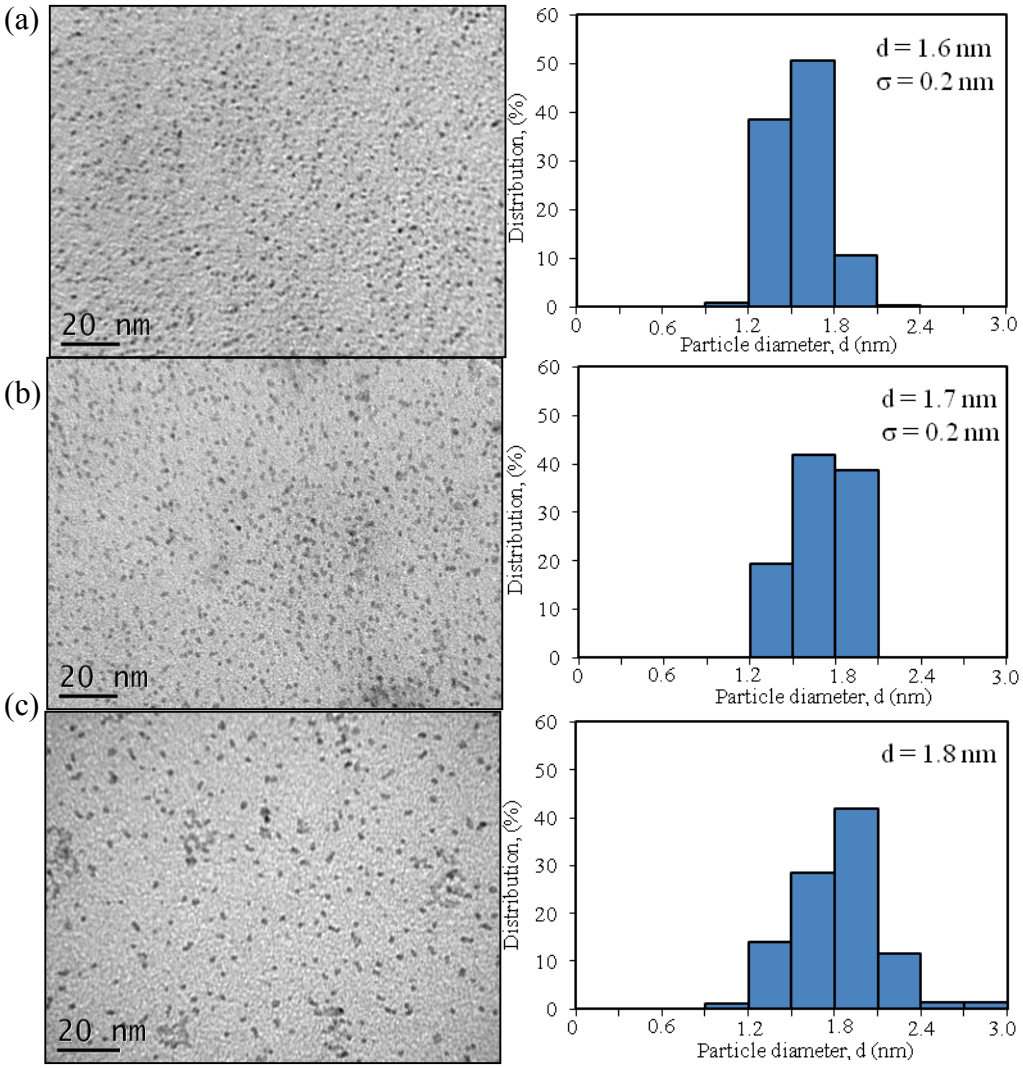

Figure 4.12. TEM photographs of Ir nanoparticles synthesized by stepwise reaction (the scale bar is 20 nm) and corresponding size distribution histograms: (a) IrS21: seed; PVP/Ir = 20, (b) IrS22: second growth; PVP/Ir = 10, and (c) IrS24: fourth growth; PVP/Ir = 2.5. Ir seed was prepared by ethanol/water method.

The formation of Ir nanoparticles was also confirmed by UV-vis spectroscopy. During the formation of Ir nanoparticles, the light brown solution containing $[IrCl_6]^{2+}$ ions turned into pale yellow then dark-brown. The absorption from the ultraviolet to the visible region increased, and the peaks at 425 nm and 500 nm disappeared after synthesis (Fig. 4.13). These peaks were ascribed to the

formation of Ir nanoparticles.

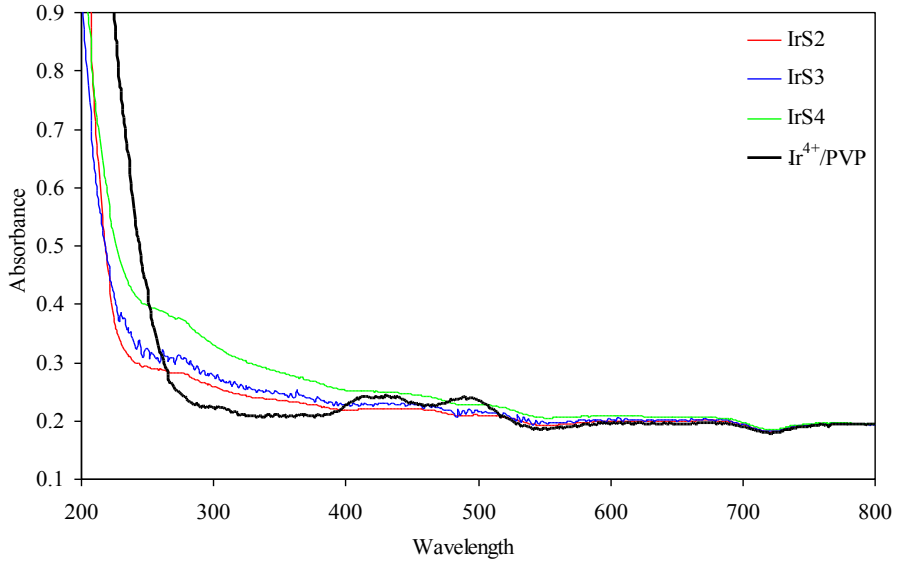

Figure 4.13. UV-vis spectroscopy of PVP-stabilized Ir nanoparticles and the precursor H_2IrCl_6.

4.1.3.2. Ir/γ-Al_2O_3 catalysts

The synthesized nanoparticles were deposited on γ-Al_2O_3 (the target loading is 0.3 wt.%). Supported Ir catalysts were submitted to neutron activation analysis (NAA) at either Slowpoke facilities at University of Alberta or the Becquerel Laboratories Inc. in Mississauga, Ontario for element analysis, as it is difficult to dissolve iridium with aqua regia for AAS. The exact loadings determined by NAA are shown in Table 4.3.

Ir nanoparticles were dispersed evenly on γ-Al_2O_3. No significant sintering was observed on the fresh and spent Ir catalysts (Fig. 4.14).

Table 4.3. Ir loading on γ-Al_2O_3 determined by NAA.

Seed synthesized in *1*-PrOH/water		Seed synthesized in EtOH/water	
Sample designation	Loading wt.%	Sample designation	Loading wt.%
IrS11	0.10 ± 0.003	IrS21	0.18 ± 0.005
IrS13	0.08	IrS22	0.15 ± 0.005
IrS14	0.08	IrS24	0.08 ± 0.003

(a) (b)

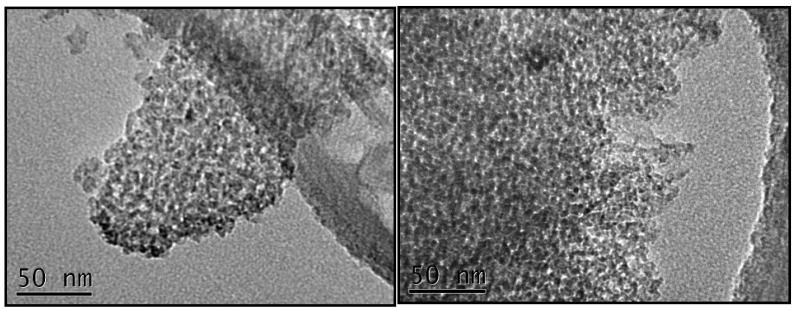

Figure 4.14. (a) IrS21/γ-Al_2O_3 and (b) IrS21/γ-Al_2O_3 after reaction.

4.1.4. Bimetallic catalysts

4.1.4.1. Alloy structures

For each bimetallic combination, nanoparticles were synthesized at three different ratios. For each ratio, two different sizes were expected, and the obtained bimetallic nanoparticles size control should follow the trend of each studied monometallic nanoparticles. Again, the optimal combination and composition of two metals for selective ring opening is not known yet. Bimetallic colloids (Pd-Ir, Ir-Ru, and Pd-Ru) were prepared via simultaneous reduction of two precursor salts in the presence of PVP. Based on our synthesis results of Pd, Ir, and Ru monometallic nanoparticles, Pd-Ir colloids were prepared by Miyake's ethanol

reduction method [11]; and both Ir-Ru and Pd-Ru colloids were prepared by Li's ethylene glycol reduction method [62]. Figures 4.15 - 4.17 show TEM images and corresponding size distributions of alloy structure bimetallic colloids of Pd-Ir, Ir-Ru, and Pd-Ru, respectively. Alloy structures will be confirmed by TEM-EDX (Energy-Dispersive X-ray spectroscopy) and Depth Profiling TOF-SIMS (Time-of-Flight Secondary Ion Mass Spectrometry) surface analyses in future studies.

Pd-Ir colloids: Pd-Ir colloids were synthesized at three Pd/Ir molar ratios: 3/1, 1/1, and 1/3; for each molar ratio, two different sizes were expected by changing the molar ratio of PVP/(Pd+Ir) from 40/1 to 10/1. As discussed in section 4.1.1, the lower the PVP to metal ratio, the larger the nanoparticles should be obtained [11], since PVP stabilizes the metal nanoparticles by preventing them from aggregation. The same idea applies to bimetallic nanoparticles. Our results show Pd3Ir1 particle size increases from 1.8 to 2.5 nm, when PVP/(Pd+Ir) molar ratio decreased from 40 to 10 (Fig 4.15 (a) and (b)). However, mean diameters of Pd1Ir1 and Pd1Ir3 were barely affected by changing the amount of PVP (Figs. 4.15 (c), (d), (e), and (f)), i.e., average mean diameters of 2.35 and 2.45 nm were obtained, respectively. This result is consistent with that of monometallic Ir colloids, where Ir nanoparticles did not show particle size growth with lowered amount of PVP. Moreover, with PVP/(Pd+Ir) molar ratios more than 2.5, nanoparticles were spherical; no worm-like filament of Pd-Ir was observed. Repeated synthesis shows reproducible Pd1Ir3_2 nanoparticle sizes of 1.9 nm (Fig. A4 (a), Appendix A).

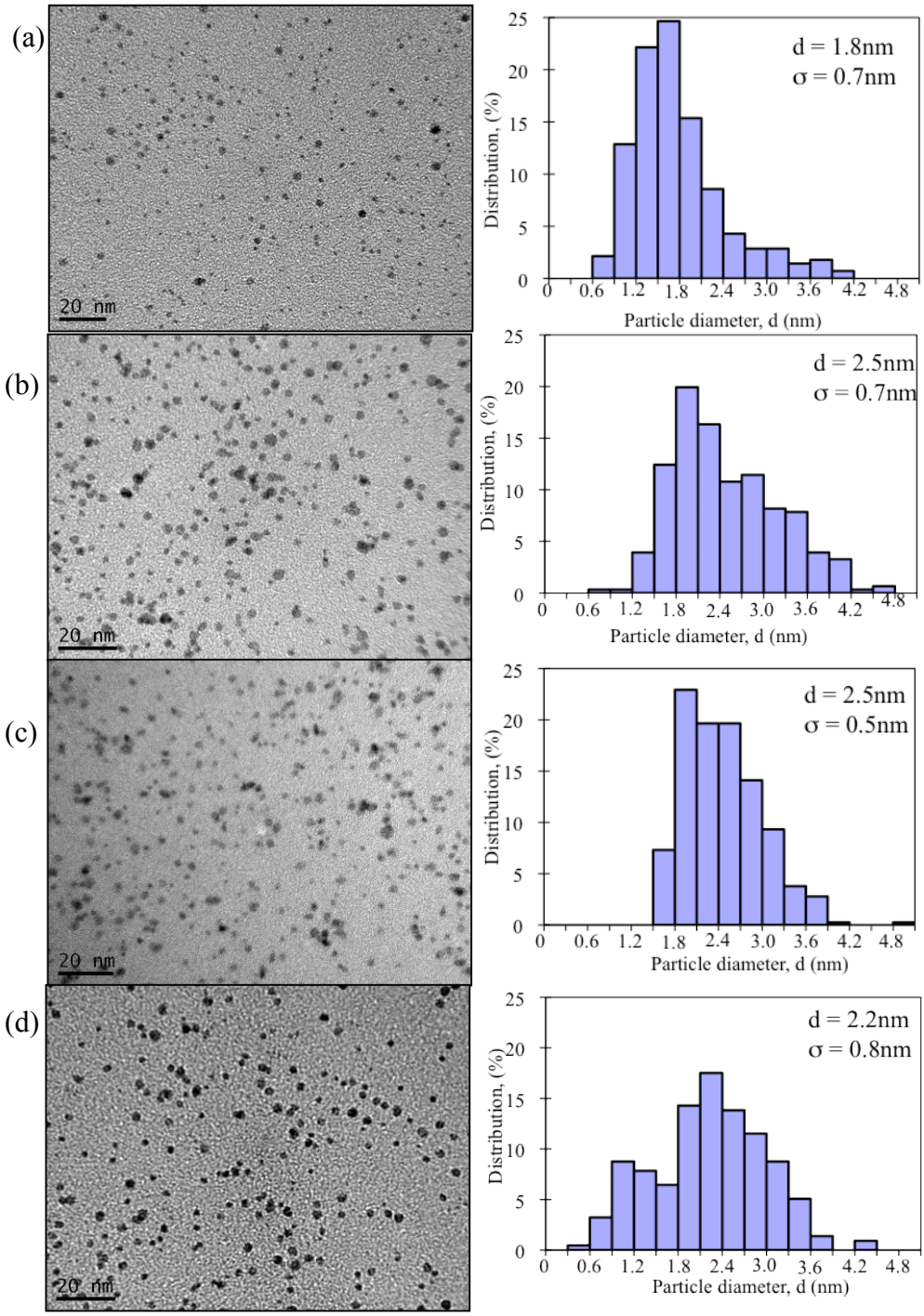
(a)
20 nm
d = 1.8nm
σ = 0.7nm
Distribution, (%)
Particle diameter, d (nm)
(b)
20 nm
d = 2.5nm
σ = 0.7nm
Distribution, (%)
Particle diameter, d (nm)
(c)
20 nm
d = 2.5nm
σ = 0.5nm
Distribution, (%)
Particle diameter, d (nm)
(d)
20 nm
d = 2.2nm
σ = 0.8nm
Distribution, (%)
Particle diameter, d (nm)

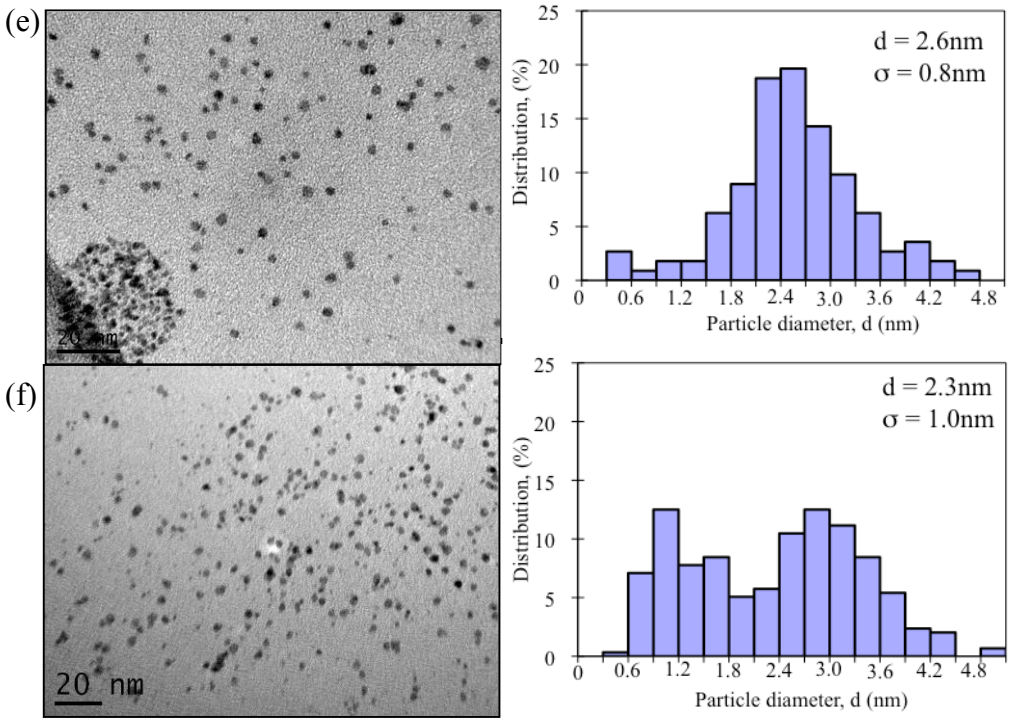

Figure 4.15. TEM photographs of bimetallic Pd-Ir colloids (the scale bar is 20 nm) and corresponding size distribution histograms: (a) Pd3Ir1_1, (b) Pd3Ir1_2, (c) Pd1Ir1_1, (d) Pd1Ir1_2, (e) Pd1Ir3_1, and (f) Pd1Ir3_2.

Ir-Ru colloids: Ir-Ru colloids were synthesized at three metal molar ratios: 3/1, 1/1, and 1/3; for each molar ratio, two different sizes were expected by changing the reduction temperature. We expected smaller particle size for refluxing at 200 ^{o}C and larger particle size at 160 ^{o}C according to Li's study on the size control of monometallic Ru nanoparticles [62]. It has been found that the particle size of Ir-Ru nanoparticles depends on neither the reduction temperature nor the molar ratio of these two metals. An average mean diameter of 2.0 nm was obtained among Ir-Ru alloy structures synthesized, which correlated with the sizes of monometallic Ru and Ir nanoparticles (2.0 - 2.4 nm and 1.6 - 1.8 nm, respectively). Also, as the amount of Ir increased, worm-like structures of Ir-Ru were observed as seen in Figure 4.16 (a). Repeated synthesis showed reproducible

Ir1Ru1_1 nanoparticle size of 2.1 nm (Fig. A4 (c), Appendix A).

Pd-Ru colloids: The synthesis and size control of Pd-Ru bimetallic alloy structures were the same as those for Ir-Ru nanoparticles. Significant size increase by decreasing reduction temperature could be observed from Figs. 4.17 (a) and (b), i.e., the mean diameter of Pd3Ru1 increased from 3.6 (Pd3Ru1_1) to 5.3 nm (Pd3Ru1_2). However, the mean diameters of Pd1Ru1 and Pd1Ru3 did not depend on the reduction temperature. With exactly the same synthesis method, it has been found that the more Ru in the alloy structure, the smaller the mean diameter of nanoparticles. This is likely because monometallic Ru nanoparticles with mean diameter greater than 2.5 nm could hardly be prepared through a one-step reaction, i.e., the largest monometallic Ru obtained by Li's one-step reaction method is 2.5 nm (see section 4.1.2).

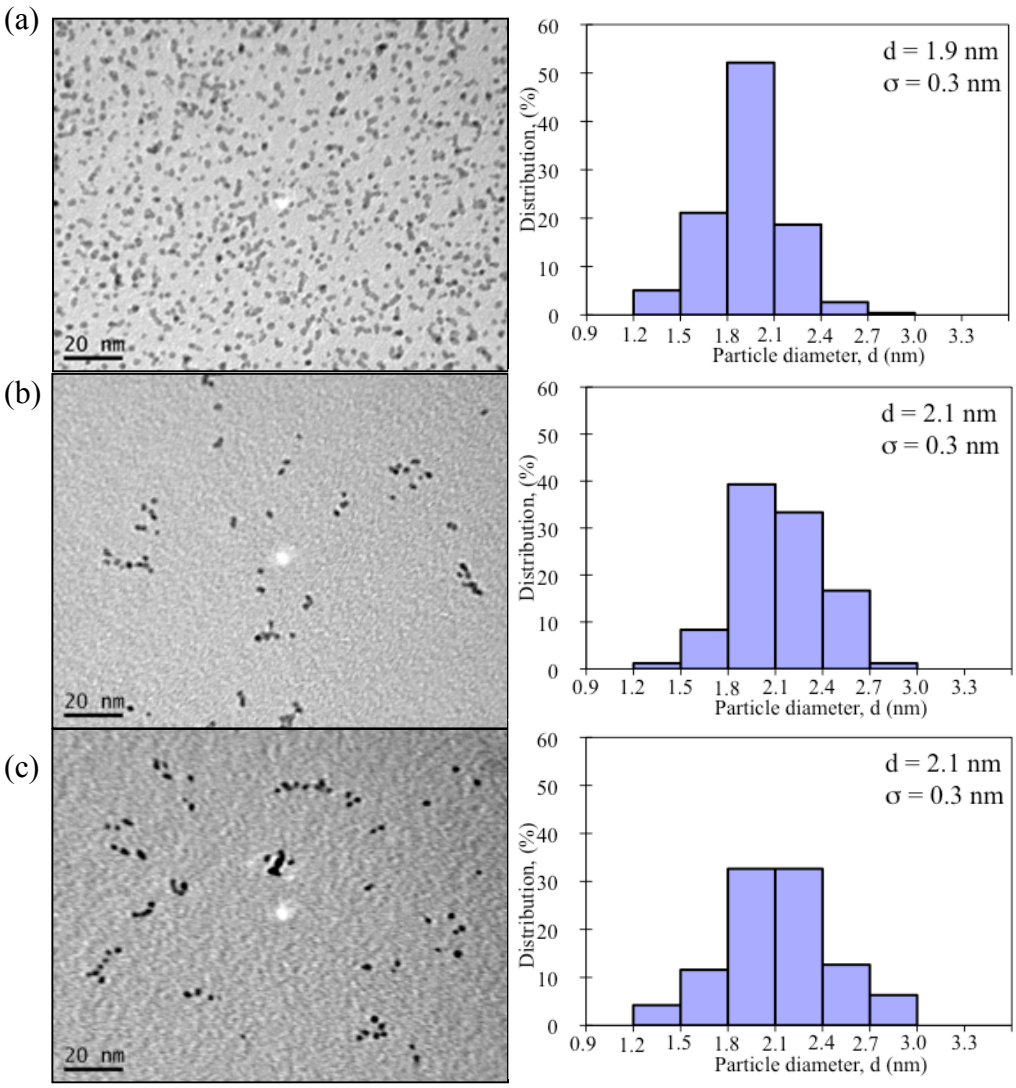

Figure 4.16. TEM photographs of bimetallic Ir-Ru colloids (the scale bar is 20 nm) and corresponding size distribution histograms: (a) Ir3Ru1_1, (b) Ir1Ru1_1, and (c) Ir1Ru_1.

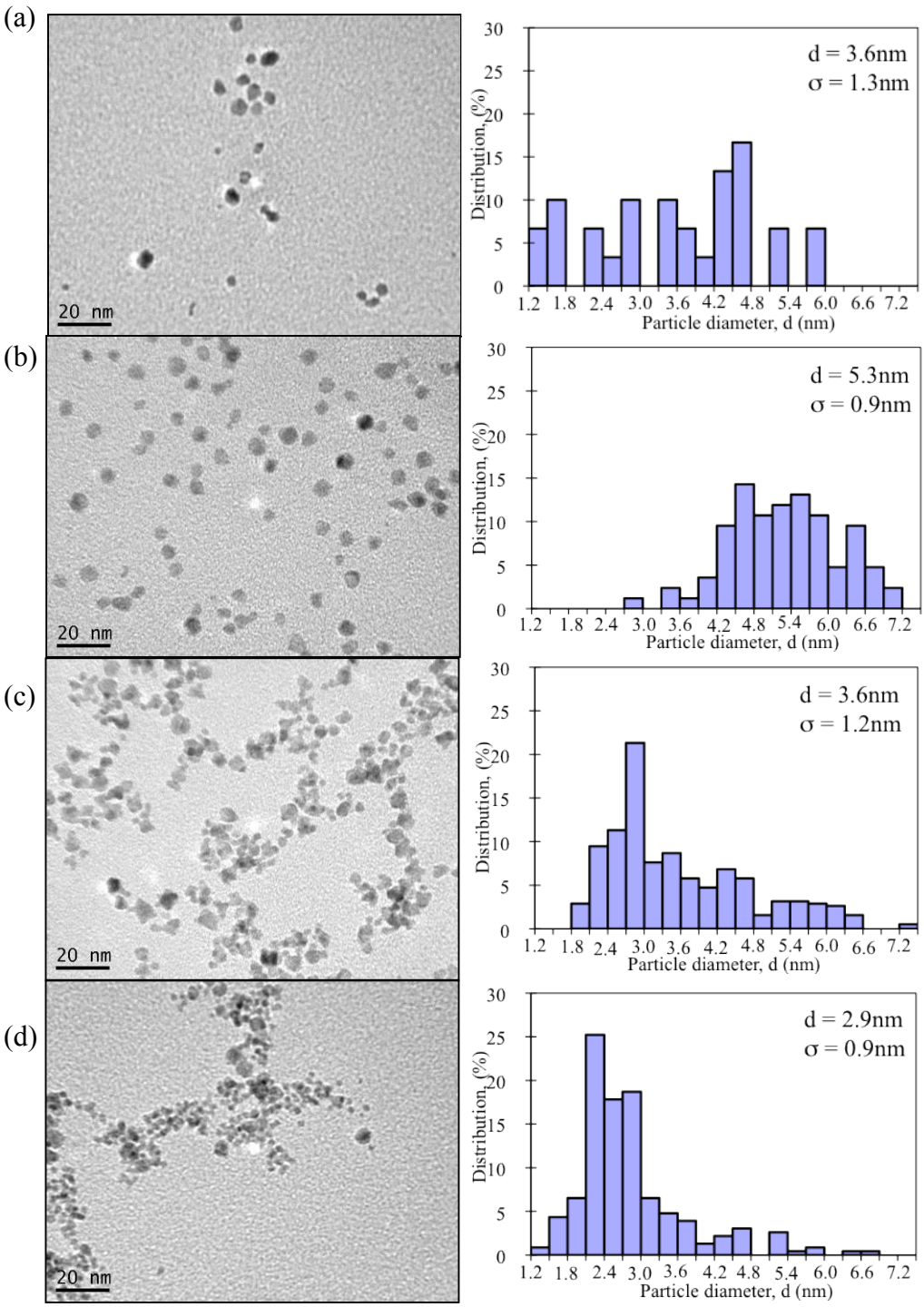

Figure 4.17. TEM photographs of bimetallic Pd-Ru colloids (the scale bar is 20 nm) and corresponding size distribution histograms: (a) Pd3Ru1_1, (b) Pd3Ru1_2, (c) Pd1Ru1_1, and (d) Pd1Ru3_2.

4.1.4.2. Core-shell structures

Two different core-shell structures of bimetallic colloids, Pd(c)Ir(s) and Pd(c)Ru(s), were prepared via Toshima's hydrogen-sacrificial technique [39]. The expected ratio of the core-shell metals was 1/1. The motivation to prepared Pd(c)Ir(s) catalyst is that Pd atoms in the core will have electronic effect on the shell Ir atoms, probably resulting in higher activity and stability (increased S-tolerance) than monometallic Ir catalysts in selective ring opening reactions. Similar synergistic effect is also expected for Pd(c)Ru(s) catalyst. After initial sulfidation in H_2S, the formed RuS_2 is the most active catalyst in hydrodesulfurization [65]. Figures 4.18 show TEM images and size distributions of core-shell structure bimetallic colloids of Pd-Ir and Pd-Ru. However, TEM images provided only presumable core-shell structures, which will be confirmed by TEM-EDX and TOF-SIMS surface analysis in future studies.

Pd(c)Ir(s) colloids: Pd core nanoparticles were synthesized using ethanol/water reduction method as for Pd1. Figure 4.18 (a) shows monodispersed Pd(c)Ir(s) nanoparticles with mean diameter of 2.7 nm, which is bigger than the size of monometallic Pd1 nanoparticles (2.3 nm) synthesized using the same method. Hydrogen, chemisorbed on palladium, reduced iridium precursors, and a shell was formed. Monometallic Ir synthesized by ethanol/water shows small Ir nanoparticles with mean diameter of 1.7 nm (see section 4.1.3). If monometallic Ir nanoparticles were formed, observed monometallic Ir nanoparticles from TEM image should have size no bigger than 1.7 nm, since H_2 is a stronger reducing agent than ethanol/water system. It is known that during the reduction reaction, a stronger reducing agent (such as H_2) leads to a faster reaction rate, thus smaller nanoparticle sizes [5, 10]. Figure 4.18 (a) also shows that 66% of the nanoparticles have diameters of 2.7 nm; and only 3% of the nanoparticles are

smaller than 1.8 nm. All of these are evidences for the formation of core-shell structures of Pd-Ir nanoparticles. Repeated synthesis showed reproducible Pd(c)Ir(s) nanoparticle size of 2.7 nm (Fig. A4 (b), Appendix A).

Pd(c)Ru(s) colloids: TEM image indicates the formation of core-shell structure of Pd-Ru colloids as well (Fig. 4.18 (b)). Both Pd and Ru nanoparticles prepared by one-step reactions show mean diameters no bigger than 3 nm (4.1.1 and 4.1.2). However, Pd(c)Ru(s) synthesized by hydrogen-sacrificial technique has a mean diameter of 3.3 nm, which is bigger than both monometallic Pd and Ru nanoparticles synthesized by a relatively weaker reducing agents than to H_2.

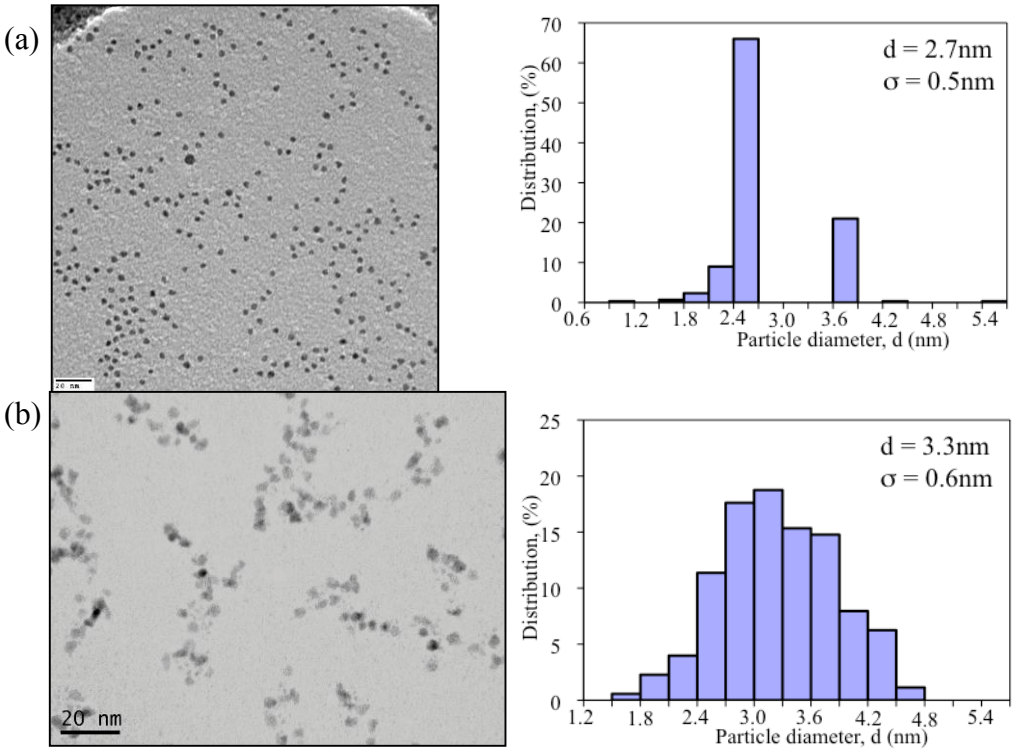

Figure 4.18. TEM photographs of bimetallic core-shell colloids prepared via hydrogen-sacrificial technique (the scale bar is 20 nm) and corresponding size distribution histograms: (a) Pd(c)Ir(s) and (b) Pd(c)Ru(s).

TEM image does not show significant sintering for the Pd(c)Ir(s)/γ-Al_2O_3 catalyst (Fig. 4.19) after the catalytic reaction (4 hours on stream).

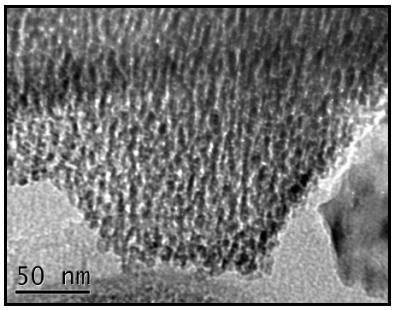

Figure 4.19. TEM image of spent Pd(c)Ir(s)/γ-Al_2O_3.

4.1.4.3. M1-M2/γ-Al_2O_3 catalysts

The synthesized bimetallic nanoparticles were deposited on γ-Al_2O_3 (the target loading is 0.3 wt.%). The exact loadings determined via NAA and M1 to M2 molar ratios are shown in Table 4.4.

Table 4.4. Bimetallic catalysts loading on γ-Al_2O_3 determined by NAA and corresponding M1 to M2 metal ratios.

Sample designation	M1 Loading wt.%	M2 Loading wt.%	Desired M1/M2 mol./mol.	Exact M1/M2 mol./mol.
Pd3Ir1_1	0.12 ± 0.002	0.05 ± 0.001	3/1	4/1
Pd3Ir1_2	0.25 ± 0.004	0.08 ± 0.001	3/1	6/1
Pd1Ir1_2	0.09 ± 0.002	0.10 ± 0.001	1/1	2/1
Pd1Ir3_2	0.05 ± 0.002	0.11 ± 0.001	1/3	1/1
Pd3Ru1_2	0.10 ± 0.001	0.04 ± 0.002	3/1	3/1
Ir3Ru1_1	0.16 ± 0.001	0.02 ± 0.001	3/1	9/1
Ir1Ru1_1	0.04 ± 0.001	0.04 ± 0.002	1/1	1/1
Ir1Ru3_1	0.03 ± 0.001	0.06 ± 0.002	1/3	1/2
Pd(c)Ir(s)	0.27 ± 0.010	0.39 ± 0.003	1/1	1/1

4.1.5. PVP removal

Prior to low-pressure ring opening of indan, the active sites of nanoparticles must be made available for chemisorption. As described in section 3.4.1, the catalysts were subjected to oxidation-hydrogenation pretreatment to remove PVP. The treatment was chosen based on the study of Somorjai et al. [68]. According to the XPS analysis of the catalysts after the pretreatment (Table 4.5), the mass ratio of metal-to-nitrogen shows 95% removal of PVP as compared to the ratio used in the synthetic procedures.

Table 4.5. XPS composition results (in mass concentration).

Catalysts / Surface mass %	Ru2	IrS13	PdS4
Metal	52%	41%	26%
Al	43%	49%	68%
N	3.1%	8.0%	3.7%
Cl	1.1%	1.8%	3.1%

4.2. Low-pressure ring opening of indan

4.2.1. Mass transfer limitations

For heterogeneous reactions, mass transfer first takes place from the bulk fluid to the catalyst surface (external mass transfer). The reactant molecules then diffuse through and into the pores of catalyst support (internal mass transfer). In

order to study the intrinsic catalytic properties of metal nanoparticles, the absence of mass transfer limitations must be verified.

4.2.1.1. External mass transfer limitation

The absence of external mass transfer limitations was first verified experimentally. Two RO reactions were performed over 0.669 g of Ir3Ru1_1 catalyst (metal loading is 1.2 mg) from the same batch at two different indan flow rates. The first reaction was carried at 2.4×10^{-5} g/min indan flow rate; and then RO of indan at same reaction conditions was repeated at 4.4×10^{-5} g/min indan flow rate, which is 1.8 times higher. For most of the RO reactions, indan flow rates were within this range (2.4×10^{-5} to 4.4×10^{-5} g/min). Indan conversion decreased from 60% to 35% (1.7 times lower). At a constant metal volume, indan conversion decreased proportionately with increasing indan flow; therefore, it can be concluded that external mass transfer was not limiting ring opening of indan at our reaction conditions.

4.2.1.2. Internal mass transfer limitation

Then Weisz-Prater parameter was calculated to verify the absence of internal mass transfer limitation. The Weisz-Prater criterion uses measured values of the rate of reaction, to determine if internal diffusion is limiting the reaction. Weisz-Prater parameter, C_{WP}, can be written as [73]

$$C_{WP} = \eta \times \phi_1^2 \tag{4.4}$$

$$= \frac{observed \quad (actual) \quad reaction \quad rate}{reaction \quad rate \quad evaluated \quad at \quad C_{As}} \times \frac{reaction \quad rate \quad evaluated \quad at \quad C_{As}}{a \quad diffusion \quad rate}$$

$$= \frac{actual \quad reaction \quad rate}{a \quad diffusion \quad rate}$$

η and ϕ_1^2 can be written as [73],

$$\eta = \frac{-r_A^{'}(obs)}{-r_A^{'}} \quad ; \quad \phi_1^2 = \frac{-r_{As}^{''} S_a \rho_c R^2}{D_e C_{As}} = \frac{-r_A^{'} \rho_c R^2}{D_e C_{As}} \tag{4.5}$$

Substituting Equations 4.5 into Equation 4.4, Weisz-Prater parameter can be rearranged to [73],

$$C_{WP} = \eta \phi_1^2 = \frac{-r_A^{'}(obs)}{-r_{As}^{'}} \left(\frac{-r_{As}^{'} \rho_c R^2}{D_e C_{As}} \right) = \frac{-r_A^{'}(obs) \rho_c R^2}{D_e C_{As}} \tag{4.6}$$

where

$-r^{'}_A(obs)$ = observed reaction rate, $mol_{indan}/(g_{cat.} \cdot s)$.

ρ_c = catalyst density, 3.67 g/mL [74], which is assumed to be the same as the density of γ-Al_2O_3, since the metal loading is very low.

r = the radius of catalyst particle (γ-Al_2O_3), 0.005 cm;

C_{As} = concentration of indan at the catalyst surface, mol/mL. In this case it is the bulk concentration of indan, because the absence of external mass transfer limitation has been verified.

D_e = effective diffusivity, cm^2/s,

In heterogeneous reaction, reactant molecules diffuse into the pores of catalyst, where catalytic reaction happens. Firstly, not all the pores are available for diffusion (porosity); secondly, the diffusion paths are tortuous (tortuosity); thirdly, the pores have varying cross-sectional areas (constrictivity). Therefore, the effective diffusivity can be calculated by [75, 76]

$$D_e = D\frac{\varepsilon\delta}{\tau} \tag{4.7}$$

where D = diffusion coefficient in gas, m^2/s

ε = porosity

δ = constrictivity

τ = tortuosity

Table 4.6. Parameters for effective diffusivity [73, 76].

D, cm^2/s	ε	δ	τ
0.2925	0.4	0.8	2

(D is the diffusion coefficient of indan in air at 336 ^oC)

If $C_{WP} << 1$, there are no diffusion limitations and consequently no concentration gradient exists within the pellet. If $C_{WP} >> 1$, internal diffusion limits the reaction severely [73].

In this study, indan ring opening reaction over 1.9 nm Ir3Ru1_1 catalyst is taken as an example for Weisz-Prater parameter calculation, as Ir3Ru1_1 is one of the most active catalysts (Table 4.7 for experimental details).

Observed reaction rate calculated from the activity is 2.5×10^{-9} $mol_{indan}/(g_{cat.}\cdot s)$. Bulk indan concentration calculated from known indan flow rate is 4.1×10^{-9} mol/cm^3. Then substituting the parameters in Table 4.6 to Equation 4.7, the

obtained effective diffusivity is 0.05 cm^2/s. Finally, substituting all the known parameters into Equation 4.6, Weisz-Prater parameter, C_{WP}, is 0.0012, which is much less than 1. Therefore, there is no internal diffusion limitation (Table 4.8).

Table 4.7. Reaction conditions and experimental data of indan ring opening over 1.9 nm Ir3Ru1_1/γ-Al_2O_3 catalyst (Appendix B).

Catalyst	Ir3Ru1_1
Catalyst weight, g	0.669
Metal loading, mg	1.2
Indan flow rate, 10^{-5} g/min	2.4
H_2 flow rate, mL/min	50
Activity, 10^{-3} $g_{indan}/(g_{metal} \cdot min)$	9.8

Table 4.8. Weisz-Prater criterion calculation.

$-r'_A(obs)$, $mol_{indan}/(g_{cat.} \cdot s)$	-2.5×10^{-8}
ρ_c, g/cm^3	3.67
r, cm	0.005
D_e, cm^2/s	0.05
C_{As}, mol/cm^3	4.1×10^{-9}
$\boldsymbol{C_{WP}}$	**0.0012 << 1**

Thus, the catalytic reaction results presented below are characteristics of intrinsic catalytic activity of synthesized metal nanoparticles.

4.2.4. Catalytic reaction results

In order to propose the optimal catalyst for selective ring opening, ring opening of indan was studied with the synthesized mono- and bi-metallic catalysts, and their catalytic performances were compared with an industrial Pt-Ir catalyst.

4.2.4.1. Ring opening of indan over industrial Pt-Ir catalyst

Low-pressure ring opening of indan was first studied over industrial Pt-Ir catalysts; the amount of catalyst was varying from 0.02 to 0.2 g, average indan flow rate was $(2.6\pm0.3) \times 10^{-5}$ g/min for five RO reactions, and the obtained indan conversion was ranging from 5 to 70%. The obtained catalytic activities were quite constant with an average of $(14.3\pm0.9) \times 10^{-3}$ $g_{indan}/(g_{metals}\cdot min)$. Selectivities to *2*-ethyltoluene and *n*-propylbenzene ("single cleavage selectivity"), *n*-propylbenzene, and lights were (47±9)%, (7±2)%, and (10±2)%, respectively.

Figures 4.20 (a), (b), and (c) show conversion versus time on stream (TOS), selectivity to single cleavage, and selectivities to all ring opening products over 0.208 g industrial catalysts. The average values such as catalytic activity and selectivities obtained by performing five indan ring opening reactions over industrial Pt-Ir catalysts were used to compare with synthesized mono- and bimetallic nanocatalysts. It has been found that steady state was established after 150 min TOS, so all the calculations and comparisons were using data obtained at steady state.

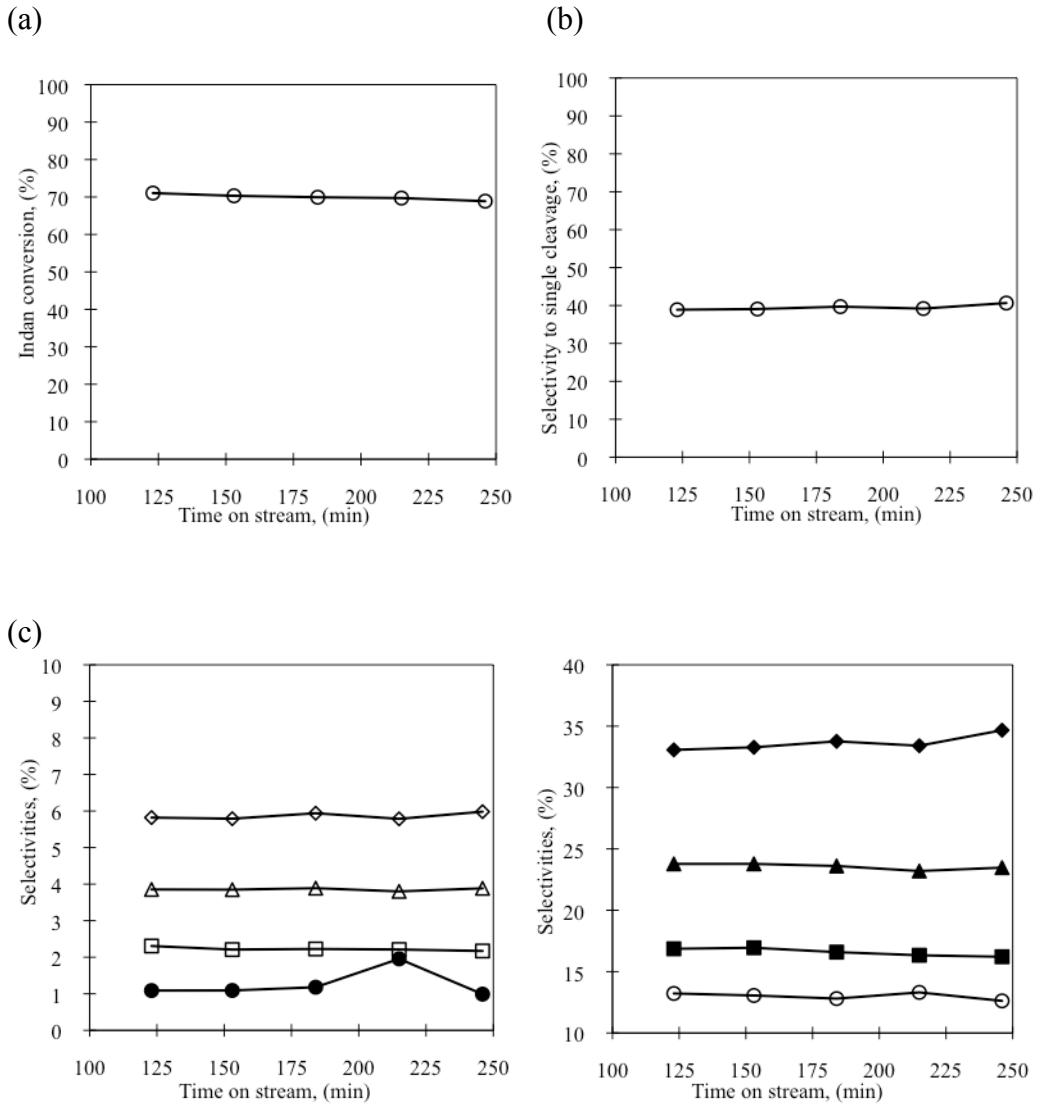

Figure 4.20. Low-pressure ring opening of indan over industrial Pt-Ir catalyst (0.208g): (a) indan conversion, (b) selectivity to single cleavage, and (c) selectivities to ring opening products. Reaction conditions: indan flow rate was 2.4 $\times 10^{-5}$ g/min, H_2/Indan molar ratio was 10136, and reaction temperature was 336 ^{o}C, reaction pressure was 1 atm pressure.

Reaction products: Benzene (□), toluene (■), ethylbenzene (□), *o*-xylene (▲), *n*-propylbenzene (□), *2*-ethyltoluene (□), lights (○), others (●).

4.2.4.2. Ring opening of indan over monometallic catalysts

In order to obtain the catalytic behavior of each metal, low-pressure ring opening of was then studied over synthesized monometallic catalysts first. This could help to understand the catalytic performance of the bimetallic structures later.

Among the synthesized monometallic catalysts, only Pd1/γ-Al_2O_3 (2.3 nm), PdS4/γ-Al_2O_3 (4.4 nm), Ru1/γ-Al_2O_3 (2.3 nm), IrS21/γ-Al_2O_3 (sphere 1.6 nm), and IrS11(worm)/γ-Al_2O_3 were studied in low-pressure ring opening of indan, as representative batches of the synthesized catalysts. IrS21 (sphere) with mean diameter of 2.6 nm can be studied in the future for size effect.

Activity. Figure 4.21 is the comparison of activities among different sizes or structures of monometallic catalysts (Pd1, PdS4, Ru1, and Ir spherical and worm-like particles), as well as for industrial Pt-Ir catalyst.

Figure 4.21 shows that Ir catalyst with sphere structures and mean diameter of 1.6 nm is the most active catalyst, which converted 19×10^{-3} $g_{indan}/(g_{metals}\cdot min)$. As compared to the commercial Pt-Ir catalyst, Ir sphere shows 1.4 times higher catalytic activity. Ir catalyst with worm-like structures does not show very high activity (5.1×10^{-3} $g_{indan}/(g_{metals}\cdot min)$) as compared to Ir spheres and industrial catalysts, which is most likely due to the reduced active surface area. Ru catalyst with a mean diameter 2.3 nm was not as active as Ir spheres but still comparable with the industrial catalyst. Pd catalysts exhibited the lowest activities. Catalytic activity for 2.3 nm and 4.4 nm Pd catalysts were only 0.6×10^{-3} and 0.1×10^{-3} $g_{indan}/(g_{metals}\cdot min)$, respectively. Similar order-of-magnitude lower activity as compared to iridium was reported for monometallic platinum catalyst in indan ring opening [59]. Also, Ir is known to be the most active and selective catalyst for RO of methylcyclopentane among all the noble metal catalysts studied [52]. In

our study the palladium catalyst showed nanoparticle sintering under reaction conditions (Fig. 4.4 (c)), which could be of the reason of low catalytic activity. Dieguez et al. reported that deactivation occurred for all Pd/Al_2O_3 catalysts with different palladium contents in the hydrogenolysis of methylcyclopentane. In their study, $PdCl_2$ was used as metal precursors as well. $Pd/\gamma\text{-}Al_2O_3$ catalysts were prepared by the traditional incipient wetness impregnation method without precisely controlled particle sizes [77].

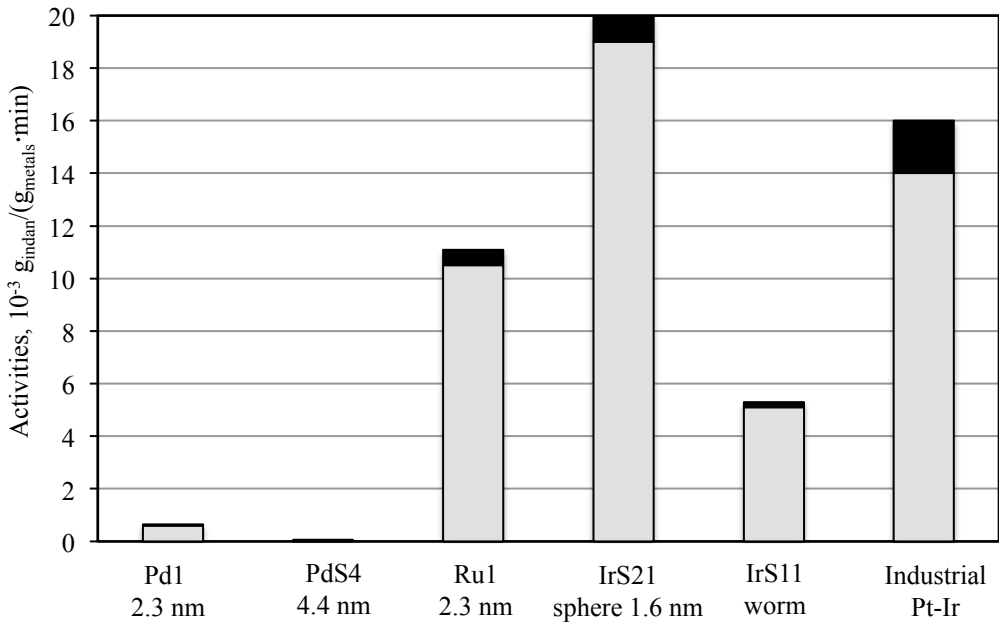

Figure 4.21. Comparison of catalytic activity among synthesized monometallic catalysts and industrial polydispersed Pt-Ir catalysts. Reaction conditions: indan flow rate was ranging from 2.2 to 3.3×10^{-5} g/min, H_2/Indan molar ratio was ranging from 7377 to 11066, reaction temperature was 336 ^{o}C, reaction pressure was 1 atm pressure, and metal loading was 1.2 mg for all catalysts.

Based on the comparison of catalytic activities, it can be concluded that the activity of supported monometallic nanosized catalysts is in the order of Ir sphere > industrial Pt-Ir > Ru > Ir worm >> Pd. The observed trend could be not only due to different metal nature, but also due to different metal nanoparticle size, structure, and shape. Turnover frequencies were not calculated because Pd sintered during reactions, and RO of indan was not carried out in a differential reactor.

RO selectivity. In this study, the sum of the selectivities to *2*-ethyltoluene and *n*-propylbenzene is named as "single cleavage selectivity", since *2*-ethyltoluene and *n*-propylbenzene are the desired products, when the naphthenic ring is cleavage only once.

Comparisons of catalytic selectivities to single cleavage, *n*-propylbenzene, *o*-xylene and lights among synthesized monometallic catalysts and industrial Pt-Ir catalysts are shown in Table 4.9. PdS4 is not included because it is not active. It can be seen that Pd and Ir catalysts allow better selectivities to single cleavage and *n*-propylbenzene as compared to industrial Pt-Ir catalyst (Table 4.9). Among the monometallic catalysts studied, Ir with worm-like structure leads to the highest selectivity to single cleavage (91%) and highest selectivity to *n*-propylbenzene (13%). Ir catalysts also result in less cracking, i.e., Ir catalysts with both structures have low selectivity to lights (2% for worm-like structure, and 4% for sphere structure) than that of industrial Pt-Ir catalyst. Boutonnet et al. have reported high selectivity (68%) to ring opening products over 2 wt.% Ir/boehmite at steady state [59]. Also, in a study of ring opening of cyclohexane, 4.6 nm Ir catalyst showed high conversion, high selectivity to desired *n*-hexane (72%), and low selectivity toward undesired benzene (0.5%) and lights (3%) [78]. On the other hand, selectivity to lights over 2.3 nm Pd catalyst (15%) is higher than that of industrial

catalyst (11%). Hydrocracking products were also found in the hydrogenolysis of methylcyclopentane (MCP) over 1 wt.% Pd/Al_2O_3 [77].

Table 4.9 also shows that 2.3 nm Ru catalyst results in low selectivities to single cleavage (10%) and to *n*-propylbenzene (< 1%) as compared to industrial Pt-Ir catalyst (Table 4.9). Moreover, selectivities to undesired products, such as *o*-xylene (38%), toluene (19%) and lights (23%) are very high as compared to the selective ring opening products (10%) (Appendix B). Among the studied catalysts, the characteristic feature of Ru is its high selectivity towards *o*-xylene. Previous studies on the hydrogenolysis of cyclohexane over Ru/Al_2O_3 catalyst shows Ru was less selective to desired *n*-hexane formation than Rh, and had a high cracking selectivity (45%) [79]. Kustov et al. have also reported that the hydrogenolysis of cyclohexane was non-selective over 1 wt.% Ru/Al_2O_3 as the reaction temperature reached 280 ^{o}C, which led to a 100 wt.% yield of light products (C_1-C_3) [80]. Moreover, ring opening of methylcyclopentane shows that C_1-C_5 cracking products were favored in the present of 1.5 wt.% Ru/SiO_2 [52].

Based on the comparison of RO selectivities with industrial Pt-Ir catalyst, it can be concluded that:

- From both selective RO and cetane number improvement points of view, Ir nanosized catalysts with both worm-like and sphere structures performed better than industrial catalyst, thus, Ir nanocatalyst should be considered as a valid alternative to the industrial catalyst either in its monometallic form or as a component of a bimetallic catalyst;
- Ru nanosized catalyst leads to excessive cracking and thus is not suitable for selective ring opening;
- Although Pd nanosized catalyst shows high RO selectivity (74%), it has the lowest activity and also its monometallic form is known to be readily

poisoned by sulfur compounds, so it should not be considered as an alternative to the industrial catalyst.

Table 4.9. Comparison of selectivities to single cleavage, *n*-propylbenzene, *o*-xylene, and lights for indan ring opening over nanosized monometallic catalysts. Metal loading was 1.2 mg for Pd1, Ru1, Ir worm, and industrial Pt-Ir catalysts; and 0.6 mg for Ir sphere catalyst. Data in brackets are one standard deviation.

Catalysts	Indan flow 10^{-5} g/min	Indan conversion %	Selectivities, %			
			Single cleavage	*n*-propylbenzene	*o*-xylene	Lights
Pd1	2.2	3	74 (4)	10.7 (0.6)	2.2 (0.1)	15 (2)
Ru1	2.8	45	9.9 (0.2)	0.89 (0.01)	37.5 (0.2)	22.7 (0.3)
IrS11[a] worm	2.3	25	90.5 (0.5)	12.8 (0.2)	3.2 (0.1)	2.32 (0.02)
IrS21[b] sphere	2.5	45	75 (1)	11.7 (0.3)	12 (1)	4.3 (0.2)
Industrial Pt-Ir	2.5 (0.1)	63 (6)	44 (4)	6.2 (0.4)	21 (4)	11 (1)

[a] in the first step, Ir precursors were reduced by *1*-propanol/water.

[b] in the first step, Ir precursors were reduced by ethanol/water.

Ring opening mechanisms. Two possible ring opening paths for indan are dicarbene mode and π-adsorbed olefin mode. Dicarbene mode results in C-C cleavage of unsubstituted secondary-secondary carbon atoms (α-ring opening in our case), producing highly branched isoparaffins with low CN; whereas π-adsorbed olefin mode achieves C-C cleavage at substituted positions (β-ring opening in our case), which eliminates branching and enhances the CN [51]. One of our goals for selective ring opening of indan is cetane number improvement. This can be achieved only when the C-C bond rupture occurs at a substituted

position, i.e., α-ring opening. Our results show that ring opening of indan over Pd and Ir catalysts follow both the dicarbene and π-adsorbed olefins mechanisms (the latte is more dominant), as *n*-propylbenzene and *2*-ethyltoluene are two main RO products. This is consistent with previous studies on ring opening of six-membered naphthenic rings, for example, McVicker et al. have indicated the propensity of Ir to cleave C-C bonds via the dicarbene path [43, 51, 81, 82, 83, 84]. It has been found that both Pd and Ir nanosized catalysts have higher selectivities to the rupture of substituted C-C bonds than Ru nanosized catalyst, thus Pd and Ir nanosized catalysts could enhance CNs. The very high selectivity to *o*-xylene (38%) and extremely low selectivity to *n*-propylbenzene (< 1%) observed in 2.3 nm Ru nanocatalyst indicate that dicarbene mode is most likely the only ring opening path for Ru nanocatalyst, since *o*-xylene is formed from the β-ring opening product, *2*-ethyltoluene (Table 4.9).

Structure effect. As discussed above, relatively high activity was obtained over 2.3 nm Ru nanocatalyst; however, Ru catalyst with nanosized filaments structures (Ru6) is nearly not active (0.1×10^{-3} $g_{indan}/(g_{metal}\cdot min)$) (Appendix B). Similar results over Ir catalysts can be also observed. 1.6 nm Ir with sphere is the most active catalyst (19×10^{-3} $g_{indan}/(g_{metal}\cdot min)$); however, Ir catalyst with worm-like structure allows 5×10^{-3} $g_{indan}/(g_{metal}\cdot min)$ activity, which is only ¼ of that for Ir sphere (Fig. 4.21). As the filaments are formed, significant portions of active sites of nanoparticles are blocked by each other, therefore, less active in RO reaction. There is a higher proportion of active sites being blocked for Ru6 (filaments) than that for Ir (worm-like structure), since the latter contains lower degree of assembling, i.e., only 2 to 4 units for each worm-like filament. The higher the degree of assembling, the higher portion of active sites are blocked; therefore, Ru6 is not active for RO of indan.

Although monometallic forms of Pd and Ru nanocatalysts did not show superior catalytic behavior as compared to the polydispersed industrial Pt-Ir catalyst in the low-pressure ring opening of indan, they are valuable candidates for bimetallic catalysts. Upon alloying two metals, synergism can be achieved due to electronic effects discussed in the literature review, e.g., a Ru-Pt catalyst with Ru excess on the surface resulted in the synergism factor of 4 in a ring opening reaction [85]. Besides, RuS_2 is known to be the most active hydrodesulfurization catalyst [65]; so Ru-containing catalysts may exhibit higher activity in the sulfur feed as compared to Ir and Pd catalysts. Therefore, all bimetallic combinations of Pd, Ir and Ru were tested for the indan ring opening.

4.2.4.3. Ring opening of indan over Pd-Ir/γ-Al_2O_3 bimetallic catalysts

Among the synthesized bimetallic catalysts, ring opening of indan was first studied with Pd-Ir catalysts. There is a great hope that Pd(c)Ir(s) will show higher active and selective, and improved S-resistance (due to electrons transfer) than industrial catalyst.

Among the synthesized Pd-Ir/**γ-**Al_2O_3 catalysts, only Pd3Ir1_2, Pd1Ir1_2, Pd1Ir3_2, and Pd(c)Ir(s) were studied in the low-pressure ring opening of indan as representative catalyst batches. An exemplary reaction over Pd(c)Ir(s) catalyst is shown in Figure 4.22. As the catalyst stability was not studied and the conversion and selectivity variation within 150 - 250 minutes on stream was negligible (within the experimental error), the activities and selectivities are reported for this period of time on stream.

Activity. Figure 4.23 is the comparison of activities among bimetallic Pd-Ir catalysts with alloy (Pd3Ir1, Pd1Ir1, and Pd1Ir3) and core-shell (Pd(c)Ir(s)) structures, their monometallic forms (Pd1 and IrS21 sphere), and industrial Pt-Ir

catalysts. Pd(c)Ir(s) with mean diameter of 2.7 nm is the most active catalyst among all Pd-Ir bimetallic catalysts studied with the activity of 17×10^{-3} $g_{indan}/(g_{metal}\cdot min)$. The Pd(c)Ir(s) catalyst also shows 1.2 times higher activity than industrial Pt-Ir catalyst per weight of the active metals. Among the Pd-Ir alloy structures, at a higher Ir content, Pd1Ir3 with mean diameter of 2.3 nm is the most active nanocatalyst, whose activity is comparable with the industrial Pt-Ir catalyst. Figure 4.23 also shows a correlation between Pd content and indan conversion: the higher the Pd content in Pd-Ir nanosized alloy structure, the lower the nanocatalyst activity in indan ring opening, i.e., Pd-Ir nanosized catalyst with molar ratio 1/1 shows low catalytic activity ($2.4\times10^{-3}g_{indan}/(g_{metal}\cdot min)$); and Pd-Ir nanosized catalyst with molar ratio 3/1 is not active ($0.1\times10^{-3}g_{indan}/(g_{metal}\cdot min)$). Monometallic nanosized Ir catalyst is always the most active nanocatalyst in ring opening of indan.

Based on the comparison of catalytic activities, it can be concluded that:

- The activity of bimetallic nanosized Pd-Ir catalysts is in the order of:
  Ir sphere > Pd(c)Ir(s) > industrial Pt-Ir ≈ Pd1Ir3 >> Pd1Ir1 > Pd > Pd3Ir1;
- Nanosized Pd(c)Ir(s) catalyst shows the highest catalytic activity among Pd-Ir bimetallic nanocatalysts and the industrial Pt-Ir catalyst;
- Nanosized Pd3Ir1 catalyst is not active in ring opening of indan at current conditions due to high content of palladium, which is the least active metal.

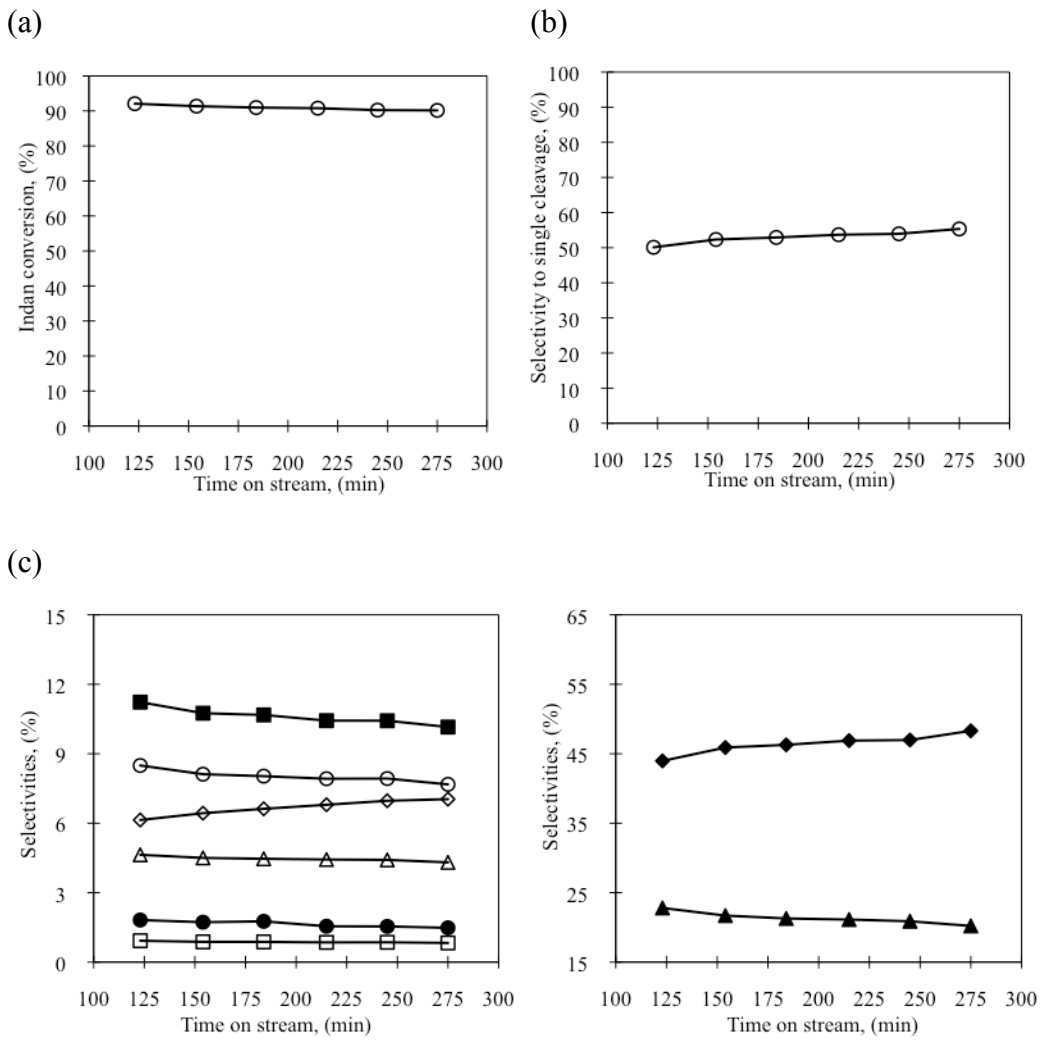

Figure 4.22. Low-pressure ring opening of indan over synthesized Pd(c)Ir(s) nanocatalyst (metal loading 1.2 mg): (a) indan conversion, (b) selectivity to single cleavage, and (c) selectivities to ring opening products. Reaction conditions: indan flow rate was 2.1×10^{-5} g/min, H_2/indan molar ratio was 11584, reaction temperature was 336 ^{o}C, and reaction pressure was 1 atm pressure.

Reaction products: Benzene (□), toluene (■), ethylbenzene (□), *o*-xylene (▲), *n*-propylbenzene (□), *2*-ethyltoluene (□), lights (○), others (●).

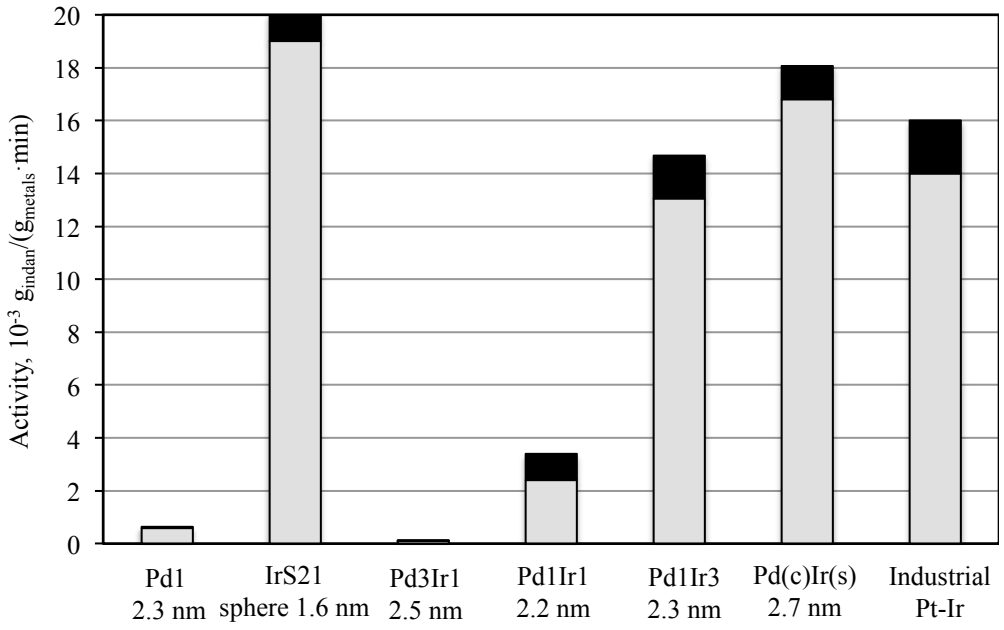

Figure 4.23. Comparison of catalytic activity among synthesized Pd-Ir bimetallic catalysts and industrial polydispersed Pt-Ir catalysts. Reaction conditions: indan flow rate was ranging from 2.2 to 3.6 $\times 10^{-5}$ g/min, H_2/Indan molar ratio was ranging from 6758 to 11058, reaction temperature was 336 ^{o}C, reaction pressure was 1 atm pressure, and metal loading was 1.2 mg for all catalysts.

RO selectivity. Comparisons of catalytic selectivities to single cleavage, *n*-propylbenzene, and lights among synthesized Pd-Ir bimetallic nanocatalysts and industrial Pt-Ir catalyst are shown in Table 4.10. Pd3Ir1 is not included because it is not active. It can be seen that all the bimetallic Pd-Ir nanocatalysts show better selectivities to single cleavage than that of industrial Pt-Ir catalyst (Table 4.10). Pd-Ir bimetallic nanocatalysts also improved CNs, for example, both Pd1Ir1 and Pd(c)Ir(s) show better selectivities to *n*-propylbenzene as compared to industrial Pt-Ir catalyst. Table 4.10 also shows that Pd-Ir bimetallic nanocatalysts allow less cracking than industrial catalyst. Both the high selectivities to single cleavage and the low selectivities to lights are due to the Ir content in the bimetallic Pd-Ir

catalysts, since monometallic Ir nanocatalysts always lead to high selectivity to selective ring opening products and less cracking.

Based on the comparison of RO selectivities with industrial Pt-Ir and monometallic nanosized Pd, Ir catalysts, it can be concluded that:

- From both selective RO selectivity and cetane number improvement points of view, nanosized Pd1Ir1, Pd1Ir3, and Pd(c)Ir(s) performed better than industrial Pt-Ir catalyst;
- Although Pd-Ir catalysts with alloy structures show high selectivities, Pd1Ir1 and Pd3Ir1 show very low catalytic activities, so only Pd1Ir3 and Pd(c)Ir(s) should be considered as valid alternatives to industrial catalyst.

Table 4.10. Comparison of selectivities to single cleavage, *n*-propylbenzene, and lights for indan ring opening over nanosized Pd-Ir bimetallic catalysts. Metal loading was 1.2 mg for Pd1, Pd1Ir1, Pd1Ir3, Pd(c)Ir(s), and industrial Pt-Ir catalysts; and 0.6 mg for Ir sphere catalyst. Data in brackets are one standard deviation.

Catalysts	Indan flow 10^{-5} g/min	Indan conversion %	Selectivities, (%)		
			Single cleavage	*n*-propylbenzene	Lights
Pd1	2.2	3	74 (4)	10.7 (0.6)	15 (2)
IrS21 sphere	2.5	45	75 (1)	11.7 (0.3)	4.3 (0.2)
Pd1Ir1	3.6 (0.7)	9 (4)	74 (1)	12 (3)	4.35 (0.07)
Pd1Ir3	2.65 (0.07)	63 (11)	64 (2)	6.0 (0.2)	5.2 (0.3)
Pd(c)Ir(s)	2.3 (0.2)	90 (0)	58 (6)	7.2 (0.8)	7 (1)
Industrial Pt-Ir	2.5 (0.1)	63 (6)	44 (4)	6.2 (0.4)	11 (1)

Ring opening of indan over bimetallic polydispersed Pt-Ir catalysts at 325 ^{o}C and atmospheric pressure was previously studied by Boutonnet et al. [3, 59]. Pt-Ir bimetallic catalysts were synthesized from a microemulsion system. TEM-EDX results showed large agglomerates with platinum lying on top of iridium plate-like clusters. Their catalytic results showed superior catalytic activities for Ir and Pt-Ir bimetallic catalysts as compared to Pt catalyst. Although Pt-Ir catalysts showed fast deactivation at atmospheric pressure, a better operating stability with no deactivation at high pressure (40 bar) was shown. They also found that indan conversion increased as the Ir content increased in the bimetallic catalysts. At similar reaction conditions, our PVP-stabilized Pd-Ir catalysts shows quite consistent results with their Pt-Ir catalysts.

Nanosized catalyst with core-shell structure that performs better than its monometallic forms has also been reported by Toshima et al.. In the hydrogenation of 1,3-cyclooctadiene to cyclooctene, Pd(c)Pt(s) with Pd/Pt molar ratio 4/1 was the most active catalyst, twice as active as a typical colloidal Pd catalyst [31].

4.2.4.4. Ring opening of indan over Ir-Ru/γ-Al_2O_3 bimetallic catalysts

As the optimal combination and composition of the bimetallic nanoparticles are not known yet, the RO of indan was then studied with Ir-Ru bimetallic catalysts, as Ir will ensure high activity, and Ru will result in increased S-resistant in the present of sulfur compound later.

Among the synthesized nanosized Ir-Ru/γ-Al_2O_3 catalysts, only Ir3Ru1_1, Ir1Ru1_1, and Ir1Ru3_1 were studied in low-pressure ring opening of indan as representative catalyst batches.

Activity. Figure 4.24 shows the comparison of the activities for bimetallic Ir-Ru nanocatalysts with alloy structures (Ir3Ru1, Ir1Ru1, and Ir1Ru3), their monometallic forms (IrS21 sphere and Ru1), and industrial Pt-Ir catalysts. Although both nanosized monometallic Ir and Ru show high catalytic activities, the combinations of these two metals are less active (Fig. 4.24). Only at higher Ir content (Ir/Ru molar ratio = 3/1), catalytic activity (10.4×10^{-3} $g_{indan}/(g_{metals}\cdot min)$) is comparable with 2.3 nm Ru1 catalysts (10.5×10^{-3} $g_{indan}/(g_{metals}\cdot min)$). Both Ir1Ru1 and Ir1Ru3 show low activities in the RO of indan. The observed correlation between Ir content and indan conversion shows that the higher the Ir content in the alloy structure, the higher the activity of the bimetallic catalyst in ring opening of indan.

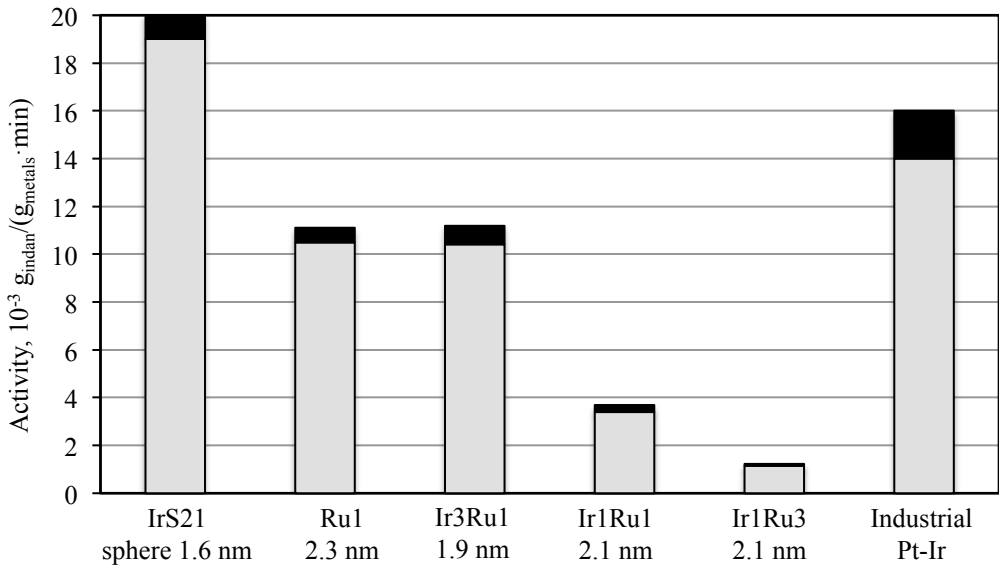

Figure 4.24. Comparison of catalytic activity among synthesized Ir-Ru bimetallic nanocatalysts and industrial polydispersed Pt-Ir catalysts. Reaction conditions: indan flow rate was ranging from 2.5 to 3.0 $\times10^{-5}$ g/min, H_2/Indan molar ratio was ranging from 8109 to 9731, reaction temperature was 336 ^{o}C, reaction pressure was 1 atm pressure, and metal loading was 1.2 mg for all catalysts.

Based on the comparison of catalytic activities, it can be concluded that:

- The activity of bimetallic Ir-Ru nanocatalysts is in the order of:
  Ir sphere > industrial Pt-Ir > Ru1 ≈ Ir3Ru1 > Ir1Ru1 > Ir1Ru3;
- Ir-Ru catalysts show antagonism in indan ring opening reactions.

RO selectivity. Comparisons of catalytic selectivities to single cleavage, *n*-propylbenzene, and lights among synthesized Ir-Ru bimetallic nanocatalysts and industrial Pt-Ir catalyst are shown in Table 4.11. Only Ir3Ru1 catalyst allows better selectivity to single cleavage (70%) than industrial Pt-Ir catalyst. However, all three alloy-nanocatalysts lead to higher single cleavage than that of monometallic Ru nanocatalyst (Table 4.11). This improvement is also due to the presence of Ir metal, since it has the highest selectivity in ring opening of indan as discussed above. Selectivities to *n*-propylbenzene for catalysts with Ir/Ru molar ratios of 1/1 (1.7%) and 1/3 (1.8%) are very low. However, as Ir content increases, Ir3Ru1 shows comparable selectivity to *n*-propylbenzene as industrial Pt-Ir catalyst (Table 4.11). Table 4.11 also shows that Ir1Ru1 and Ir1Ru3 nanocatalysts lead to excessive cracking similar to Ru monometallic nanocatalyst. Only at low Ru content, Ir3Ru1 catalyst displayed less cracking as compared to industrial Pt-Ir catalyst. Similar result has been reported by Marecot's group. In their study, ring opening of methylcyclopentane favored the production of cracking products as Ru added onto a parent Pt/Al_2O_3 catalyst by a surface redox reaction [52].

Based on the comparisons of RO selectivities with industrial Pt-Ir and monometallic Ru, Ir catalysts, it can be concluded that:

- Although Ir3Ru1 shows comparable selectivity to the industrial catalyst, it is less active than the industrial catalyst;

- Ir1Ru1 and Ir1Ru3 nanocatalysts leads to low selectivities and excessive cracking, thus they are not suitable for selective ring opening.

Table 4.11. Comparison of selectivities to single cleavage, *n*-propylbenzene, and lights for indan ring opening over nanosized Ir-Ru bimetallic nanocatalysts. Metal loading was 1.2 mg for Ru1, Ir3Ru1, Ir1Ru1, Ir1Ru3, and industrial Pt-Ir catalysts; and 0.6 mg for IrS21 sphere catalyst. Data in brackets are one standard deviation.

Catalysts	Indan flow 10^{-5} g/min	Indan conversion %	Selectivities, (%)		
			Single cleavage	*n*-propylbenzene	Lights
IrS21 Sphere	2.5	45	75 (1)	11.7 (0.3)	4.3 (0.2)
Ru1	2.8	45	9.9 (0.2)	0.89 (0.01)	22.7 (0.3)
Ir3Ru1	3 (1)	35 - 65	70 (4)	5.9 (0.2)	5.1 (0.9)
Ir1Ru1	2.8	14	28.1 (0.1)	1.68 (0.03)	16.4 (0.2)
Ir1Ru3	3 (1)	4 (1)	36 (4)	1.8 (0.7)	18 (2)
Industrial Pt-Ir	2.5 (0.1)	63 (6)	44 (4)	6.2 (0.4)	11 (1)

4.2.4.5. Ring opening of indan over Pd-Ru/γ-Al_2O_3 bimetallic catalysts

Although monometallic Pd and Ru did not show superior catalytic performance as compared to industrial catalyst, they are valuable candidates for bimetallic catalysts, as synergism could be achieved by electrons transfer. Among the synthesized Pd-Ru/γ-Al_2O_3 catalysts, only Pd3Ru1_2, Pd1Ru1_1, and Pd1Ru3_1 were studied in low-pressure ring opening of indan as representative catalyst batches.

Activity. Figure 4.25 is the comparison of activities among bimetallic Pd-Ru nanocatalysts with alloy structures (Pd3Ru1, Pd1Ru1, and Pd1Ru3), their monometallic forms (Pd1 sphere and Ru1), and industrial Pt-Ir catalysts. Figure 4.25 shows that Pd3Ru1 and Pd1Ru1 have very low activities in the RO of indan. As Ru content increases in the bimetallic alloy structure, Pd1Ru3 converted 2.4×10^{-3} gram of indan per active metal per minute, which is higher than the activity of Pd monometallic nanocatalyst, but still lower than nanosized Ru monometallic and industrial catalysts (Fig. 4.25).

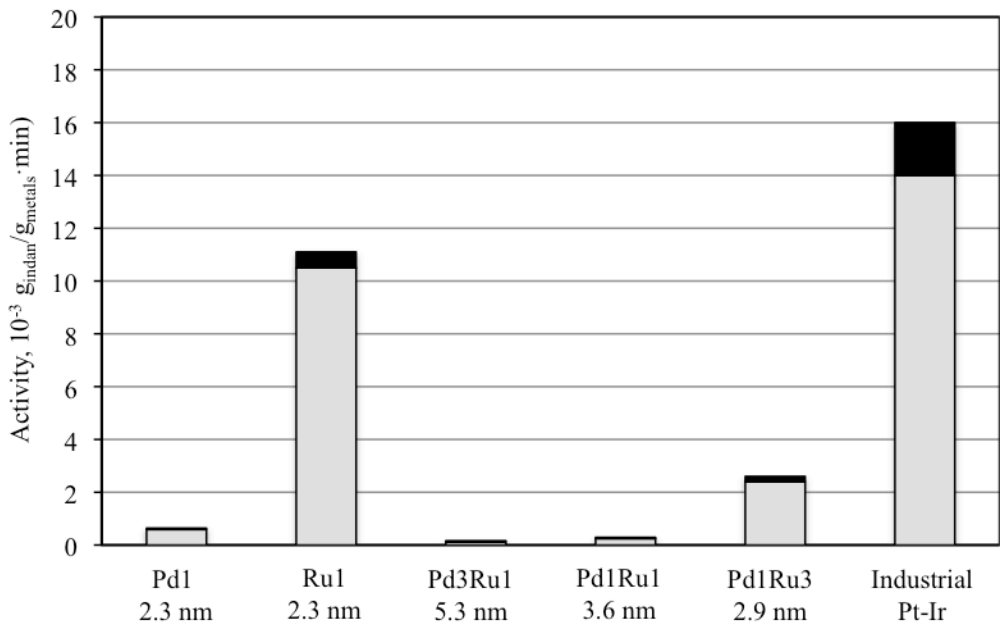

Figure 4.25. Comparison of catalytic activity among synthesized Pd-Ru bimetallic nanocatalysts and industrial polydispersed Pt-Ir catalysts. Reaction conditions: indan flow rate was ranging from 2.2 to 4.6 $\times10^{-5}$ g/min, H_2/Indan molar ratio was ranging from 5289 to 11058, reaction temperature was 336 ^{o}C, reaction pressure was 1 atm pressure, metal loading was 1.2 mg for all catalysts.

Based on the comparison of catalytic activities, it can be concluded that:

- The activity of bimetallic Pd-Ru nanocatalysts is in the order of: industrial Pt-Ir > Ru1 >> Pd1Ru3 > Pd1> Pd1Ru1 ≈ Pd3Ru1;
- Pd -Ru catalysts show antagonism in indan ring opening reactions.

RO selectivity. Comparisons of catalytic selectivities to single cleavage, *n*-propylbenzene, and lights among synthesized Pd-Ru bimetallic nanocatalysts and industrial Pt-Ir catalyst are shown in Table 4.12. All three Pd-Ru nanosized alloy catalysts show very low selectivities to ring opening products as compared to Pd1 and industrial catalysts. The ring opening of indan results in high cracking (38% of lights) over 5.3 nm Pd3Ru1. This is consistent with the previous result obtained on monometallic Pd nanocatalysts, when indan ring opening became non-selective over 4.4 nm Pd catalyst as compared to 2.3 nm Pd catalyst. Table 4.12 also shows that Pd1Ru3 has lower selectivities to single cleavage (6%) and to *n*-propylbenzene (< 1%), and higher cracking than those of Pd1Ru1. This is because Pd1Ru3 has higher content of Ru metal than Pd1Ru1 does, thus leading to lower selectivities and excessive cracking.

Based on the comparison of RO selectivities with industrial Pt-Ir and monometallic Pd, Ru nanocatalysts, it can be concluded that:

- None of the Pd-Ru nanocatalysts with three different alloy structures are suitable for selective ring opening of indan due to their low activities, low selectivities, and excessive cracking.

Table 4.12. Comparison of selectivities to single cleavage, *n*-propylbenzene, and lights for indan ring opening over nanosized Ir-Ru bimetallic nanocatalysts. Metal loading was 1.2 mg for Pd1, Ru1, Pd1Ru3, and industrial Pt-Ir catalysts. Data in brackets are one standard deviation.

Catalysts	Indan flow 10^{-5} g/min	Indan conversion %	Selectivities, (%)		
			Single cleavage	*n*-propylbenzene	Lights
Pd1	2.2	3	74 (4)	10.7 (0.6)	15 (2)
Ru1	2.8	45	9.9 (0.2)	0.89 (0.01)	22.7 (0.3)
Pd3Ru1	2.8 (0.3)	0.5 (0)	0 (0)	0 (0)	38 (4)
Pd1Ru1	4.6	0.5	18 (3)	3.5 (0.5)	9 (2)
Pd1Ru3	3.6	7	5.9 (0.3)	0.73 (0.06)	63 (2)
Industrial Pt-Ir	2.5 (0.1)	63 (6)	44 (4)	6.2 (0.4)	11 (1)

Often, the addition of a second metal does not simply "add" its activity but leads to synergism. For example, Ru-Pt bimetallic catalyst in the RO of methylcyclopentane showed synergism factor (ratio of actual conversion to the sum of conversions for separate metals) close to four, whereas synergism factors were approximately 1 for other Pt- based bimetallic catalysts (Ir-Pt, Rh-Pt, and Pd-Pt) [85]. Moreover, Thomas's group has reported that Pd6Ru6 bimetallic catalyst was more active, selective, and resistant to sulfur poisoning in single-step hydrogenation [86]. However, ring opening of indan over Pd-Ru bimetallic nanocatalysts does not follow the catalytic results obtained in RO of methylcyclopentane or single-step hydrogenation, i.e., nanosized Pd-Ru catalysts show much lower activities than Ru monometallic nanocatalyst; and much lower ring opening selectivities than Pd monometallic nanocatalyst.

5. Conclusions

- Monometallic PVP-stabilized Pd, Ir, and Ru colloids of various defined sizes in the < 10 nanometer range were synthesized and deposited onto a gamma-alumina support.
- Nanosized bimetallic colloids of Pd-Ir, Ir-Ru, and Pd-Ru were synthesized either via simultaneous reduction in the presence of PVP or via hydrogen-sacrificial technology, providing presumably alloy or core-shell structures, respectively.
- Benzocyclopentane (indan) ring opening was studied under hydrogen atmospheric pressure at 609 K with synthesized nanocatalysts; and the obtained catalytic results were compared with an industrial polydispersed Pt-Ir catalyst.
- Pd nanocatalysts displayed the lowest activity in the RO reaction; the characteristic feature of the Ru nanocatalysts is the highest *o*-xylene production among the catalysts studied.
- Monometallic Ir nanocatalyst (sphere 1.6 nm) and bimetallic Pd-Ir nanocatalyst (2.7 nm) with presumable core-shell structure showed superior activity and selectivity as compared to the industrial Pt-Ir catalyst.
- In future studies, the bimetallic nanoparticle structures (alloy or core-shell) should be confirmed. Their catalytic performances (activity, selectivity and stability) should be studied for ultra-deep desulfurization.

6. References

[1] C. Song and A.D. Schmitz, *Energy & Fuels*, 11 (1997) 656.

[2] R.M. Navarro, B. Pawelec, J.M. Trejo, R. Mariscal, and J.L.G. Fierro, *J. Catal.* 189 (2000) 184.

[3] U. Nylen, L. Sassu, S. Melis, S. Jaras, and M. Boutonnet, *Appl. Catal. A* 299 (2006) 1.

[4] B. Coq and F. Figueras, *J. Mol. Catal. A Chem*. 173 (2001) 117.

[5] *Metal Nanoclusters in Catalysis and Materials Science: the Issue of Size Control*, Eds. B. Corain, G. Schmid, and N. Toshima, Elsevier B. V. (2008)

[6] R. Narayanan and M.A. El-Sayed, *Langmuir* 21 (2005) 2027.

[7] N. Semagina and L. Kiwi-Minsker, *Catal. Rev.* 50 (2008) 1.

[8] D. Astruc, F. Lu, and J.R. Aranzaes, *Angew. Chem. Int. Ed.* 44 (2005) 7852.

[9] *Chemical Bonds and Bond Energy*, R.T. Sanderson, New York, Academic Press (1976).

[10] Y. Borodko, S.M. Humphrey, T.D. Tilley, H. Frei, and G.A. Somorjai, *J. Phys. Chem. C* 111 (2007) 6288.

[11] T. Teranishi and M. Miyake, *Chem. Mater.* 10 (1998) 594.

[12] Y. Shiraishi, K. Hirakawa, and N. Toshima, *Kobunshi Ronbun-shu* 57 (2000) 346.

[13] M, Ganesan, R.G. Freemantle, and S.O. Obare, *Chem. Mater.* 19 (2007) 3464.

[14] N. Toshima, Y. Shiraishi, T. Teranishi, M. Miyake, T. Tominage, H. Watanabe, W. Brijoux, H. Bonnemann, and G. Schmid, *Appl. Organometal. Chem.* 15 (2001) 178.

[15] G. Schmid, R. Boese, R. Pfeil, F. Bandermann, S. Meyer, G.H.M. Calis, and J.A.W. van der Velden, *Chem. Ber.* 114 (1981) 3634.

[16] R. Franke, J. Rothe, J. Pollmann, J. Hormes, H. Bnnemann, W. Brijoux, and Th. Hindenburg, *J. Am. Chem. Soc.* 118 (1996) 12090.

[17] H. Hirai, N. Yakura, Y. Seta, and S. Hodoshima, *React. Funct. Polym.* 37 (1998) 121.

[18] R.M. Rioux, H. Song, J.D. Hoefelmeyer, P. Yang, and G.A. Somorjai, *J. Phys. Chem. B* 109 (2005) 2192.

[19] J. Turkevich, *Gold Bull*. 18 (1985) 3.

[20] C.B. Murray, C.R. Kagan, and M.G. Bawendi, *Annu. Rev. Mater. Sci.* 30 (2000) 545.

[21] Y. Xiong, H. Cai, B.J. Wiley, J. Wang, M.J. Kim, and Y. Xia, *J. Am. Chem. Soc*. 129 (2007) 3665.

[22] R.V. Hardeveld and F. Hartog, *Surf. Sci*. 15 (1969) 189.

[23] Y. Wang, M. Du, J. Xu, P. Yang, and Y. Du, *J. Disp. Sci. Tech.* 29 (2008) 891.

[24] H. Choo, B. He, K.Y. Liew, H. Liu, and J. Li, *J. Mol. Catal. A Chem.* 244 (2006) 217.

[25] J.M. Petroski, Z.L. Wang, T.C. Green, and M.A. El-Sayed, *J. Phys. Chem. B* 102 (1998) 3316.

[26] B. Wiley, T. Herricks, Y. Sun, and Y. Xia, *Nano. Lett.* 4 (2004) 1733.

[27] T. Teranishi, R. Kurita, and M. Miyake, *J. Inorg. Organomet. Polym.* 10 (2000) 145.

[28] *Catalysis by metals and alloys*, V. Ponec and G.C. Bond, Elsevier, Amsterdam, 1995.

[29] J.C. Fuggle, F.U. Hillebrecht, R. Zeller, Z. Zolnierek, P.A. Bennett, and Ch. Freiburg, *Phys. Rev. B* 27 (1982) 2145.

[30] R.L. Moss, D. Pone, and H.R. Gibbens, *J. Catal.* 55 (1978) 100.

[31] N. Toshima, T. Yonezawa, and K. Kushihashi, *J. Chem. Soc. Faraday Trans.* 89 (1993) 2537.

[32] N. Toshima, *Pure Appl. Chem.* 72 (2002) 317.

[33] J. Yang, J.Y. Lee, L.X. Chen, and H.P. Too, *J. Phys. Chem. B* 109 (2005) 5468.

[34] C.X. Kan, W.P. Cai, and C.C. Li, L.D. Zhang, H. Hofmeister, *J. Phys. D* 36 (2003) 1609.

[35] M. Harada, K. Asakura, and N. Toshima, *Jpn. J. Appl. Phys*. 32 (1993) 451.
[36] B. Zhao and N. Toshima, *Chem. Express* 5 (1990) 721.
[37] C. Pan, F. Dassenoy, M.J. Casanove, K. Philippot, C. Amiens, P. Leante, A. Mosset, and B. Chaudret, *J. Phys. Chem. B* 103 (1999) 10098.
[38] P. Dash, N.A. Dehm, and R.W.J. Scott, *J. Mol. Catal. A* 286 (2008) 114.
[39] Y. Wang and N. Toshima, *J. Phys. Chem. B* 101 (1997) 5301.
[40] K. Vinodgopal, Y.H. He, M. Ashokkumar, and F. Grieser, *J. Phys. Chem. B* 110 (2006) 3849.
[41] *LCO Upgrading: A novel approach for greater added value and improved returns*, V.P. Thakkar, S.F. Abdo, V.A. Gembicki, and F.M. Gehee, UOP LLC (2005).
[42] P. Courty and J.F. Gruson, *Oil and Gas Science and Technology – Rev. IFP*, 56 (2001) 515.
[43] G.B. McVicker, M. Daage, M.S. Touvelle, C.W. Hudson, D.P. Klein, W.C. Baird, Jr., B.R. Cook, J.G. Chen, S. Hantzer, D.E.W. Vaughan, E.S. Ellis, and O.C. Feeley, *J. Catal.* 210 (2002) 137.
[44] H. Du, C. Fairbridge, H. Yang, and Z. Ring, *Appl. Catal. A* 294 (2005) 1.
[45] Z. Paal and P. Tetenyi, *Nature* 267 (1977) 19.
[46] D. Kubicka, N. Kumar, P.M-Arvela, M. Tiitta, V. Niemi, T. Salmi, and D.Y. Murzin, *J. Catal.* 222 (2004) 65.
[47] C. Marcilly, *J. Catal.* 216 (2003) 47.
[48] F.G. Gault, *Adv. Catal.* 30 (1981) 1.
[49] K. Hayek, R. Kramer, and Z. Paal, *Appl. Catal. A* 162 (1997) 1.
[50] D. Kubicka, N. Kumar, P.M-Arvela, M. Tiitta, V. Niemi, H. Karhu, T. Salmi, and D.Y. Murzin, *J. Catal.* 227 (2004) 313.
[51] P.T. Do, W.E. Alvarez, and D.E. Resasco, *J. Catal.* 238 (2006) 477.
[52] P. Samoila, M. Boutzeloit, C. Especel, F. Epron, and P. Marecot, *Appl. Catal. A* 369 (2009) 104.

[53] R.L. Moss, *J. Catal.* 55 (1978) 100.
[54] J-M. Dartigues, A. Chambellan, and F.G. Gault, *J. Am. Chem. Soc.* 98 (1976) 856.
[55] J.P. Boitiaux, J. Cosyns, and S. Vasudevan, *Appl. Catal.* 6 (1983) 41.
[56] J.N. Kuhn, W. Huang, C-K. Tsung, Y. Zhang, and G.A. Somorjai, *J. Am. Chem. Soc.* 130 (2008) 14026.
[57] C.G. Walter, B. Coq, F. Figueras, and M. Boulet, *Appl. Catal. A* 133 (1995) 95.
[58] L.B. Galperin, J.C. Bricker, and J.R. Holmgren, *Appl. Catal. A* 239 (2003) 297.
[59] U. Nylen, J.F. Delgado, S. Jaras, and M. Boutonnet, *Appl. Catal. A* 262 (2004) 189.
[60] Y. Li, E. Boone, and M.A. El-Sayed, *Langmuir* 18 (2002) 4921.
[61] F. Fievet, J.P. Lagier, and B. Blin, *Solid State Ion*. 32/33 (1989) 198.
[62] Y. Chem, K.Y. Liew, and J. Li, *Mater. Lett.* 62 (2008) 1018.
[63] X. Yan, H. Liu, and K.Y. Liew, *J. Mater. Chem.* 11 (2001) 3387.
[64] X. Zuo, H. Liu, and C. Yue, *J. Mol. Catal. A Chem.* 147 (1999) 63.
[65] P. Castillo-Villalon, J. Ramirez, and F. Mauge, *J. Catal.* 260 (2008) 65.
[66] Y. Shiraishi, D. Ikenaga, and N. Toshima, *Aust. J. Chem.* 56 (2003) 1025.
[67] A. Molnar, A. Sarkany, M. Varga, J. Mol. Catal. A 173 (2001) 185.
[68] R.M. Rioux, H. Song, M. Grass, S. Habas, K. Niesz, J.D. Hoefelmeyer, P. Yang, and G.A. Somorjai, *Top. Catal.* 39 (2006) 3.
[69] M.M. Koebel, L.C. Jones, and G.A. Somorjai, *J. Nanopart. Res*. 10 (2008) 1063.
[70] P. Santiago-Torres, M.Sc. Thesis, U. Puerto Rico (2007).
[71] K.M.K. Yu, P. Meric, and S.C. Tsang, *Catal. Today* 114 (2006) 428.
[72] G.B. Khomutov, *Adv. Coll. Interface Sci.* 111 (2004) 79.
[73] *Elements of chemical reaction engineering* (4th edition), H.S. Fogler, Pearson international edition (2006).
[74] F.W. Dynys and J.W. Halloran, *J. Am. Ceram. Soc.* 65 (1982) 9.

[75] *Coulson and Richardson's Chemical Engineering - Chemical and Biochemical Reactors and Process Control,* J.F. Richardson and D.G. Peacock, Volume 3 (3rd Edition), Elsevier (1994). http://knovel.com.login.ezproxy.library.ualberta.ca/web/portal/browse/display?_EXT_KNOVEL_DISPLAY_bookid=2998&VerticalID=0
[76] *Yaws' Handbook of Thermodynamic and Physical Properties of Chemical Compounds,* C.L. Yaws, Knovel (2003). http://knovel.com/web/portal/browse/display?_EXT_KNOVEL_DISPLAY_bookid=667&VerticalID=0
[77] A.B. Gaspar and L.C. Dieguez, *Appl. Catal. A* 201 (2000) 241.
[78] J.L.C. - Dominguez and R.V.-Ibarra, *Energy & Fuels* 21 (2007) 1122.
[79] O.V. Masloboishchikova, T.V. Vasina, E.G.K.-Sergeeva, L.M. Kustov, and P. Zeuthen, *Russ. Chem. Bull.* 51 (2002) 249.
[80] O.V. Masloboishchikova, E.G.K.-Sergeeva, V.I. Bogdan, T.V. Vasina, and L.M. Kustov, *Russ. Chem. Bull.* 55 (2006) 656.
[81] W.C. Baird Jr., J.G. Chen, and G.B. McVicker, US Patent 6, 623, 626 (2003).
[82] W.C. Baird Jr., D.P. Klein, M.S. Touvelle, J.G. Chen, and G.B. McVicker, US Patent 6, 586, 650 (2003).
[83] W.C. Baird Jr., J.G. Chen, and G.B. McVicker, US Patent 6, 623, 625 (2003).
[84] W.C. Baird Jr., D.P. Klein, M.S. Touvelle, and J.G. Chen, US Patent 6, 589, 416 (2003).
[85] Patent WO 2007/041605 (2007)
[86] J.M. Thomas, B.F.G. Johnson, R. Raja, G. Sankar, and P.A. Midgley, *Acc. Chem. Res.* 36 (2003) 20.

Appendix A: TEM images and corresponding histograms for repeated nanoparticles.

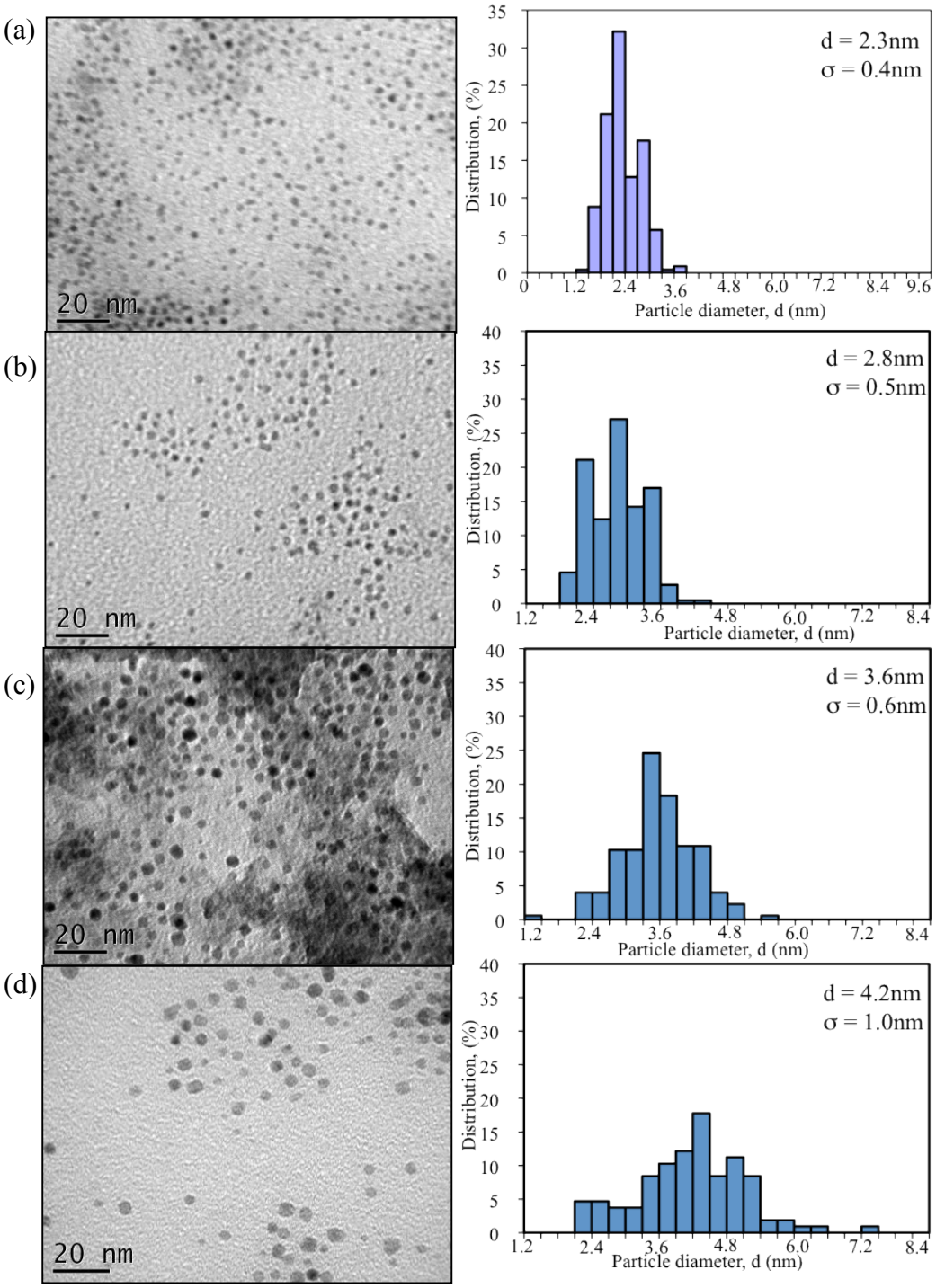

Figure A1. TEM photographs of repeated (a) PdS1, (b) PdS2, (c) PdS3, and (d) PdS4 and corresponding size distribution histograms.

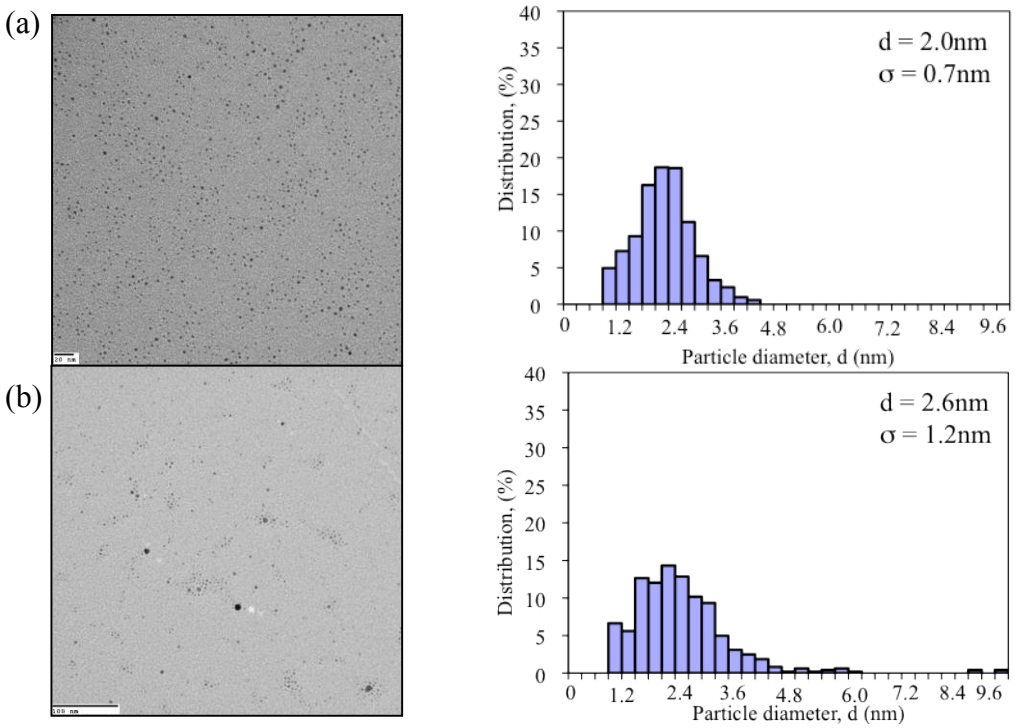

Figure A2. TEM photographs of repeated (a) Pd3 and (b) Pd4 and corresponding size distribution histograms.

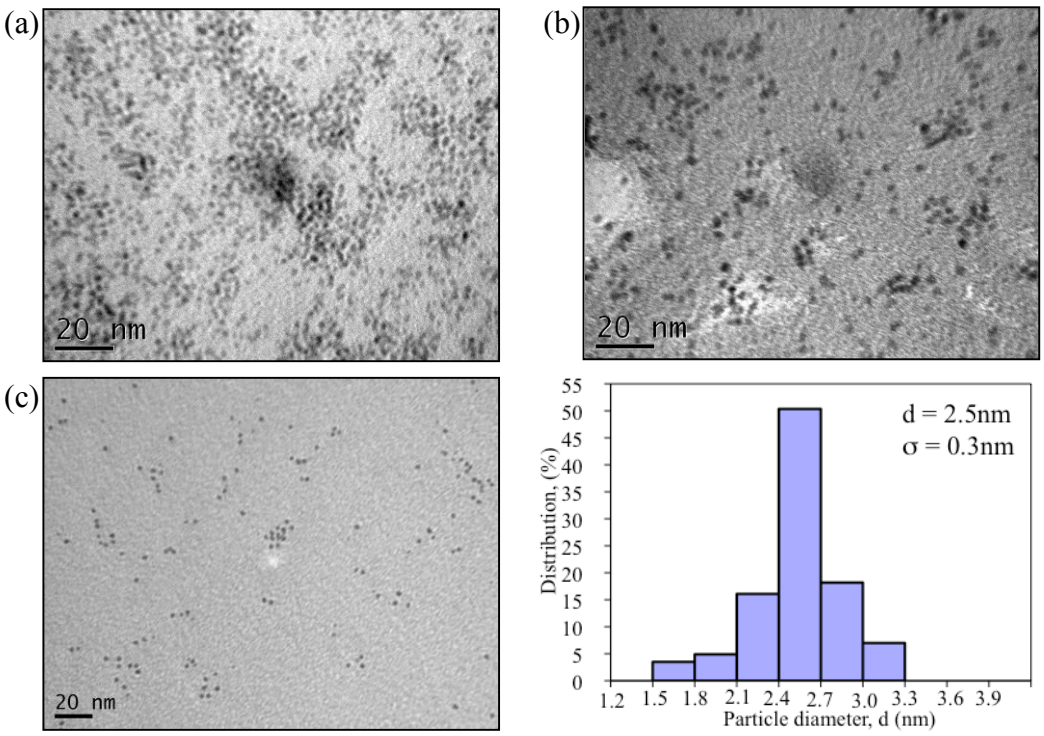

Figure A3. TEM photographs of repeated (a) Ru1, (b) RuS3, (c) Ru4 (PVP/Ru = 5/1) and corresponding size distribution histogram for Ru4.

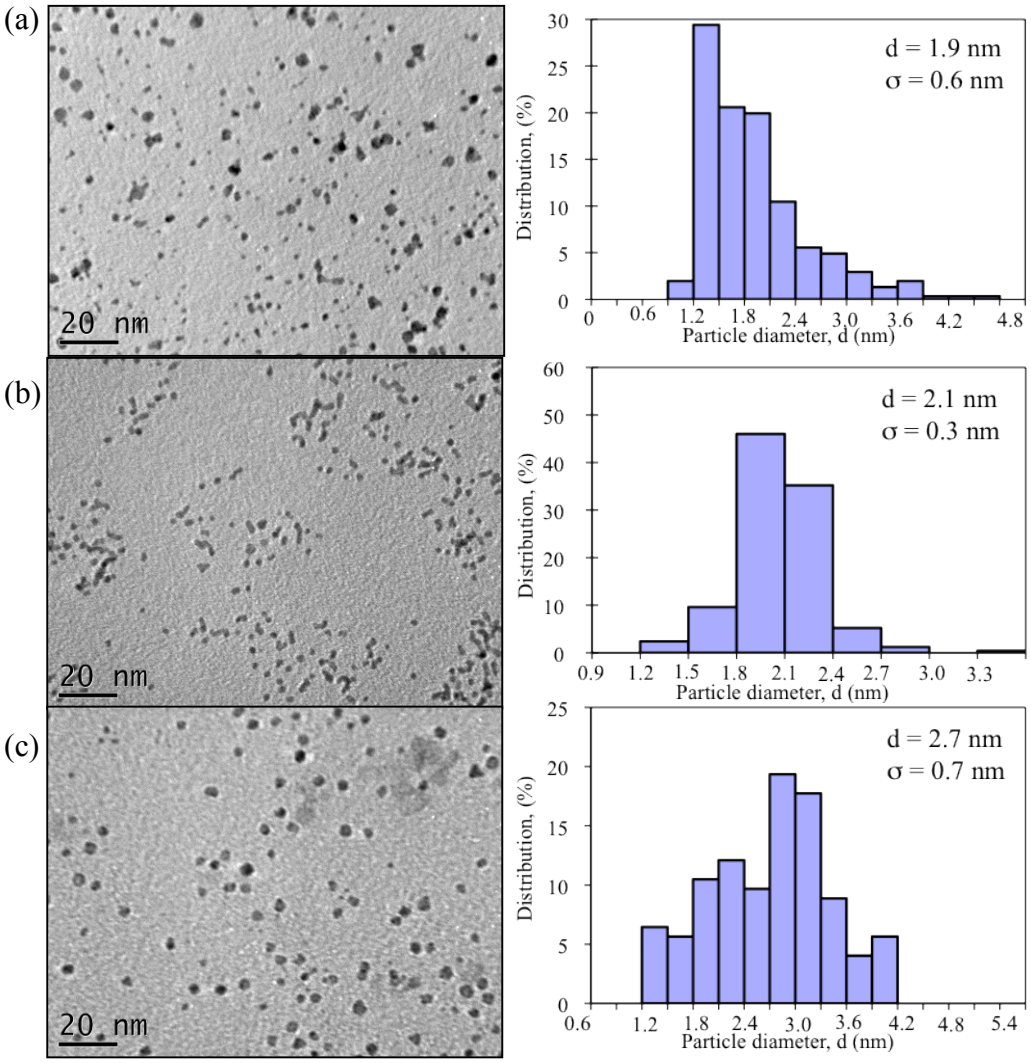

Figure A4. TEM photographs of repeated (a) Pd1Ir3_2, (b) Ir1Ru1_1, and (c) Pd(c)Ir(s) and corresponding size distribution histograms.

Appendix B: Summary of low-pressure ring opening of indan

Table B1. Summary of catalytic results for low-pressure ring opening of indan. Reaction temperature was 336 ^{o}C and reaction pressure was 1 atm pressure. 8 (or 6) data points were obtained at 150, 180, 210 (and 240 minutes) of time on stream with a duplicate experiment. Within the indicated times on stream the catalysts did not show noticeable deactivation.

Catalyst	Metal loading in the reactor, mg	Indan flow, 10^{-5} g/min	Conversion %	Activity, 10^{-3} $g_{indan}/(g_{metal} \cdot min)$	Selectivity, %								
					Benzene	Toluene	Ethylbenzene	*o*-xylene	*n*-propylbenzene	*2*-ethyltoluene	Lights	Others	Single Cleavage
industrial Pt-Ir	1.2	2.4	70	14 (2)	2.3 (0.1)	16.8 (0.2)	3.86 (0.02)	23.7 (0.1)	5.9 (0.1)	34.0 (0.3)	9.3 (0.2)	1.1 (0.1)	39.4 (0.5)
industrial Pt-Ir	1.2	2.6	60	15 (1)	1.4 (0.3)	12 (2)	3.8 (0.1)	21 (1)	6.6 (0.4)	41 (2)	11 (1)	3 (1)	48 (3)
industrial Pt-Ir	0.12	3.1	5	14.8 (0.7)	1.06 (0.04)	6.7 (0.2)	3.30 (0.05)	14.1 (0.2)	10.0 (0.2)	51.8 (0.7)	6.3 (0.4)	6.8 (0.7)	61.8 (0.9)
industrial Pt-Ir	1.2	2.5	60	12.8 (0.3)	1.86 (0.03)	15.3 (0.3)	3.54 (0.01)	22.0 (0.2)	6.1 (0.1)	37.5 (0.6)	11.7 (0.2)	2.1 (0.1)	44 (1)
industrial Pt-Ir	0.29	2.8	23	23 (1)	1.57 (0.06)	11.9 (0.3)	3.53 (0.05)	19.8 (0.2)	7.9 (0.1)	43.8 (0.5)	9.7 (0.9)	1.8 (0.4)	51.7 (0.5)
industrial Pt-Ir	0.9	2.3	67	15 (4)	1.9 (0.1)	15.2 (0.3)	3.52 (0.01)	22.8 (0.3)	5.9 (0.2)	37.3 (0.6)	12.2 (0.3)	1.2 (0.2)	43.2 (0.8)
Pd1	1.2	2.2	3	0.59 (0.05)	1.2 (0.1)	0	2.8 (0.2)	2.2 (0.1)	10.7 (0.6)	63 (3)	15 (2)	7.8 (0.4)	74 (4)

PdS1	1.2	4	0.5	0.21 (0.02)	5.1 (0.1)	2.8 (0.3)	1.5 (0.2)	0	0	0.6 (0.3)	21 (2)	69 (3)	0.6 (0.2)
PdS1	1.2	3.4	0.5	0.165 (0.002)	6 (1)	0.1 (0.2)	3.3 (0.5)	2.3 (0.4)	0.1 (0.1)	0	15 (1)	72 (3)	0.1 (0.1)
PdS4	1.2	3.3	0.2	0.04 (0.05)	12 (2)	0	10 (1)	0	0	0.2 (0.3)	9 (2)	68 (4)	0.2 (0.3)
PdS4	1.2	3.2	0.3	0.1 (0.3)	6 (2)	0	4 (1)	0	0	0	2 (1)	89 (3)	0
IrS11 worm	1.2	2.3	25	5.1 (0.2)	0.19 (0.01)	1.4 (0.1)	0.56 (0.03)	3.2 (0.1)	12.8 (0.2)	77.7 (0.4)	2.32 (0.02)	2.32 (0.02)	90.5 (0.5)
IrS21 sphere	0.6	2.5	45	19 (1)	0.46 (0.04)	4.6 (0.3)	2.3 (0.1)	12 (1)	11.7 (0.3)	64 (1)	4.3 (0.2)	1.4 (0.5)	75 (1)
IrS21 sphere	1.2	2.2	100	19 (1)	1.57 (0.04)	21.9 (0.4)	4.2 (0.1)	44.4 (0.5)	0.53 (0.05)	10.4 (0.6)	16.2 (0.3)	0.81 (0.03)	11 (1)
Ru1	0.97	2.8	45	10.5 (0.6)	3.7 (0.1)	19.2 (0.1)	3.6 (0.1)	37.5 (0.2)	0.89 (0.01)	8.9 (0.2)	22.7 (0.3)	3.4 (0.1)	9.9 (0.2)
Ru2	1.2	11	2	2.1 (0.3)	1.1 (0.1)	0	1.0 (0.3)	11 (2)	0	12 (2)	1.8 (0.7)	74 (6)	12 (2)
Ru6	1.2	4	0.3	0.12 (0.03)	2 (2)	0	3 (1)	5.9 (0.1)	0	8.9 (0.1)	24 (1)	58 (3)	8.9 (0.1)
Ru6	1.2	2.9	0.3	0.081 (0.006)	0	0	2.4 (0.5)	0	0	0	19 (1)	79 (3)	0
Rus2	1.2	8.7	9	6.4 (0.2)	1.1 (0.1)	0.4 (0.5)	0	18 (1)	0	47 (3)	5.2 (0.7)	28 (5)	47 (3)
Pd3Ir1_2	1.2	2.6	0.5	0.10 (0.01)	4.5 (0.5)	0	3.6 (0.1)	0	0.3 (0.5)	9 (2)	17 (4)	65 (6)	9 (2)
Pd3Ir1_2	1.2	3.1	0.5	0.11 (0.01)	4.9 (0.2)	0	4.6 (0.4)	0	0	15.7 (1.2)	9.8 (1.4)	65 (2)	16 (1)
Pd1Ir1_1	1.2	4.1	6	1.7 (0.5)	0.5 (0.1)	1.16 (0.01)	7.2 (0.7)	0.5 (0.2)	10.1 (0.7)	65.8 (1.5)	4.3 (0.2)	10.3 (1.4)	73 (2)

Pd1Ir1_1	1.2	3.1	11	3.1 (0.3)	0.30 (0.03)	1.3 (0.2)	6.5 (0.3)	1.6 (0.1)	13.8 (0.8)	68.5 (0.9)	4.4 (0.1)	3.6 (1.3)	75 (1)
Pd1Ir3_2	1.2	2.7	55	11.9 (0.7)	0.254 (0.003)	3.9 (0.1)	2.13 (0.05)	22.7 (0.8)	5.8 (0.2)	59.2 (0.6)	5.0 (0.1)	0.9 (0.3)	65.1 (0.8)
Pd1Ir3_2	1.2	2.6	70	14.2 (0.7)	0.29 (0.02)	4.8 (0.1)	2.52 (0.06)	24.4 (0.8)	6.1 (0.2)	55.7 (0.9)	5.4 (0.1)	0.7 (0.1)	61.9 (1.2)
Pd(c)Ir(s)	1.2	2.1	90	15.9 (0.7)	0.87 (0.01)	10.6 (0.2)	4.47 (0.04)	21.4 (0.3)	6.6 (0.2)	46.4 (0.5)	8.1 (0.1)	1.7 (0.1)	53.0 (0.7)
Pd(c)Ir(s)	1.2	2.4	90	17.7 (0.1)	0.71 (0.02)	8.1 (0.3)	3.8 (0.1)	17.4 (0.6)	7.8 (0.3)	54 (1)	6.7 (0.2)	1.5 (0.1)	62 (1)
Ir3Ru1_1	1.2	4.4	35	11.0 (0.6)	0.164 (0.006)	3.6 (0.1)	1.28 (0.01)	17.0 (0.5)	5.7 (0.2)	66 (0.4)	4.4 (0.1)	2 (0.2)	72 (1)
Ir3Ru1_1	1.2	2.4	60	9.8 (0.3)	0.226 (0.002)	4.6 (0.2)	1.55 (0.05)	20 (1)	6.0 (0.2)	61 (1)	5.7 (0.3)	0.9 (0.3)	67 (1)
Ir1Ru1_1	1.2	2.8	14	3.4 (0.3)	1.28 (0.02)	10.7 (0.1)	2.71 (0.02)	36.1 (0.4)	1.68 (0.03)	26.39 (0.08)	16.4 (0.2)	4.8 (0.4)	28.1 (0.1)
Ir1Ru3	1.2	4.3	3	1.2 (0.1)	1.5 (0.1)	10.2 (0.8)	3.4 (0.2)	28 (2)	2.3 (0.2)	36 (1)	16 (1)	3 (4)	38 (1)
Ir1Ru3	1.2	2.3	5	1.1 (0.2)	1.5 (0.1)	9.5 (0.6)	3.0 (0.1)	27 (1)	1.3 (0.1)	32 (2)	19 (1)	7 (4)	33 (2)
Pd3Ru1_2	1.2	3	0.5	0.12 (0.02)	6 (1)	0	2.9 (0.3)	0	0	0	41 (6)	50 (7)	0
Pd3Ru1_2	1.2	2.6	0.5	0.15 (0.02)	4 (1)	0	2.4 (0.4)	0	0	0	35 (7)	58 (8)	0
Pd1Ru1_1	1.2	4.6	0.5	0.25 (0.04)	1.9 (0.1)	20 (1)	3.4 (0.3)	9 (1)	3.5 (0.5)	14 (3)	9 (2)	38 (7)	18 (3)
Pd1Ru3_1	1.2	3.6	7	2.4 (0.2)	2.8 (0.1)	5.8 (0.1)	1.9 (0.1)	7.2 (0.6)	0.73 (0.06)	5.2 (0.2)	63 (2)	13 (2)	5.9 (0.3)

Appendix C: GC-MS analysis

Table C1. Reactant and major products confirmed by chemical standards and GC-MS.

Chemical names	Molecular formula	Molecular structure
Benzene	C_6H_6	
Toluene	C_7H_8	
Ethylbenzene	C_8H_{10}	
o-xylene	C_8H_{10}	
n-propylbenzene	C_9H_{12}	
2-Ethyltoluene	C_9H_{12}	
indan	C_9H_{10}	
indene	C_9H_8	

Table C2. Possible by-products identified by GC-MS.

Chemical name	Molecular formula	Molecular structure
p-xylene	C_8H_{10}	
2-methylpropylbenzene	$C_{10}H_{14}$	
o-cymene	$C_{10}H_{14}$	
Pseudocumene	C_9H_{12}	
n-propyltoluene	$C_{10}H_{14}$	
4-propylbenzene	$C_{10}H_{14}$	
4-ethyl-m-xylene	$C_{10}H_{14}$	
Methylindane	$C_{10}H_{12}$	
1,2,3,4-tetramethylbenzene	$C_{10}H_{14}$	
7-methylbenzofuran	C_9H_8O	
2-ethylbenzaldehyde	$C_9H_{10}O$	
2,3-dihydro-1h-inden	$C_9H_{10}O$	
2,3-dihydro-1H-inden-1-one	C_9H_8O	
3-methylbenzaldehyde	C_8H_8O	
.alpha.-1-propenyl-benzenemethanol	$C_{10}H_{12}O$	

2,3-dihydro-1h-inden-1-ol	$C_9H_6O_2$	
3-chloro-n-isochroman-1-ylmethyl-propionamide	$C_{13}H_{16}ClNO_2$	
3,4-dihydro-1(2h)-naphthalenone	$C_{10}H_{10}O$	
1,1'-(1,4-butanediyl)bis-benzene	$C_{16}H_{18}$	
benzoic acid, 2-amino-, 3-phenyl-2-propenyl ester	$C_{16}H_{15}N_1O_2$	
Tricyclo[10.2.2.2(5,8)]octadeca-5,7,12,14,15,17-hexaen	$C_{18}H_{20}$	
Benzyl nitrile	C_7H_7N	
3-benzylidene-2-(3-pyridyl)-1-pyrroline	$C_{16}H_{14}N_2$	
2-biphenyl ester 4-ethylbenzoic acid	$C_{21}H_{18}O_2$	
1,1'-(1,5-hexadiene-1,6-diyl)bis benzene	$C_{18}H_{18}$	
4-methylbenzonitrile	C_8H_7N	
1,2,3,5-tetrahydro-1,3-methanopentalene	C_9H_{10}	

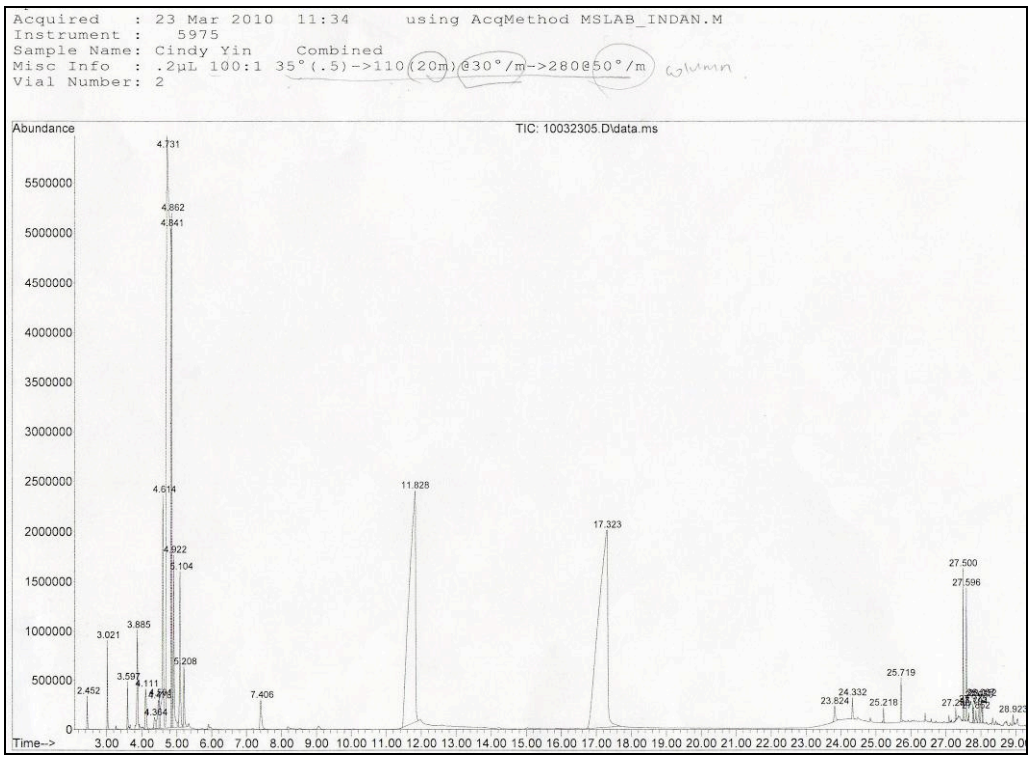

Figure C1. Product evaluation for ring opening of indan by GC-MS analysis. (Mixture of indan and RO products).